

Rainbow phenomena : development of a laser-based, non-intrusive technique for measuring droplet size, temperature and velocity

Citation for published version (APA):

van Beeck, J. P. A. J. (1997). *Rainbow phenomena : development of a laser-based, non-intrusive technique for measuring droplet size, temperature and velocity*. [Phd Thesis 2 (Research NOT TU/e / Graduation TU/e), Applied Physics and Science Education]. Technische Universiteit Eindhoven. <https://doi.org/10.6100/IR493789>

DOI:

[10.6100/IR493789](https://doi.org/10.6100/IR493789)

Document status and date:

Published: 01/01/1997

Document Version:

Publisher's PDF, also known as Version of Record (includes final page, issue and volume numbers)

Please check the document version of this publication:

- A submitted manuscript is the version of the article upon submission and before peer-review. There can be important differences between the submitted version and the official published version of record. People interested in the research are advised to contact the author for the final version of the publication, or visit the DOI to the publisher's website.
- The final author version and the galley proof are versions of the publication after peer review.
- The final published version features the final layout of the paper including the volume, issue and page numbers.

[Link to publication](#)

General rights

Copyright and moral rights for the publications made accessible in the public portal are retained by the authors and/or other copyright owners and it is a condition of accessing publications that users recognise and abide by the legal requirements associated with these rights.

- Users may download and print one copy of any publication from the public portal for the purpose of private study or research.
- You may not further distribute the material or use it for any profit-making activity or commercial gain
- You may freely distribute the URL identifying the publication in the public portal.

If the publication is distributed under the terms of Article 25fa of the Dutch Copyright Act, indicated by the "Taverne" license above, please follow below link for the End User Agreement:

www.tue.nl/taverne

Take down policy

If you believe that this document breaches copyright please contact us at:

openaccess@tue.nl

providing details and we will investigate your claim.

Rainbow Phenomena:

**development of a laser-based, non-intrusive
technique for measuring
droplet size, temperature and velocity**

(P.A.J. van Beeck)

RAINBOW PHENOMENA:
development of a laser-based, non-intrusive
technique for measuring droplet size,
temperature and velocity

Jeroen van Beeck

CIP-DATA LIBRARY TECHNISCHE UNIVERSITEIT EINDHOVEN

Beeck, Jeronimus Petrus Antonius Johannes van

Rainbow phenomena : development of a laser-based, non-intrusive technique for measuring droplet size, temperature and velocity / by

Jeronimus Petrus Antonius Johannes van Beeck. -

Eindhoven : Technische Universiteit Eindhoven, 1997. -

Proefschrift. -

ISBN 90-386-0557-9

NUGI 812

Trefw.: atmosfeeroptica / lichtverstrooiing / lasermeettechniek / deeltjesgroottemeting / druppels.

Subject headings: atmospheric optics / light scattering / measurement by laser beam / temperature measurement / velocity measurement / shape measurement / drops.

Copyright ©1997 J.P.A.J. van Beeck

Omslagontwerp: Ben Mobach, TUE

Druk: Universiteitsdrukkerij, TUE

No part of this book may be reproduced in any form without the written permission of the author

**RAINBOW PHENOMENA:
development of a laser-based, non-intrusive
technique for measuring droplet size,
temperature and velocity**

PROEFSCHRIFT

ter verkrijging van de graad van doctor aan de
Technische Universiteit Eindhoven, op gezag
van de Rector Magnificus, prof.dr. M. Rem,
voor een commissie aangewezen door het College
van Dekanen in het openbaar te verdedigen op
donderdag 26 juni 1997 om 16.00 uur

door

Jeronimus Petrus Antonius Johannes van Beeck

geboren te Deurne

Dit proefschrift is goedgekeurd door de promotoren:

prof.dr.ir. M.E.H. van Dongen

en

prof.dr.ir. G.J.F. van Heijst.

*My heart leaps up when I behold
A rainbow in the sky*

William Wordsworth (1770-1850)

Contents

1	Introduction	1
1.1	Development of laser-based, diagnostic tools in fluid dynamics . . .	1
1.2	Rainbow in the sky	4
1.3	Rainbow in the laboratory	12
1.4	Thesis overview	17
2	Off-axis laser-beam scattering by a sphere using Lorenz-Mie theory	19
2.1	Definition of the scattering problem for Lorenz-Mie theory	19
2.2	Solution of the scattering problem	22
2.3	Far-field approximation	28
2.4	Localization principle	29
2.5	Off-axis laser-beam scattering	31
3	Surface integral method for light scattering by ellipsoids	39
3.1	Rainbow at surface of ellipsoidal droplet: a geometrical approach . .	39
3.1.1	Ray tracing in an ellipsoid	39
3.1.2	Polarization	42
3.1.3	Phase	44
3.1.4	Gain factor	44
3.1.5	Scattered field at the droplet surface	46
3.2	Rainbow in the far field: a hybrid approach	47
3.2.1	The vector Kirchhoff integral relation	47
3.2.2	Solving the Kirchhoff integral for the primary rainbow . . .	49
3.3	Surface integral method versus Lorenz-Mie theory	59
3.4	Primary rainbow from prolates and oblates	60
4	Airy theory for the rainbow	67
4.1	The rainbow from a sphere according to geometrical optics	67
4.2	Airy fringes	70
4.3	Domain of validity of the Airy theory	76

5	Rainbow-interferometric measurements of droplet size and temperature	81
5.1	Detection of the monochromatic rainbow by a linear CCD camera	81
5.2	Simultaneous determination of droplet size and temperature	83
5.2.1	Ripple structure	85
5.3	Non-sphericity detection	88
5.3.1	Non-circular rainbows	88
5.3.2	Selection of spherical droplets	89
5.4	Dynamic calibration procedure for the rainbow technique	89
5.5	Experimental results	90
5.6	Rainbow patterns without ripple structure	91
6	Rainbow interferometry with wire diffraction	93
6.1	Photomultiplier set-up for detection of the rainbow in a spray	93
6.1.1	The effect of wire diffraction on the rainbow pattern	97
6.2	Determination of droplet velocity, size and temperature	100
6.3	Experimental results in a water spray	101
6.4	Transient events	103
7	Discussion and conclusions	107
	Symbols	111
	References	117
	Summary	125
	Samenvatting	127
	Acknowledgements	129
	Curriculum vitae	131

Chapter 1

INTRODUCTION

1.1 Development of laser-based, diagnostic tools in fluid dynamics

The motivation for this work is the experimental research on heat and mass transfer in liquid spray environments. Liquid spraying is used in combustion engines and in numerous agricultural and industrial processes. In order to be able to choose the proper spray configuration, it is essential to develop a complete understanding of the fundamental phenomena that determine the spray performance. Therefore, diagnostic tools should be developed that are suitable for the experimental study of spray processes in laboratory and realistic conditions.

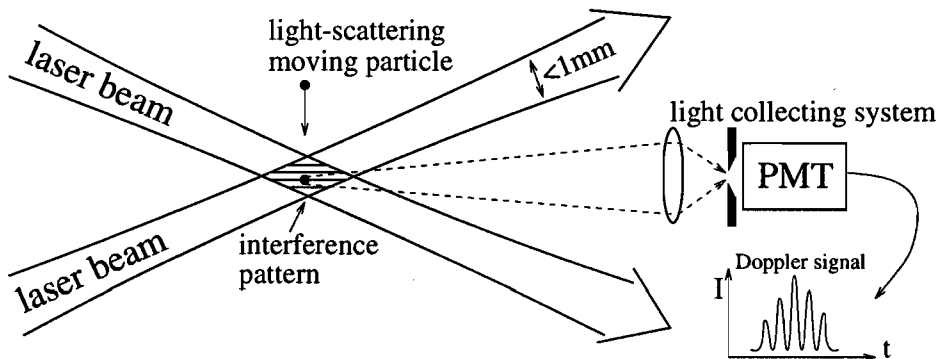


Figure 1.1: Schematic of the optical configuration of a laser Doppler instrument for measuring one velocity component of the tracer particle in a fluid flow.

Diagnostic tools based on light detection have the advantage over mechanical measuring probes that they are relatively easy to use in complex experimental situations such as in combustion research. Moreover, optical measurement techniques are non-intrusive; the physical phenomenon studied is not disturbed by the light source of the instrumentation. It is the development of this light source that

has undergone a revolutionary impulse since the first successful operation in 1960 of Light Amplification by Stimulated Emission of Radiation (LASER), announced by Th. H. Mainam (see e.g. Ref. [25]). The directionality and exceedingly high radiant power of the laser beam soon resulted in a variety of improved and novel optical measurement techniques in the field of experimental fluid dynamics.

Laser Doppler Velocimetry (LDV) was the first laser-based measurement technique in fluid dynamics. Already in 1964, Yeh and Cummins[90] performed velocity measurements in a pipe flow of water using LDV. The technique is based on the formation of an interference pattern in the cross-over region of two crossing laser beams (Fig. 1.1). This region is visible because of the scattering of laser-light by small tracer particles in the flow. A light-collecting system observes a so-called Doppler signal of one tracer at a time. This signal contains a Doppler frequency which is proportional to the tracer velocity which is aimed to be as close as possible to the fluid flow. Because one tracer is evaluated at a time, no spatial flow structures are measured. However, an important feature of LDV is its rapid response to velocity changes which allows extraction of turbulent flow properties. More is said on the principles and practice of LDV by e.g. Durst et al.[14].

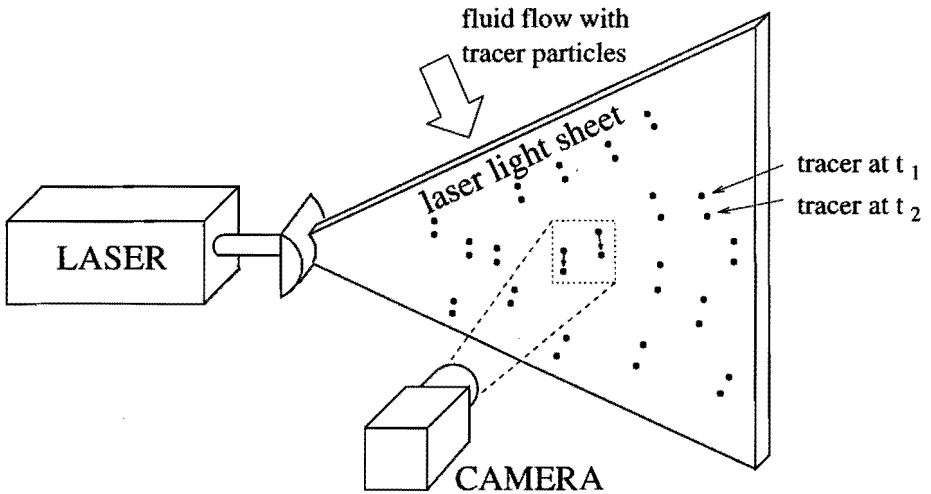


Figure 1.2: *Outline of the experimental setup for particle image velocimetry.*

In 1980, Meynart[46] proposed Particle Image Velocimetry (PIV). PIV is a most promising, laser-based, diagnostic technique that measures the 2D- or even 3D-velocity data-set of an instantaneous spatial flow structure. The principle of this technique is the analysis of two images of the flow that is seeded with tracer particles illuminated by a powerful laser-light sheet. As for LDV, tracers have to be smaller than $10\ \mu\text{m}$ in order to follow gas flow fluctuations up to 700 Hz with a precision of 1% (see Ref. [15]). The local fluid velocity-vector is deduced from

the local average particle-image displacement between the two images (Fig. 1.2). A review on PIV and related techniques is given by Adrian[3].

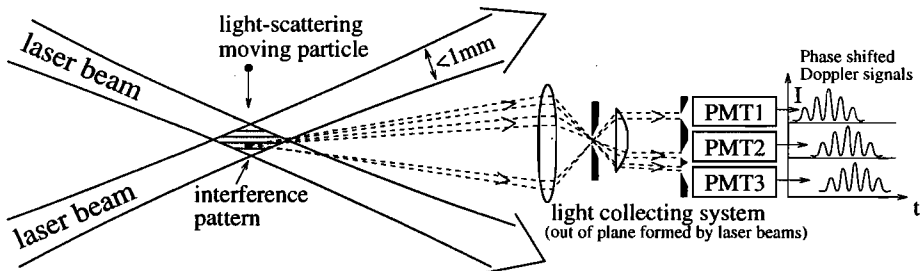


Figure 1.3: Sketch of the phase Doppler particle analyzer; one velocity component and the diameter of a single particle can be obtained with this optical setup.

Both LDV and PIV can be applied to measure the droplet velocity in a liquid spray. But to characterize droplets also information on size, shape, composition and temperature is required. In 1975, Durst and Zaré[16] proposed a method to determine the particle size from the spatial frequency of the scattered interference pattern in LDV. In 1984, Bachalo and Houser[7] presented a commercial Phase/Doppler instrument based on this idea; it contains three detectors collecting scattered laser-light at different angular positions (Fig. 1.3). From the phase shifts between the Doppler signals of the three detectors a drop size range over a factor of 100 can be determined. Consequently, this instrument can measure velocity/size correlations of small and large particles with one optical setting. Since 1984, the phase-Doppler Anemometry (PDA) has been improved and successfully applied to for example fuel spray combustion, agricultural spray research and fire and toxic gas control development.

In 1990, Naqwi et al.[51] extended PDA toward the measurement of the refractive index of the light-scattering particle. Extended phase-Doppler anemometry (EPDA) consists of two sets of receiving optics instead of one as in Fig. 1.3. The sign and ratio of the two phase signals is used to recognize the transparent particle material. Another extension of PDA to the measurement of the refractive index has been proposed by Onofri et al.[56] and is called the dual burst technique (DBT). Using only one receiving unit, two scattering processes, i.e. reflection and refraction of light by the particle, are identified in the Doppler signal. The reflected part serves to determine the particle diameter whereas from the refracted part the particle refractive index and velocity can be obtained. The advantage of both EPDA and DBT is their large measuring range of particle refractive indices. Provided that one knows the relationship between the refractive index and the temperature, the droplet temperature can be measured as well. Unfortunately, the temperature can not be estimated with a precision higher than several decades of degrees Celsius.

Over the years, different laser-based techniques have been proposed to measure

the droplet temperature. In 1985, Murray and Melton[50] presented a technique using the fluorescence of an organic dopant added to the droplet. The temperature is determined by measuring the temperature-dependent ratio of the fluorescence intensity of the organic dopant to the fluorescence intensity of excited state molecules that are formed by the binding of the solvent together with the excited dopant. The excitation results from ultraviolet laser absorption. A measurement resolution of 1 °C has been claimed. Practically, fluorescence thermometry seems to be complex and suffers from the necessity of the addition of a substance to the droplets.

Less complex thermometric techniques have been proposed utilizing the temperature dependence of the index of refraction as for DBT and EPDA. In 1993, Massoli et al.[45] deduced the droplet temperature from the ratio of horizontally polarized scattered-light, detected at two different positions. One year later, Schaller et al.[65] presented a technique that measures the ratio of brightnesses of different light spots, i.e. glare points (Sec. 1.3), on the droplet surface which is observed through a lens of finite aperture. The ratio exhibits a monotonic dependence on the index of refraction. For both techniques, an accuracy of less than 10 °C has been reported.

All the above thermometric techniques are based on the ratio of light intensities. This leads to inevitable errors in dense sprays due to obstruction of the optical paths. But most importantly, ratioing techniques lack a certain characteristic structure which is needed to reject noisy data. This makes it difficult, but not impossible, to produce a reliable instrument.

This thesis deals with the development of a non-intrusive measurement technique, first presented by Roth et al.[59]. The technique is based on the primary rainbow, formed by laser-light scattering droplets. From the angular position of the rainbow, the refractive index is deduced and subsequently the temperature. The advantage of the technique is its characteristic signature as it was called by Sankar et al.[64]. This is the reason why these authors could manufacture a reliable "Rainbow Refractometer System"[62] which uses ideas proposed by Van Beeck and Riethmuller[70, 71].

1.2 Rainbow in the sky

The background of this thesis is known as one of the most beautiful optical phenomena in nature, i.e. the rainbow. It is seen particularly brightly when one looks towards a thunderstorm shortly before sun-set having the sun shining from the back. Marvelously concentric coloured bands can be distinguished on a part or parts of a circle arranged from the inner to the outer border as violet, indigo, blue, green, yellow, orange and red. Sometimes, higher in the sky, a broader secondary rainbow is seen which is much weaker in intensity and has its colours reversed. The photograph in Fig. 1.4 shows that the sky below the primary and above the secondary rainbow is brighter than the region between both rainbows; this dark re-

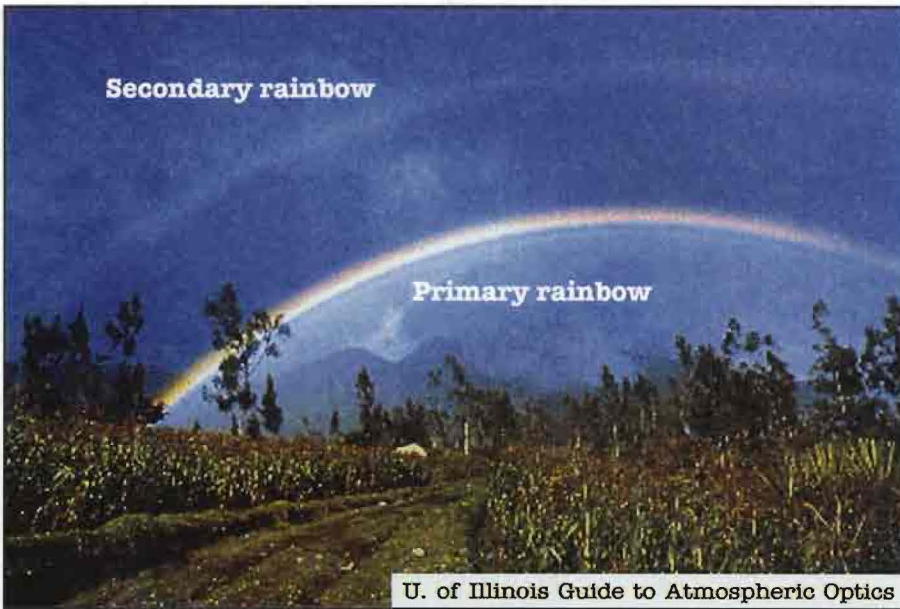


Figure 1.4: *The rainbow in the sky (printed with permission of Dr. Mohan Ramamurthy of the University of Illinois).*

gion was already noticed by Alexander of Aphrodisias in 200 AD and is historically known and often cited as the Alexander’s Dark Band.

At this point, it is interesting to pose the question of what the distance is between the observer and the rainbow. In the case of a fountain, this distance is quite well defined because the rainbow is generated by the droplets in the fountain. But, when one is looking at a rainbow while getting wet at the same time, then one is unable to tell its exact position, even when reference points in the landscape are present. The question is related to why we see smooth coloured bands, although we are looking at droplets filling only a tiny volume-fraction of the space. The explanation lies in the limiting resolution of our imaging system, the human eye. Fig. 1.5 shows the eye, trying to form images of distant droplets. Due to the finite aperture of the pupil, the images will be distorted by Fraunhofer diffraction forming Airy patterns on the eye’s retina. The towering central high irradiance of one Airy pattern is known as the Airy disk. The diameter of this disk at the retina is approximately given by Hecht[26]:

$$D_{disk} \approx 2.44 \frac{f\lambda}{D_{pupil}}, \quad (1.1)$$

where f is the focal length of the eye’s lens, λ the wavelength of the light and D_{pupil} the diameter of the pupil. A criterion for the minimum angular separation,

$\Delta\phi_{min}$, between two distant points can be defined from the situation where the centre of one Airy spot touches the edge of another[26]:

$$\Delta\phi_{min} \approx 1.22 \frac{\lambda}{D_{pupil}}. \quad (1.2)$$

For instance, when $D_{pupil} \approx 2$ mm, then $\Delta\phi_{min}$ equals $\pm 0.02^\circ$. With an intermediate distance between the droplets of 20 cm, the observer cannot distinguish single droplets at a distance of 500 m. This overlapping of diffracted droplet images at the retina accounts for the continuous character of the rainbow in the sky. Obviously, droplets further away than 500 m will also contribute to the rainbow, which is why one ought to speak about coloured layers instead of coloured bands. Consequently, one understands that the rainbow is a three-dimensional phenomenon which explains the problem in defining a unique position. As the scattered-light intensity from the droplets at 1000 m is only 25 % of the intensity of those at 500 m away from the eye, one can state that the rainbow is about twice as deep as the distance at which the human eye can still resolve two droplets.

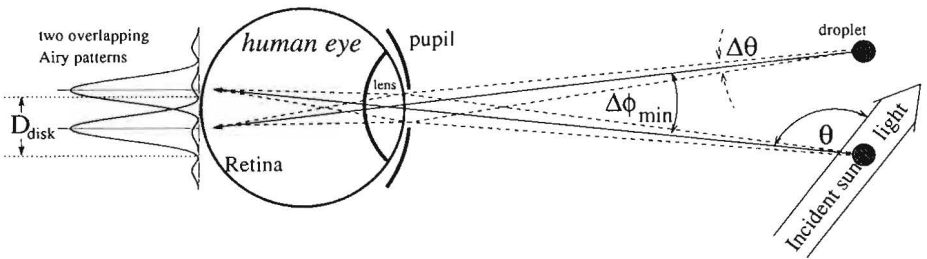


Figure 1.5: *The limiting resolution of the human eye. The scattering angle θ is the angle between the incident sun rays and a ray scattered from the droplet reaching the eye of the observer.*

The overlapping of coloured points was an effect that Georges Seurat aimed at in his paintings. As a pointillist, he painted small dots about 2.5 mm from each other. For instance, in “*Dimanche d’été à la Grande Jatte*” (1885; Art Institute, Chicago) the blending of the colours occurs in the eye when the observer stands at a distance of several metres. However, the painting is two-dimensional, thus there is no question about its position.

Now it is understood that the rainbow is not a thing of which the position can be determined by the stereoscopic properties of the eyes, some rainbow characteristics will be explained. Therefore, one has to define the scattering angle θ as the angle that a scattered sun ray, reaching the observer, makes with the incident sun beam. The eye detects only a tiny range of scattering angles, i.e. $\theta \pm \Delta\theta/2$, from each droplet in the rainbow, as indicated in Fig. 1.5; for a droplet at a distance of 500 m, this range would be $\theta \pm \sim 0.0001^\circ$. This means that looking at a certain droplet, situated in a coloured layer, implies looking in a certain direction. However, due

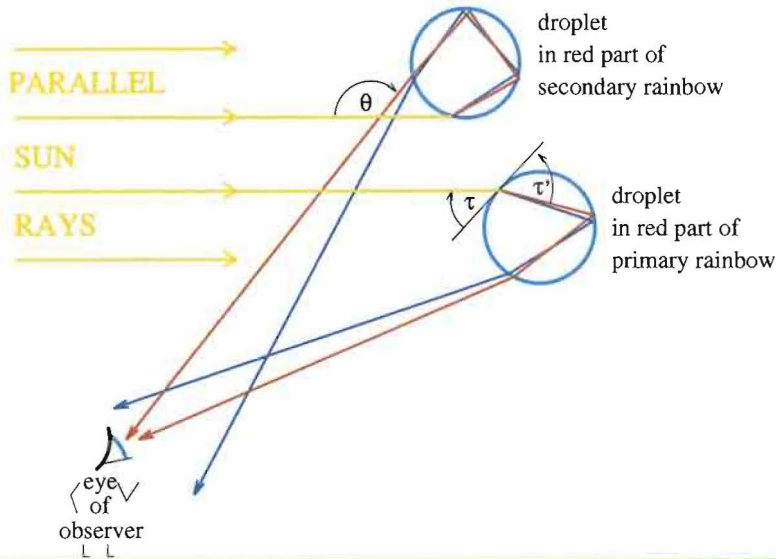


Figure 1.6: The path of sun rays through two raindrops in the red parts of the primary and secondary rainbows. One internal reflection yields the primary rainbow and two internal reflections result in the secondary rainbow whose colours are reversed. θ is the scattering angle. τ is the incidence angle and τ' is the angle between the deviated incident ray and the tangential to the droplet surface.

to the limiting resolution of the human eye, the resolution in the direction is decreased to a range of scattering angles of about $\theta \pm \Delta\phi_{min}/2$ instead of $\theta \pm \Delta\theta/2$. Nevertheless, it was computed from Eq. 1.2 that this range is still small, which makes it possible to study the rainbow characteristics from the scattering diagrams of a single droplet.

In 1637, René Descartes was the first to explain the brightness of the rainbow. He traced the paths of light rays in a single spherical water droplet using the law of reflection and Snell’s law of refraction describing how a ray deviates upon entering a droplet:

$$\cos \tau = m \cos \tau'. \tag{1.3}$$

Here τ is defined as the angle between an incoming ray and the tangential to the droplet surface and τ' represents the angle between the same tangential and the refracted ray (see Fig. 1.6). m is the refractive index which depends on the density and temperature of the medium and on the colour of the light. The latter accounts for the dispersion of light first announced by Newton in 1666; this was not seen by Descartes. Nevertheless, Descartes established a correct relationship between the angles θ , τ and τ' for incoming sun rays that first refract, then reflect several times

on the internal surface of the droplet and finally refract again to emerge from the droplet as outlined schematically in Fig. 1.6:

$$\theta = 2\tau - 2(N - 1)\tau'. \quad (1.4)$$

N corresponds to the number of interactions between a ray and the surface of the scatterer. Fig. 1.7 has been constructed from this relationship and with the help of Snell's law. It shows $|\theta|$ as a function of τ for one internal reflection ($N = 3$) and two internal reflections ($N = 4$). For m , the value for red light (i.e. $\lambda \approx 700$ nm), an ambient temperature of $T = 20^\circ\text{C}$ and a pressure of $P = 1.023$ bar is used. The scattering angle in both curves exhibits an extremum with respect to the incident angle. This means that near these two extrema a large range of incoming rays focus on two narrow ranges of scattering angles (i.e. directions), which results in two regions of high scattered-light intensity, called the rainbows. Descartes concluded that the primary rainbow arises from incoming sun rays which have experienced one internal reflection. $|\theta_{rg}|$ is the scattering angle of minimum deviation known as the (primary) geometric rainbow angle. $|\theta_{rg}|$ is about 138.9° for violet and 137.4° for red light because violet is refracted more than red. Thus the spectrum of the sunlight is fanned out by the droplet similarly to the manner in which a prism acts on white light. By identical reasoning, the secondary rainbow was found to result from two internal reflections.

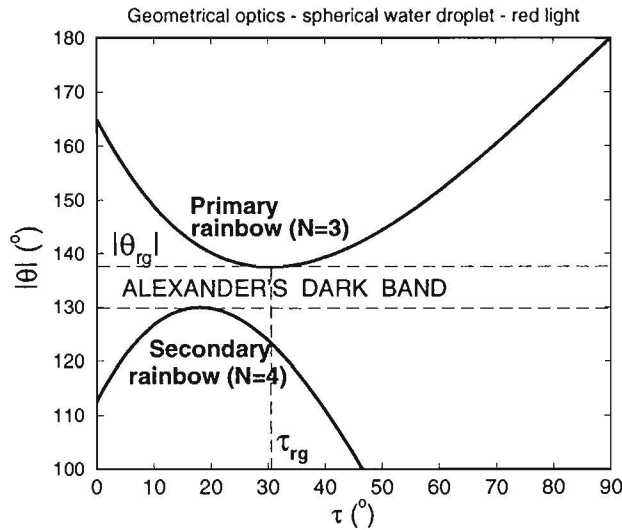


Figure 1.7: The relationship between the scattering angle and the incidence angle for one ($N = 3$) and two ($N = 4$) internal reflections of red light in a spherical water droplet. Focusing of the light rays near the extrema leads to the brightness of the primary and secondary rainbow.

Rays forming the primary and secondary rainbows cannot come from droplets in the Alexander's Dark Band because to do so they would have to come from rays having a scattering angle less than $|\theta_{rg}|$ for the primary bow and greater than the angle of maximum deviation for the secondary bow. This explains why the sky between both bows is darker than beneath the primary rainbow and above the secondary rainbow.

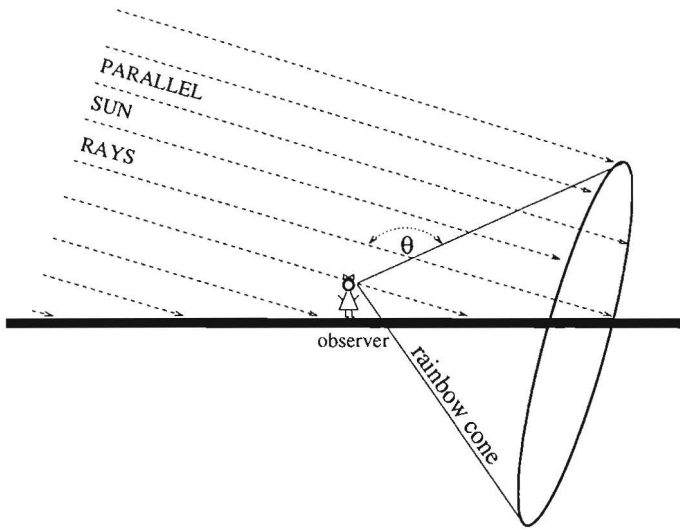


Figure 1.8: The primary rainbow in the sky is situated near the surface of a cone having the axis formed by the sun ray passing the observer and having 180° minus the geometric rainbow angle as the cone angle.

It is a small step from the study of a single droplet to explain the primary rainbow formed by an ensemble of raindrops. From the definition of the scattering angle θ in Fig. 1.5, it results that an entire surface in the sky exists for which this angle is the same. This surface lies on a cone having $(180^\circ - |\theta|)$ as cone-angle and having the axis connecting the observer and the sun (Fig. 1.8). When the raindrops are all identical and spherical, the scattered-light intensity detected from all drops crossing this surface is the same. Consequently, a certain coloured layer lies on the surface of such a cone. This cone is higher in the sky when the sun is lower to horizon. In an airplane the entire cone might be seen. Thus the rainbow is fixed to the observer; everybody has his own rainbow.

Closer examining of Fig. 1.7 reveals more than deduced until so far. Due to the extremum of θ with respect to τ , there are, for $|\theta_{rg}| < |\theta| \lesssim 165^\circ$ concerning the primary rainbow, always two rays that have the same scattering angle. In 1802, Young was the first to realize that these rays interact according to the principle of optical interference that he formulated starting from the work of Christiaan Huygens on a wave-like theory of light. As a result of this principle, the parallel

rays interfere at infinity in a destructive or constructive manner according to their phase difference, thus forming supernumerary bows inside the primary rainbow (see for instance Plate 14 in Ref. [48] for a nice photograph). Based on the same principle of optical interference, in 1838 Airy[4] successfully developed a theory for the rainbow which will be treated in Chap. 4 of this thesis.

Fig. 1.9 shows the scattered-light intensity versus the scattering angle for the primary rainbow according to the so-called Airy theory. The droplet diameter is $300\ \mu\text{m}$ and the wavelength of light varies from $\lambda = 700\ \text{nm}$ for red to $\lambda = 420\ \text{nm}$ for violet light. The pressure is 1.023 bar and the temperature $T = 20^\circ\text{C}$. The figure represents interference structures for each colour. The first series of maxima (seen from left to right) is known as the main rainbow maximum which for $D = 300\ \mu\text{m}$ is particularly well developed as all the colours are well separated. The first supernumerary bow shows the same structure as the main rainbow maximum but is less intense. Higher-order supernumerary bows have a different arrangement of colours because of the strong overlapping of the colours. For this specific droplet size it is interesting to notice that there are gaps between the second, third and fourth supernumerary bow.

Fig. 1.10 shows (normalized) Airy rainbow patterns as in Fig. 1.9 but now for a smaller droplet diameter of $30\ \mu\text{m}$, common for the droplet dimension in mist. Here, the rainbow is 464 times less intense and twice the width of the rainbow in Fig. 1.9. The main rainbow maximum appears almost entirely white due to colour mixing. Therefore, it is known as the white rainbow or mistbow. Only one or two coloured supernumerary bows are visible and are well separated from the white main maximum. It is interesting to see that for the supernumeraries the order of the colours is the reverse of those in an ordinary primary rainbow like in Fig. 1.9.

The Airy theory predicts how the features of the rainbow change with droplet size. However, in reality, there is more than just the size of the droplet that determines the characteristics of the rainbow. First, one has to realize that the sun is not a point source. Therefore, the sunbeams are not parallel but spread over an angle of about half a degree, thus obliterating the colours of the rainbow. Secondly, a normal rain shower contains a broad spectrum of droplet diameters. On top of this, the large raindrops are not spherical. Fraser[19] explains why under these conditions it is still possible to see supernumerary bows.

This section on the rainbow in the sky has described only few rainbow phenomena that the human eye can observe. Additional phenomena are discussed in an almost infinite number of reference books and journal articles; Minnaert[48] and Humphreys[32] are among those most cited. An interesting WWW-site is *About Rainbows*[42] containing an extended list of references. From all these works it can be concluded that there do not exist two rainbows that are the same. Some observations of abnormal rainbows, reported by Minnaert[48], are even still waiting for convincing explanations.

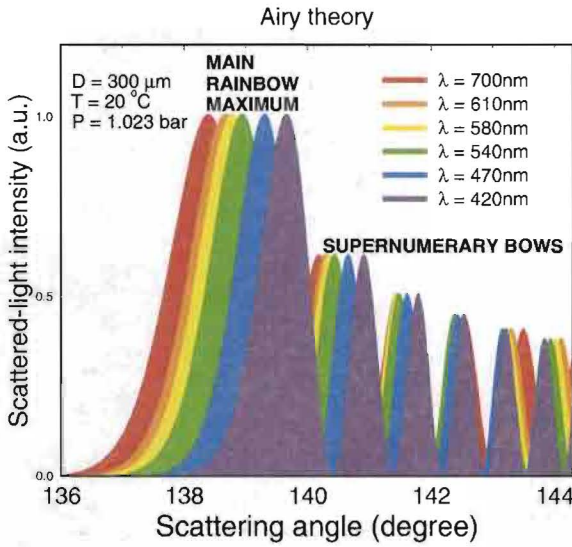


Figure 1.9: The rainbow according to Airy's theory for different colours. The main rainbow maximum and supernumerary bows are predicted. The droplet diameter is $300 \mu\text{m}$.

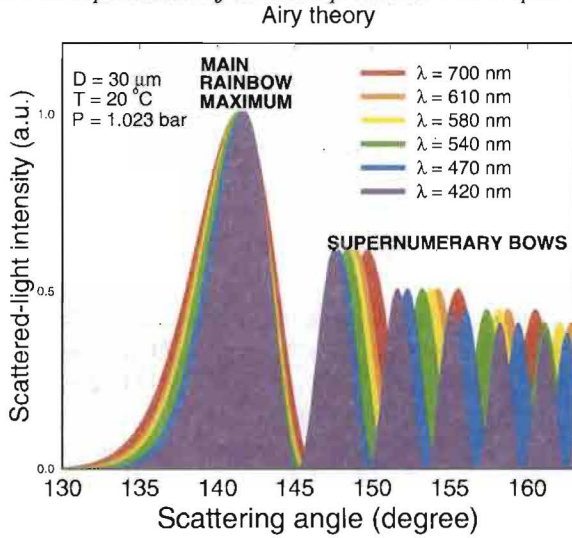


Figure 1.10: The rainbow according to the Airy theory for a droplet diameter of $30 \mu\text{m}$. Mixing of colours gives rise to a white main rainbow maximum. The order of colours in the first supernumerary bow is reversed.

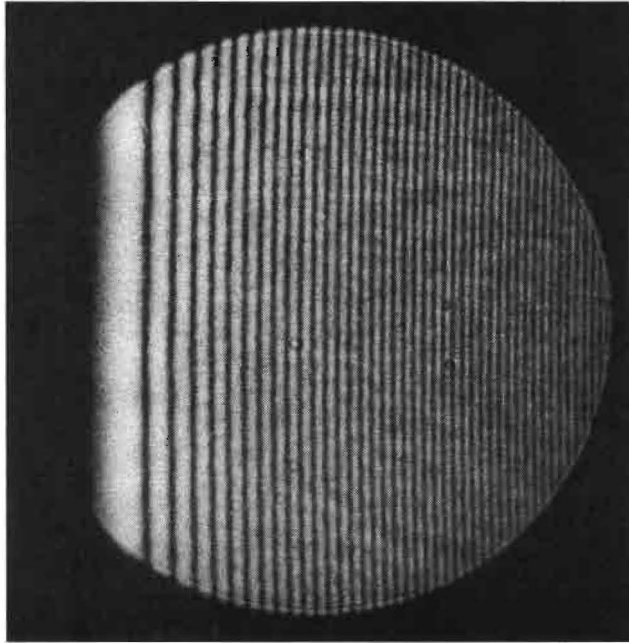


Figure 1.11: *Supernumerary bows in the monochromatic primary rainbow created by a nearly spherical droplet suspended from a small tube with its point ground flat.*

1.3 Rainbow in the laboratory

The rainbow in the laboratory discussed in this thesis is slightly different from the rainbow in the sky, introduced in Sec. 1.2. Therefore, it deserves some words of explanation.

The rainbow in the laboratory is created by a single droplet scattering laser light instead of sunbeams. Consequently, the scattered-light intensity distribution is monochromatic. There is no mixing of colours which would blur the supernumerary bows. Fig. 1.11 depicts the resulting so-called monochromatic primary rainbow; the supernumerary bows are clearly visible. The photograph has been taken of a nearly spherical droplet suspended from a small tube with its point ground flat. The camera is focused at infinity so that the supernumerary bows correspond to those in the far field[74].

Not only the primary rainbow but also the second and even higher-order rainbows, resulting from higher-order internal reflections, can be studied accurately by observing the monochromatic angular scattered-light pattern of a single droplet. Walker[86] studied the first 13 rainbows of water and other liquids using a student He-Ne laser. In theory, an infinite number of rainbows exist; the higher the order, the broader and dimmer the pattern becomes.

The Airy theory mentioned in the previous section gives a good idea of what a rainbow resembles. However, the theory is not complete. In 1845, Faraday found an interrelationship between light waves and electromagnetism. Some years later, Maxwell captured this discovery in a single set of mathematical equations, now known as the Maxwell equations. These equations were solved for the scattering of an incident electromagnetic plane wave by a spherical particle consisting of a homogeneous medium[41, 47]. The solution is called the Lorenz-Mie theory and is treated in Chap. 2. It gives an exact solution for the problem considered. Consequently, it should be able to predict at least the supernumerary bows in the primary rainbow region.

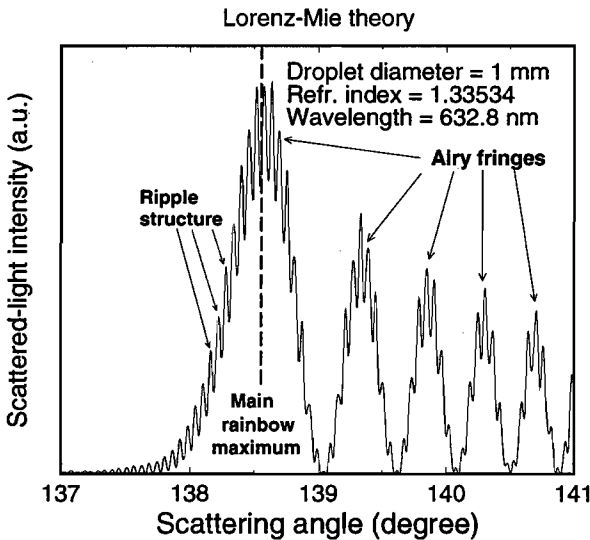


Figure 1.12: *The monochromatic rainbow according to the Lorenz-Mie theory. A ripple structure is superimposed on the clearly visible Airy rainbow pattern.*

Fig. 1.12 shows the angular scattered-light distribution for $137^\circ < \theta < 141^\circ$ according to the Lorenz-Mie theory for the wavelength of the light of a He-Ne laser, i.e. $\lambda = 632.8 \text{ nm}$. The droplet size is 1 mm and the refractive index is $m = 1.33534 + 0i$, where $0i$ (i is the imaginary unit) implies that there is no absorption of light by the medium. The incident light is polarized normal to the scattering plane made by the incident and scattered wave vector.¹ The figure clearly shows the main rainbow maximum and the supernumerary bows. Because the main maximum results from the same type of optical interference as the supernumeraries, they are both referred to as Airy fringes or the Airy rainbow pattern. High frequency

¹A polarization in the scattering plane would give a 25 times weaker rainbow pattern because the internal reflection occurs close to the Brewster angle (see e.g. Van de Hulst[77]).

oscillations are superimposed on these Airy fringes which are not predicted by the Airy theory and not visible in the rainbow in the sky. To trace the origin of this ripple structure in terms of geometrical rays, it is necessary to examine the angular frequency spectrum.

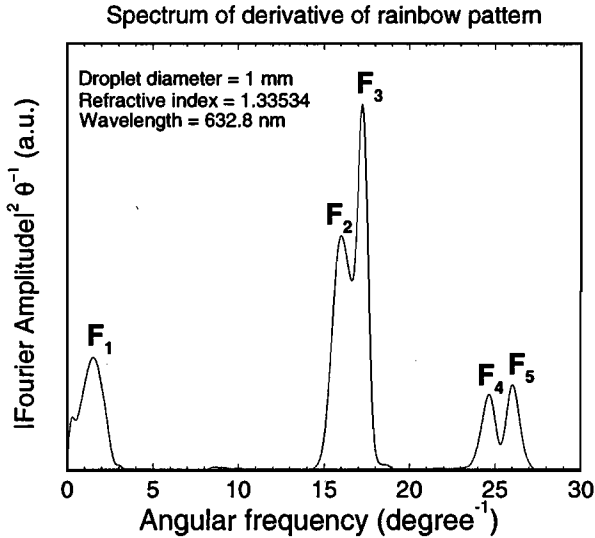


Figure 1.13: *The derivative of the spectrum of the monochromatic rainbow. Each of the labeled peaks corresponds to the interference between two geometrical rays.*

In Fig. 1.13 the derivative of the spectrum of the monochromatic rainbow in Fig. 1.12 is depicted. The reason to show the derivative is to bring the amplitudes of the different peaks in the same order of magnitude for better readability. The angular frequency F corresponds to the number of light intensity oscillations per degree scattering angle. Each peak, labeled from F_1 to F_5 , can be explained by the principle of optical interference at infinity between two parallel rays separated by a distance δ_i . Therefore, one can treat this interference analogous to the Young's double-slit experiment (Ref. [27]):

$$F_i = \frac{\delta_i}{\lambda} \frac{\pi}{180^\circ} \quad i = 1..5. \quad (1.5)$$

From this equation and Fig. 1.13, the distances δ_1 to δ_5 can be computed. The connection between each distance and the corresponding geometrical rays can best be found graphically by computing the $\theta - \tau$ relationship for light reflected at the outer droplet surface and transmitted across the drop without and with internal reflections, as was done for one and two internal reflections in Fig. 1.7. In this manner, the main contributions to the primary rainbow are found to arise from external reflection and one internal reflection (Fig. 1.14). The three resulting rays

B, C and D interfere upon emerging from the droplet at a detector placed in the far field to yield the 3 dominant peaks at frequencies, F_1 , F_2 and F_3 :

F_1 : Rays B and C represent the contributions of internal reflection to the primary rainbow. After leaving the droplet with the same scattering angle, their intermediate distance is δ_1 . Interference yields the Airy fringes corresponding to the peak at angular frequency F_1 .

F_2 : Ray C, a once-internally reflected ray, interferes with the external reflection (ray D) resulting in F_2 .

F_3 : Ray B, the other once-internally reflected ray at scattering angle θ , interferes with ray D to yield the angular frequency F_3 .

The relationship between F_1 , F_2 and F_3 is given by

$$F_1 = F_3 - F_2. \quad (1.6)$$

Peaks F_2 and F_3 account mainly for the ripple structure superimposed on the Airy fringes.

Close study reveals that distances δ_4 and δ_5 have to result from the interference between internal reflection, i.e. rays B and C, and the ray E coming from the edge of the droplet (Fig. 1.14). The explanation of this edge ray is not yet entirely understood. In Fig. 1.14, it has been represented as a ray traveling along the curved surface of the droplet spraying energy continually forward tangentially away from the surface. However, according to Van de Hulst[78], the energy left in such a surface wave after completing half a circle around the sphere can be neglected. Later, Lock[37] and Van de Hulst and Wang[84] stated that edge rays might be a combination of $N - 2$ times critically-reflected rays and the higher-order rainbows that accumulate in the extreme edge region of the droplet.

Optical interference between edge ray E and the external reflection (ray D) is weak but nevertheless visible as a small peak between F_1 and F_2 . An edge ray A probably also exists but it would be situated so close to ray C (see Ref. [84]) that the interference with other rays would not appear as separate peaks in the power spectrum of Fig. 1.13.

An interesting alternative relationship between the monochromatic rainbow pattern and its spectrum is given by Van Beeck and Riethmuller[74] and is based on the concepts of Fourier optics (see Refs. [28, 20]). For this, the glare point amplitude pattern $g(p)$ as sketched in Fig. 1.14 has to be defined. An observer sees the amplitude squared of $g(p)$ on the surface of the drop. This pattern is the Fourier transform of the linearly-polarized Lorenz-Mie scattering amplitude, $S_1(\theta)$, taken over a limited range of angles covered by an imaging lens as explained by Van de Hulst and Wang[84] and Lock[36]:

$$g(p) = \mathcal{F}\{S_1(\theta)\}. \quad (1.7)$$

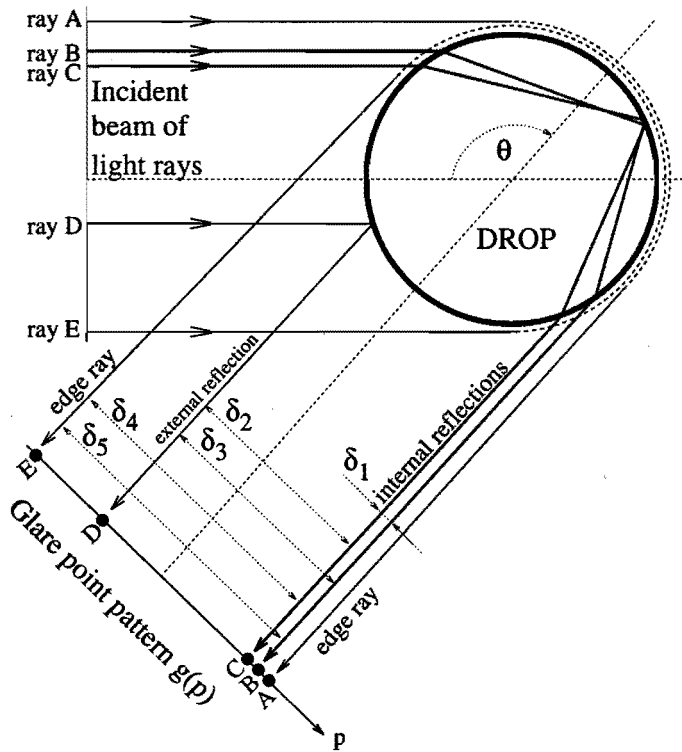


Figure 1.14: Rays contributing to the primary rainbow. The way that rays A and E emerge from near to the edge of the droplet is not completely understood and is sketched schematically as dashed surface waves.

The angular scattered-light intensity distribution $i_1(\theta)$, as depicted in Fig. 1.12, is then

$$i_1(\theta) = |S_1(\theta)|^2 = |G^{-1}(\theta)|^2, \tag{1.8}$$

where $G^{-1}(\theta)$ designates the inverse Fourier transform of $g(p)$, $\mathcal{F}^{-1}\{g(p)\}$. With the help of the Wiener-Khitchine theorem (see Refs.[28, 20]) the autocorrelation, symbolized by \odot , of $g(p)$ becomes

$$g(p) \odot g^*(p) = \mathcal{F}^{-1}\{|G(\theta)|^2\}, \tag{1.9}$$

where $*$ denotes the complex conjugate. This leads to the spectrum, $|\mathcal{F}\{i_1(\theta)\}|^2$:

$$|\mathcal{F}\{i_1(\theta)\}|^2 = |\mathcal{F}\{|G^{-1}(\theta)|^2\}|^2 = |\mathcal{F}^{-1}\{|G(\theta)|^2\}|^2 = |g(p) \odot g^*(p)|^2. \tag{1.10}$$

Hence the spectrum is the magnitude squared of the auto-correlation of the glare point pattern. This alternative interpretation is not different with regard to the

previous one. In particular Eq. 1.7 has been employed by Lock[36, 37] and Van de Hulst and Wang[84] to gain better insight in the glare points seen at the edges of the droplet at almost any scattering angle.

1.4 Thesis overview

The development of a laser-based measurement instrument is the subject of the thesis. The main purpose of the instrument is the non-intrusive measurement of the temperature of a single droplet in a spray. Therefore, a remote sensing principle is employed, based on the monochromatic rainbow described in Sec. 1.3.

Chap. 2 deals with the Lorenz-Mie theory used for the prediction of the monochromatic rainbow characteristics from a homogeneous sphere, necessary for the development of the rainbow technique. A simple extension of the Lorenz-Mie theory is attempted which enables the computation of the primary monochromatic rainbow for a sphere arbitrarily located in an off-axis Gaussian laser beam.

The behaviour of the rainbow pattern for non-spherical droplets is treated in Chap. 3. The Airy fringes and ripple structure are computed for the specific case of an ellipsoidal droplet with a constant and real refractive index. A comparison with the Lorenz-Mie theory will be made concerning spheres to validate the developed theoretical approach.

Chap. 4 examines the limits of the Airy theory by comparing it with the Lorenz-Mie theory.

Chap. 5 explains how from an angular rainbow pattern, recorded with a linear CCD-camera both the temperature and size of the light-scattering droplet can be determined. It also demonstrates how the influence of the drop non-sphericity on these parameters is circumvented. Experiments on satellite droplets around an unstable water jet will be shown.

Chap. 6 will deal with the simultaneous measurement of the temperature, size and velocity of an individual droplet using a single photomultiplier to detect a time-varying rainbow pattern. Experimental results carried out in a full-cone water spray are reported as well as the detection of non-sphericity.

The discussion and conclusions follow in Chap. 7.

Chapter 2

OFF-AXIS LASER-BEAM SCATTERING BY A SPHERE USING LORENZ-MIE THEORY

It is a challenge to characterize particles in a fluid flow without disturbing the phenomenon that is being surveyed. Therefore optical techniques are applied based on the detection of light scattered by particles. To relate the detected spatial or temporal intensity distribution to a certain physical quantity, all kind of scattering theories can be utilized. In this chapter light will be treated as electromagnetic waves. The scattering problem is defined in Sec. 2.1 and solved in Sec. 2.2. The result is known as the Lorenz-Mie theory and gives an exact solution for spherical particles of arbitrary size. In Sec. 2.3 the far-field solution is derived and Sec. 2.4 treats the localization principle.

The rainbow technique utilizes laser-light illumination. This means that the incident wave-front has a non-uniform light-intensity distribution unlike in the Lorenz-Mie theory. Moreover, when the sphere is not located on the laser-beam axis, the scattering problem loses its axial symmetry. An extension of the Lorenz-Mie theory is proposed in Sec. 2.5 concerning the specific situation of the off-axis illumination by a laser beam with a Gaussian intensity profile.

2.1 Definition of the scattering problem for Lorenz-Mie theory

The considered problem is sketched in Fig. 2.1. A planar monochromatic wave front is impinging on a sphere. The light wave consists of the mutually perpendicular electric field \mathbf{E} and magnetic field intensity \mathbf{H} . The medium inside (denoted by subscript i) and outside the particle (subscript o) is homogeneous and free of charges. In that case, the electromagnetic field (\mathbf{E}, \mathbf{H}) has to satisfy the Maxwell

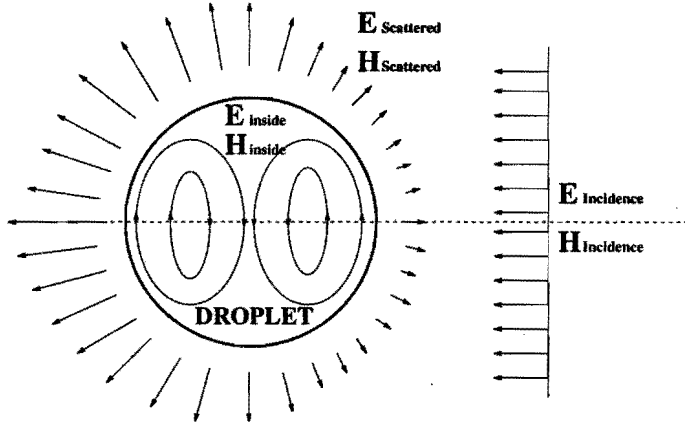


Figure 2.1: Sketch of the Scattering Problem by a Sphere

equations that Hecht[29] writes in the following differential form, applying SI-units:

$$\nabla \cdot \mathbf{E} = 0, \quad (2.1)$$

$$\nabla \cdot \mathbf{H} = 0, \quad (2.2)$$

$$\nabla \times \mathbf{E} = -\mu \frac{\partial \mathbf{H}}{\partial t}, \quad (2.3)$$

$$\nabla \times \mathbf{H} = \epsilon \frac{\partial \mathbf{E}}{\partial t}. \quad (2.4)$$

μ is the permeability and ϵ denotes the electric permittivity of the particular medium. Eqs. 2.1 and 2.2 describe the divergence-free conditions of the (\mathbf{E}, \mathbf{H}) -field and the other two Maxwell equations express the mutual dependence between both vectors. Based on the vector identity $\nabla \times \nabla \times \mathbf{A} = -\Delta \mathbf{A} + \nabla(\nabla \cdot \mathbf{A})$, above relations transform into the vector wave equations:

$$\Delta \mathbf{E} - \mu \epsilon \frac{\partial^2 \mathbf{E}}{\partial t^2} = 0, \quad (2.5)$$

$$\Delta \mathbf{H} - \mu \epsilon \frac{\partial^2 \mathbf{H}}{\partial t^2} = 0. \quad (2.6)$$

Consider an electromagnetic field that is time harmonic,

$$\mathbf{E} = \mathcal{E} e^{-i\omega t}, \quad (2.7)$$

$$\mathbf{H} = \mathcal{H} e^{-i\omega t}, \quad (2.8)$$

where ω is the circular frequency of the light being equal inside and outside the sphere. Then Eqs. 2.5 and 2.6 lead to the following two Helmholtz equations:

$$\Delta \mathcal{E} + k^2 \mathcal{E} = 0, \quad (2.9)$$

$$\Delta \mathcal{H} + k^2 \mathcal{H} = 0. \quad (2.10)$$

The wavenumber k is defined as

$$k = \omega \sqrt{\mu \epsilon} = \omega \frac{m}{c} = \frac{2\pi}{\lambda} m. \tag{2.11}$$

λ is the wavelength and c the speed of light in vacuum whereas the refractive index of the medium is assigned to m . Note that \mathcal{E} and \mathcal{H} are complex vector functions representing the complex space part of the waves.

Eqs. 2.7 and 2.8 are the wave equations to be solved for the incident and scattered field and the field inside the sphere. These three fields are connected by the boundary conditions described at the interface between the two media. Gauss's divergence theorem, $\oint \mathbf{A} \cdot \mathbf{n} \, da = \iiint \nabla \cdot \mathbf{A} \, d^3x$, applied to the divergence-free conditions (Eqs. 2.1 and 2.2), leads to the condition that the normal components of the considered vector functions are continuous over the interface:

$$\mathcal{E}_i \cdot \mathbf{e}_r = (\mathcal{E}_s + \mathcal{E}_b) \cdot \mathbf{e}_r, \tag{2.12}$$

$$\mathcal{H}_i \cdot \mathbf{e}_r = (\mathcal{H}_s + \mathcal{H}_b) \cdot \mathbf{e}_r. \tag{2.13}$$

$i \rightarrow$ pertains to the field inside the sphere

$b \rightarrow$ pertains to the incident field

$s \rightarrow$ pertains to the scattered field

\mathbf{e}_r is the unit vector in the radial direction which is normal to the interface in this particular case. The boundary conditions for the tangential components of the electromagnetic field are found by applying Stokes' theorem, $\oint \mathbf{A} \cdot d\mathbf{r} = \iint \nabla \times \mathbf{A} \cdot \mathbf{n} \, da$, to Maxwell's Eqs. 2.3 and 2.4:

$$\mathcal{E}_i \times \mathbf{e}_r = (\mathcal{E}_s + \mathcal{E}_b) \times \mathbf{e}_r, \tag{2.14}$$

$$\mathcal{H}_i \times \mathbf{e}_r = (\mathcal{H}_s + \mathcal{H}_b) \times \mathbf{e}_r. \tag{2.15}$$

By solving the Helmholtz equations with the proper boundary conditions, the amplitude of the electromagnetic field (\mathcal{E}, \mathcal{H}) is obtained, everywhere inside and outside the sphere. But a photomultiplier, a CCD camera or a film plate detects the radiant energy that is transported by the (\mathbf{E}, \mathbf{H})-field. Because this energy flux is fluctuating in time at optical frequencies, the quantity measured by the detector is an averaged energy, which is known as irradiance. It is often simply denoted as the intensity which reads (Stratton[66])

$$I = \langle \mathbf{E} \times \mathbf{H} \rangle, \tag{2.16}$$

where $\langle \dots \rangle$ symbolizes the time-averaging. In most applications, one is interested in the so-called far-field intensity. This can be expressed in terms of the electric field only (see for example Gouesbet et al.[21]):

$$I = \frac{\epsilon c}{m} \langle \text{Re}(\mathbf{E}) \cdot \text{Re}(\mathbf{E}) \rangle. \tag{2.17}$$

Since $\text{Re}(\mathbf{E}) = \frac{1}{2}(\mathbf{E} + \mathbf{E}^*)$ (where \mathbf{E}^* denotes the complex conjugate of \mathbf{E}), the far-field expression can be written as

$$I = \frac{1}{2} \frac{\epsilon c}{m} \mathcal{E}^* \cdot \mathcal{E} \tag{2.18}$$

after substitution of \mathbf{E} by $\mathcal{E} e^{-i\omega t}$ and then performing the time-averaging.

2.2 Solution of the scattering problem

When treating light as electromagnetic waves, the irradiance (Eq. 2.16) inside and outside the sphere, illuminated by a planar wave front, can be found by looking for expressions for the vector functions \mathcal{E} and \mathcal{H} . Therefore the Helmholtz equations 2.9 and 2.10 have to be solved with the appropriate boundary conditions at the interface. The solution was found by Lorenz[41] and Mie[47]. It is now referred to as the Lorenz-Mie theory and has been described later in numerous books on light scattering such as those of Van de Hulst[79] and Bohren and Huffman[9]. It is this set of references that served in a large extent for the construction of this section.

The Lorenz-Mie theory expresses the $(\mathcal{E}, \mathcal{H})$ -field in a scalar function Ψ which is a solution of the scalar wave equation. As such the problem of solving two vector wave equations is reduced to seeking the solution to only one scalar wave equation. In order to achieve this, the following two time harmonic vector functions \mathbf{M} and \mathbf{N} have to be introduced:

$$\mathbf{M} = \mathcal{M}e^{-i\omega t}, \quad (2.19)$$

$$\mathbf{N} = \mathcal{N}e^{-i\omega t}, \quad (2.20)$$

$$\mathcal{M} = \nabla \times (\mathbf{r}\Psi), \quad (2.21)$$

$$\mathcal{N} = \frac{\nabla \times \mathcal{M}}{k}, \quad (2.22)$$

$$\mathcal{M} = \frac{\nabla \times \mathcal{N}}{k}. \quad (2.23)$$

Note that \mathcal{M} is perpendicular to the radial vector \mathbf{r} , which is convenient when taking the curl of \mathcal{M} in spherical coordinates to calculate \mathcal{N} . Moreover, because the divergence of the curl of any vector vanishes, both \mathcal{M} and \mathcal{N} are divergence free:

$$\nabla \cdot \mathbf{M} = 0, \quad (2.24)$$

$$\nabla \cdot \mathbf{N} = 0. \quad (2.25)$$

They also satisfy the Helmholtz equations

$$\Delta \mathcal{M} + k^2 \mathcal{M} = 0, \quad (2.26)$$

$$\Delta \mathcal{N} + k^2 \mathcal{N} = 0, \quad (2.27)$$

if the scalar function Ψ is the solution of the scalar wave equation

$$\Delta \Psi + k^2 \Psi = 0. \quad (2.28)$$

Comparing above relations for the $(\mathcal{M}, \mathcal{N})$ -field to those for the $(\mathcal{E}, \mathcal{H})$ -field (previous section) reveals that the vector functions \mathcal{M} and \mathcal{N} have all the properties of an electromagnetic field. This field can be computed by solving Eq. 2.28.

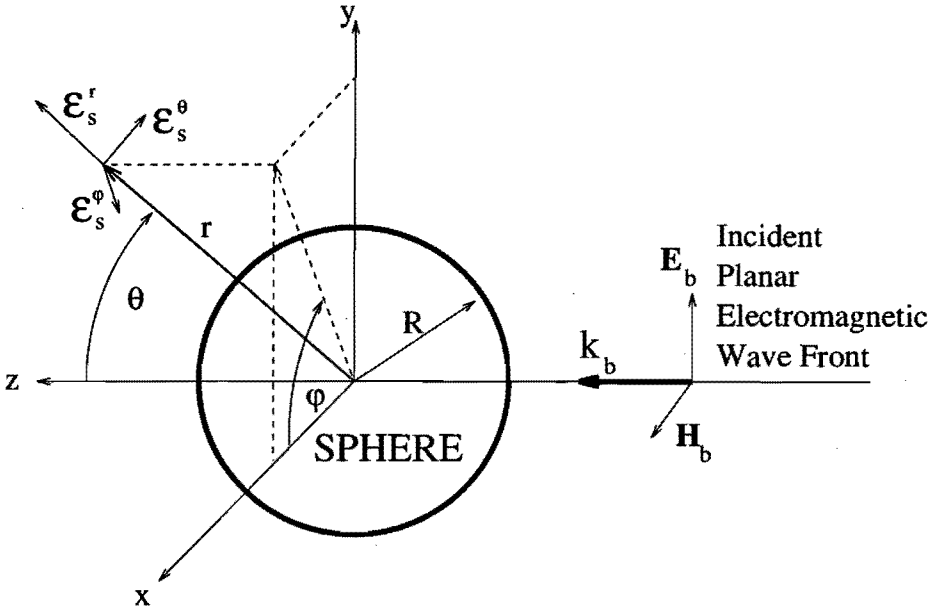


Figure 2.2: Definition of the coordinate system for the scattering problem. $(\mathbf{E}_b, \mathbf{H}_b)$ represents the incident electromagnetic field. $\mathcal{E}_s^r, \mathcal{E}_s^\theta$ and \mathcal{E}_s^φ are the three components of the space part of the scattered electric field in polar spherical coordinates. The scattering plane is taken through the directions of the incident beam and the scattered wave at a certain point (r, θ, φ) .

The spherical symmetry of the problem dictates the obvious choice of spherical polar coordinates (r, θ, φ) as defined in Fig 2.2. Subsequently, separation of variables yields the general solution of the Helmholtz equation 2.28, which is expressed as a linear combination of elementary solutions:

$$\Psi = \sum_{l=0}^{\infty} \sum_{n=l}^{\infty} A_{ln} \cos(l\varphi) P_n^l(\cos \theta) z_n(kr) + B_{ln} \sin(l\varphi) P_n^l(\cos \theta) z_n(kr) \quad (2.29)$$

where l and n are integers. A_{ln} and B_{ln} are the coefficients in the expansion. P_n^l is the associated Legendre polynomial and $z_n(kr)$ is any spherical Bessel function. In principle, a general expression for \mathcal{M} could now be constructed for the incident, internal and scattered field by substituting Ψ in Eq. 2.21; \mathcal{N} follows then from Eq. 2.22. However, this would be not sufficient because the irradiance I requires the electromagnetic field to be expressed in the vector pair $(\mathcal{E}, \mathcal{H})$. Therefore, as both $(\mathcal{E}, \mathcal{H})$ and $(\mathcal{M}, \mathcal{N})$ describe the same field, \mathcal{E} and \mathcal{H} have to be written as a linear combination of \mathcal{M} and \mathcal{N} . Consequently, the general expression for $(\mathcal{E}, \mathcal{H})$ implies 4 expansion coefficients (with indices l and n) for each electric field $\mathcal{E}_b, \mathcal{E}_s$ and \mathcal{E}_i ; the magnetic-field vector functions are coupled to the \mathcal{E} -field by the third Maxwell equation (Eq. 2.3).

The incident field \mathcal{E}_b

For the incident field \mathcal{E}_b , the 4 expansion coefficients are dictated by the imposed plane wave which is linearly polarized in the x-direction:

$$\mathcal{E}_b = E_b e^{ik_o z} \mathbf{e}_x. \quad (2.30)$$

k_o is the wave number outside the particle (i.e. $k_o = \frac{2\pi}{\lambda} m_o$). The amount of expansion coefficients is reduced because of the orthogonality within the set of elementary functions. This set and the choice of $e^{-i\omega t}$ as the time-dependent part of the waves determines the actual values of the remaining coefficients. After solving several integrals, which have been thoroughly described by Bohren and Huffman[9] and will not be treated here, the expression for \mathcal{E}_b in polar spherical coordinates reads

$$\mathcal{E}_b = \mathcal{M}_{v_b} - i\mathcal{N}_{u_b}, \quad (2.31)$$

and the magnetic-field intensity holds

$$\mathcal{H}_b = -\frac{k_o}{\mu_o \omega} (\mathcal{M}_{u_b} + i\mathcal{N}_{v_b}). \quad (2.32)$$

u_b and v_b designate the reduced scalar functions that have to be substituted for Ψ in Eqs. 2.21 and 2.22 to construct the vector functions \mathcal{M} and \mathcal{N} for the incident field:

$$u_b = E_b \cos \varphi \sum_{n=1}^{\infty} i^n \frac{2n+1}{n(n+1)} P_n^1(\cos \theta) j_n(k_o r), \quad (2.33)$$

$$v_b = E_b \sin \varphi \sum_{n=1}^{\infty} i^n \frac{2n+1}{n(n+1)} P_n^1(\cos \theta) j_n(k_o r). \quad (2.34)$$

j_n is the spherical Bessel function that is derived from the Bessel function of the first kind $J_{n+\frac{1}{2}}$:

$$j_n(\rho) = \sqrt{\frac{\pi}{2kr}} J_{n+\frac{1}{2}}(\rho). \quad (2.35)$$

Here the dimensionless variable $\rho = kr$ has been introduced. It is this Bessel function that has to be used for the incident field because the Bessel function of the second kind is not finite at the origin. Note that u_b and v_b are orthogonal because $\cos \varphi$ and $\sin \varphi$ are mutually so. E_b is the amplitude of the electric field. Now, one could verify, by substitution of u_b and v_b for Ψ in Eqs. 2.21 and 2.22, that relationship 2.31 describes a simple x-polarized plane wave.

The scattered field \mathcal{E}_s

The scattered field is connected to the imposed incident field by means of the boundary conditions at the interface between the media, i.e. continuity of all the field-components over the surface. This implies that the scalar functions for the scattered field, u_s and v_s , are proportional to u_b and v_b respectively:

$$u_s = E_b \cos \varphi \sum_{n=1}^{\infty} a_n i^n \frac{2n+1}{n(n+1)} P_n^1(\cos \theta) h_n^{(1)}(k_o r), \quad (2.36)$$

$$v_s = E_b \sin \varphi \sum_{n=1}^{\infty} b_n i^n \frac{2n+1}{n(n+1)} P_n^1(\cos \theta) h_n^{(1)}(k_o r). \quad (2.37)$$

Therefore the scattering coefficients a_n and b_n for the scattered field were introduced. Note the use of the first spherical Hankel function $h_n^{(1)}$ as elementary solution for the r-equation of differential Eq. 2.28:

$$h_n^{(1)}(\rho) = j_n(\rho) + i y_n(\rho) \xrightarrow{\rho \gg n^2} \frac{(-i)^n e^{i\rho}}{i\rho}. \quad (2.38)$$

$y_n(\rho)$ is the spherical Bessel function of the second kind. This Hankel function is used because it makes $\mathbf{E} = \mathcal{E} e^{-i\omega t}$ to an outgoing wave at large distance from the particle, as the scattered wave is supposed to be. From Eqs. 2.21, 2.22, 2.31, 2.36 and 2.37, the θ -, φ - and r -components of \mathcal{E}_s are obtained, that is to say, \mathcal{E}_s^θ , \mathcal{E}_s^φ and \mathcal{E}_s^r , respectively:

$$\mathcal{E}_s^\theta = \mathcal{M}_{v_s}^\theta - i \mathcal{N}_{u_s}^\theta, \quad (2.39)$$

$$\mathcal{M}_{v_s}^\theta = E_b \cos \varphi \sum_{n=1}^{\infty} b_n i^n \frac{2n+1}{n(n+1)} \pi_n(\cos \theta) h_n^{(1)}(k_o r),$$

$$\mathcal{N}_{u_s}^\theta = E_b \cos \varphi \sum_{n=1}^{\infty} a_n i^n \frac{2n+1}{n(n+1)} \tau_n(\cos \theta) \left[h_{n-1}^{(1)}(k_o r) - \frac{n h_n^{(1)}(k_o r)}{k_o r} \right],$$

$$\mathcal{E}_s^\varphi = \mathcal{M}_{v_s}^\varphi - i \mathcal{N}_{u_s}^\varphi, \quad (2.40)$$

$$\mathcal{M}_{v_s}^\varphi = E_b \sin \varphi \sum_{n=1}^{\infty} b_n i^n \frac{2n+1}{n(n+1)} \tau_n(\cos \theta) h_n^{(1)}(kr),$$

$$\mathcal{N}_{u_s}^\varphi = E_b \sin \varphi \sum_{n=1}^{\infty} a_n i^n \frac{2n+1}{n(n+1)} \pi_n(\cos \theta) \left[h_{n-1}^{(1)}(k_o r) - \frac{n h_n^{(1)}(k_o r)}{k_o r} \right],$$

$$\mathcal{E}_s^r = \mathcal{M}_{v_s}^r - i \mathcal{N}_{u_s}^r, \quad (2.41)$$

$$\mathcal{M}_{v_s}^r = 0,$$

$$\mathcal{N}_{u_s}^r = E_b \cos \varphi \sum_{n=1}^{\infty} a_n i^n (2n+1) P_n^1(\cos \theta) \frac{h_n^{(1)}(k_o r)}{k_o r}.$$

The expressions for the magnetic-field intensity follow from Eq. 2.32. The functions π_n and τ_n (with argument $\cos \theta$) were defined as

$$\pi_n \equiv \frac{P_n^1}{\sin \theta} = \frac{2n-1}{n-1} \cos \theta \pi_{n-1} - \frac{n}{n-1} \pi_{n-2}, \quad (2.42)$$

$$\tau_n \equiv \frac{d}{d\theta} P_n^1 = n \cos \theta \pi_n - (n+1) \pi_{n-1}. \quad (2.43)$$

Furthermore, the following recurrence relation was applied:

$$\frac{1}{\rho} \frac{d}{d\rho} \rho z_n(\rho) = z_{n-1}(\rho) - \frac{n z_n(\rho)}{\rho}. \quad (2.44)$$

The internal field \mathcal{E}_i

u_i and v_i for the internal field are, due to the boundary conditions at the interface, proportional to u_b and v_b of the imposed incident electromagnetic wave:

$$u_i = E_b \cos \varphi \sum_{n=1}^{\infty} c_n i^n \frac{2n+1}{n(n+1)} P_n^1(\cos \theta) j_n(k_o r), \quad (2.45)$$

$$v_i = E_b \sin \varphi \sum_{n=1}^{\infty} d_n i^n \frac{2n+1}{n(n+1)} P_n^1(\cos \theta) j_n(k_o r). \quad (2.46)$$

Here c_n and d_n are the coefficients for the internal field. As for the incident field, the Bessel function $j_n(k_o r)$ is applied because it is finite at the origin which condition the internal field evidently has to satisfy. The components of \mathcal{E}_i have not been written out here but can be found with the help of the Eqs. 2.21, 2.22, 2.31 and above expressions for u_i and v_i . An interesting survey on the internal light intensity distribution of illuminated droplets has been carried out by Lock and Hovenac[40] using the Lorenz-Mie coefficients c_n and d_n .

Determination of coefficients a_n , b_n , c_n and d_n

The last task is the determination of the coefficients a_n , b_n , c_n and d_n . Therefore, four independent equations are required which are constructed from the boundary conditions (Eqs. 2.12, 2.13, 2.14 and 2.15). First, to simplify the notation, the Riccati-Bessel functions $\psi_n(\rho)$ and $\zeta_n(\rho)$ are introduced:

$$\psi_n(\rho) = \rho j_n(\rho), \quad (2.47)$$

$$\zeta_n(\rho) = \rho h_n^{(1)}(\rho). \quad (2.48)$$

This notation is convenient for the tangential components of the vector function \mathcal{N} as it contains terms like $\frac{1}{\rho} \frac{d}{d\rho} (\rho j_n(\rho))$. The next definitions of the size parameters x and y are based on the fact that for the boundary conditions the radial coordinate r equals the radius R of the sphere:

$$x = k_o R = \frac{2\pi R}{\lambda} m_o, \quad (2.49)$$

$$y = k_i R = \frac{2\pi R}{\lambda} m_i. \quad (2.50)$$

The continuity at the sphere surface, concerning the normal field components, leads to

$$\mathcal{E}_s^r + \mathcal{E}_b^r = \mathcal{E}_i^r \Rightarrow b_n \frac{\zeta_n(x)}{m_o} + \frac{\psi_n(x)}{m_o} = d_n \frac{\psi_n(y)}{m_i}, \quad (2.51)$$

$$\mathcal{H}_s^r + \mathcal{H}_b^r = \mathcal{H}_i^r \Rightarrow a_n \frac{\zeta_n(x)}{\mu_o} + \frac{\psi_n(x)}{\mu_o} = c_n \frac{\psi_n(y)}{\mu_i}, \quad (2.52)$$

where μ_o and μ_i are the permeability outside and inside the sphere, respectively. Notice that here the magnetic field intensity starts to play a role. This field is also applied to find the last two equations needed to solve the coefficients a_n , b_n , c_n and d_n . These equations are deduced by subtraction of above equations (times $\alpha = \left(\frac{n(n+1)}{r_n} P_n^1\right)^{-1}$) from the expressions describing the continuity of the θ -component of the electromagnetic field over the particle surface:

$$\mathcal{E}_s^\theta - \alpha \mathcal{E}_s^r + \mathcal{E}_b^\theta - \alpha \mathcal{E}_b^r = \mathcal{E}_i^\theta - \alpha \mathcal{E}_i^r \Rightarrow a_n \frac{\zeta_n'(x)}{m_o} + \frac{\psi_n'(x)}{m_o} = c_n \frac{\psi_n'(y)}{m_i}, \quad (2.53)$$

$$\mathcal{H}_s^\theta - \alpha \mathcal{H}_s^r + \mathcal{H}_b^\theta - \alpha \mathcal{H}_b^r = \mathcal{H}_i^\theta - \alpha \mathcal{H}_i^r \Rightarrow b_n \frac{\zeta_n'(x)}{\mu_o} + \frac{\psi_n'(x)}{\mu_o} = d_n \frac{\psi_n'(y)}{\mu_i}. \quad (2.54)$$

The prime ' at the Riccati-Bessel functions denotes the first derivative. Eqs. 2.51, 2.52, 2.53 and 2.54 combine to a set of linear equations,

$$\begin{pmatrix} 0 & \frac{\zeta_n(x)}{m_o} & 0 & -\frac{\psi_n(y)}{m_i} \\ \frac{\zeta_n(x)}{\mu_o} & 0 & -\frac{\psi_n(x)}{\mu_o} & 0 \\ \frac{\zeta_n'(x)}{m_o} & 0 & -\frac{\psi_n'(y)}{m_i} & 0 \\ 0 & \frac{\zeta_n'(x)}{\mu_o} & 0 & -\frac{\psi_n'(y)}{\mu_i} \end{pmatrix} \begin{pmatrix} a_n \\ b_n \\ c_n \\ d_n \end{pmatrix} = \begin{pmatrix} -\frac{\psi_n(x)}{m_o} \\ -\frac{\psi_n(x)}{\mu_o} \\ -\frac{\psi_n'(x)}{m_o} \\ -\frac{\psi_n'(x)}{\mu_o} \end{pmatrix}, \quad (2.55)$$

which is solved for its coefficients:

$$a_n = \frac{\psi_n(x)\psi_n'(y) - \psi_n(y)\psi_n'(x) \frac{\mu_o m_i}{\mu_i m_o}}{\psi_n(y)\zeta_n'(x) - \zeta_n(x)\psi_n'(y) \frac{\mu_o m_i}{\mu_i m_o}}, \quad (2.56)$$

$$b_n = \frac{\psi_n(x)\psi_n'(y) - \psi_n(y)\psi_n'(x) \frac{\mu_i m_o}{\mu_o m_i}}{\psi_n(y)\zeta_n'(x) - \zeta_n(x)\psi_n'(y) \frac{\mu_i m_o}{\mu_o m_i}}, \quad (2.57)$$

$$c_n = \frac{\psi_n(x)\zeta_n'(x) - \psi_n'(x)\zeta_n(x)}{\psi_n(y)\zeta_n'(x) \frac{\mu_o}{\mu_i} - \zeta_n(x)\psi_n'(y) \frac{m_o}{m_i}}, \quad (2.58)$$

$$d_n = \frac{\psi_n(x)\zeta_n'(x) - \psi_n'(x)\zeta_n(x)}{\psi_n(y)\zeta_n'(x) \frac{m_o}{m_i} - \zeta_n(x)\psi_n'(y) \frac{\mu_o}{\mu_i}}. \quad (2.59)$$

This completes the general solution of the problem defined in Sec 2.1. For dielectric media the expressions for the coefficients simplify somewhat because $\mu_o = \mu_i$.

2.3 Far-field approximation

The detection of scattered light often takes place at a very large distance from the particle. There, the expressions for the electric-field components, Eqs. 2.39, 2.40 and 2.41, simplify to the far-field approximation. In fact, it was already mentioned in the previous section that the spherical Hankel function $h_n^{(1)}(\rho)$, used to describe the scattered field $(\mathbf{E}_s, \mathbf{H}_s)$, takes its asymptotic expression provided that $k r \gg n^2$, which is the condition for far-field scattering. Upon substitution of the asymptotic expression (Eq. 2.38) in the electric-field components, Eqs. 2.39, 2.40 and 2.41 reduce to:

$$\mathcal{E}_s^\theta = -iE_b \cos \varphi \frac{e^{ik_0 r}}{k_0 r} \sum_{n=1}^{\infty} \frac{2n+1}{n(n+1)} [a_n \tau_n(\cos \theta) + b_n \pi_n(\cos \theta)], \quad (2.60)$$

$$\mathcal{E}_s^\varphi = -iE_b \sin \varphi \frac{e^{ik_0 r}}{k_0 r} \sum_{n=1}^{\infty} \frac{2n+1}{n(n+1)} [a_n \pi_n(\cos \theta) + b_n \tau_n(\cos \theta)], \quad (2.61)$$

$$\mathcal{E}_s^r = 0. \quad (2.62)$$

Consequently, the electromagnetic field in the far field is an outgoing spherical wave because $\mathcal{E}_s^r = 0$. In the literature, the non-dimensional Lorenz-Mie amplitude

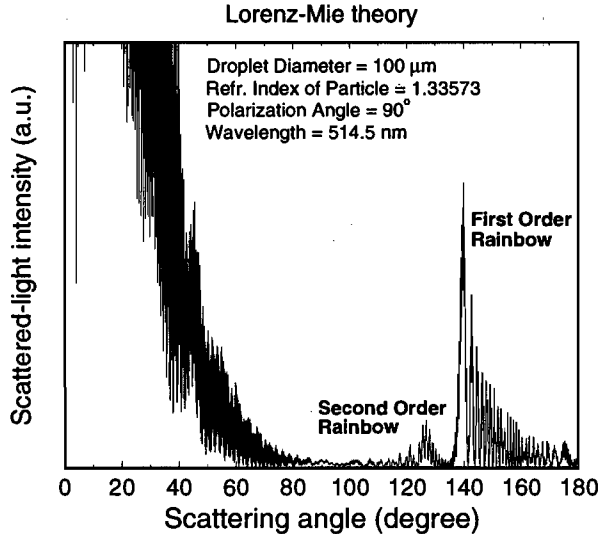


Figure 2.3: The angular scattered-light distribution in the far field for a spherical droplet of $100 \mu\text{m}$ according to the Lorenz-Mie theory.

functions S_1 and S_2 are extensively tabulated:

$$S_1 = \sum_{n=1}^{\infty} \frac{2n+1}{n(n+1)} [a_n \pi_n(\cos \theta) + b_n \tau_n(\cos \theta)], \quad (2.63)$$

$$S_2 = \sum_{n=1}^{\infty} \frac{2n+1}{n(n+1)} [a_n \tau_n(\cos \theta) + b_n \pi_n(\cos \theta)]. \quad (2.64)$$

It is important to note that S_1 pertains to \mathcal{E}_s^φ and that this electric field component is normal to the scattering plane that is taken through the centre of the sphere, the sensor and through the incident beam. S_2 pertains to \mathcal{E}_s^θ and lies in the scattering plane.

$i_1(\theta)$ and $i_2(\theta)$ are the far-field normalized intensities

$$i_1 = |S_1|^2, \quad (2.65)$$

$$i_2 = |S_2|^2. \quad (2.66)$$

For linearly-polarized light in the x-direction (as in Fig. 2.2), the detected light intensity I in a certain point (r, θ, φ) follows from Eq. 2.18 and above relations as

$$I = [i_1(\theta) \sin^2 \varphi + i_2(\theta) \cos^2 \varphi] \frac{I_b}{(k_0 r)^2}, \quad (2.67)$$

where I_b denotes the intensity of the incident light. Fig. 2.3 shows the angular scattered-light intensity as a function of the scattering angle for $0^\circ < \theta < 180^\circ$. The incident light is polarized normal to the scattering plane, i.e. $\varphi = 90^\circ$. Therefore, only the intensity i_1 had to be computed. Notice that in the back-scattered region the primary and secondary rainbow are identified.

2.4 Localization principle

The Lorenz-Mie theory expresses the scattering amplitude S_1 (and S_2) in an infinite sum of partial waves C_n

$$S_1 = \sum_{n=1}^{\infty} C_n, \quad (2.68)$$

$$\text{with } C_n = \frac{2n+1}{n(n+1)} [a_n \pi_n(\cos \theta) + b_n \tau_n(\cos \theta)].$$

Fig. 2.4 shows $|C_n|$ for a sphere with size parameter $x = 745$ and a scattering angle $\theta = 139.7^\circ$, i.e. somewhere in the main rainbow maximum. The sharp drop near $x = n$ is remarkable and appears to be due to the asymptotic behaviour of the spherical Bessel functions in the Lorenz-Mie scattering coefficients a_n and b_n .

Van de Hulst[80] saw the analogy with quantum mechanics; there, an electron colliding with a centre of disturbance, can be interpreted either as a wave or a particle. Similarly, the partial waves in the Lorenz-Mie series can be related to

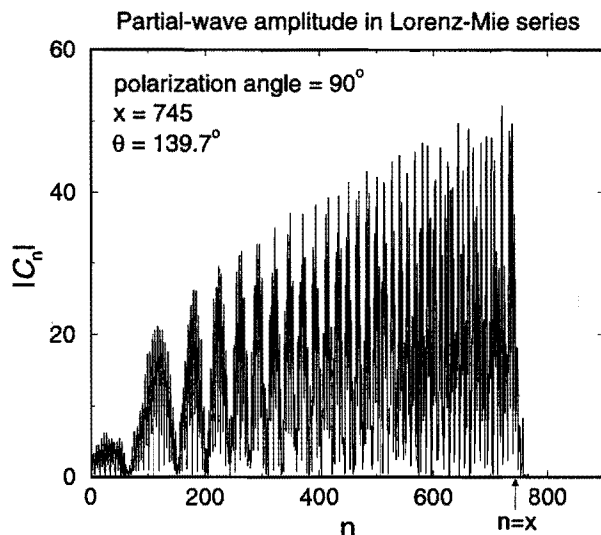


Figure 2.4: The amplitude of the complex term C_n in the Lorenz-Mie series as a function of the summation integer n for a size parameter $x = 745$.

geometrical rays. He stated that each term C_n corresponds to a ray at a distance $(n + \frac{1}{2})\frac{\lambda}{2\pi m_o}$ from the symmetry axis (Fig. 2.5). Consequently, for $n + \frac{1}{2} = x$ the partial wave C_n corresponds to a ray at grazing incidence and for $n + \frac{1}{2} < x$ the ray hits the sphere. The contribution of the terms with $n + \frac{1}{2} > x$ decreases

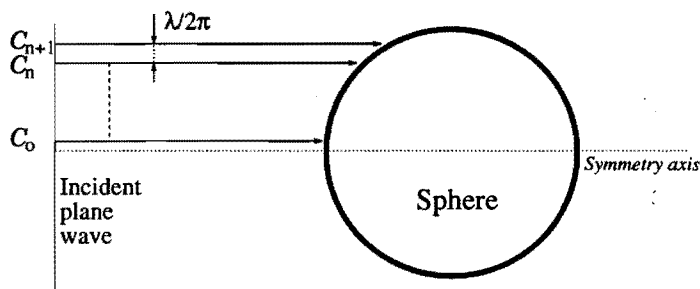


Figure 2.5: The localization principle: term C_n is related to a ray passing the origin of the sphere at a distance $(n + \frac{1}{2})\frac{\lambda}{2\pi}$. The refractive index outside the sphere, m_o , has been taken unity.

exponentially; these terms refer to rays beyond the edge of the sphere, giving rise to so-called surface waves (see Probert-Jones[58]). This interpretation of the partial waves was of great help for the computation of the infinite series. A survey

carried out by Wiscombe[89] revealed that the maximum integer, n_{max} , at which the partial-wave series can be cut off, equals

$$n_{max} \approx x + 4.3x^{\frac{1}{3}}. \quad (2.69)$$

The importance of the localization principle for the numerical prediction of spherical scattering phenomena can hardly be overestimated. It was therefore crucial that a rigorous justification of the principle was formulated in 1994 by Lock and Gouesbet[39] and Gouesbet and Lock[23] using the generalized Lorenz-Mie theory.

2.5 Off-axis laser-beam scattering

The scattering of laser-light by a spherical droplet can be treated by the Lorenz-Mie theory as well. Therefore, the theory has to be generalized so that the incident wave front represents the characteristics of a laser beam. This requires a description of the laser beam satisfying the Maxwell equations which leads to the non-plane-wave character with both axial and transverse field components. Moreover, when the intensity profile over the beam's cross section is Gaussian, then the beam possesses a waist with radius w_0 at a certain position along the axis (see Ref. [13]). Based on this description Gouesbet et al.[21] developed the generalized Lorenz-Mie theory (GLMT) which handles particles with arbitrary size having any location relative to the Gaussian beam (Fig. 2.6).

In many practical situations, the field components parallel to the direction of propagation of the laser light can be ignored; the beam reveals a plane-wave character with constant radius w . Moreover, when the droplet lies on the axis of the laser beam, then the scattering problem is axisymmetric like in the Lorenz-Mie theory. In order to account for the non-uniformity of the intensity profile, one simply multiplies each term C_n by the field amplitude at the position following the localization principle, introduced in the previous section. As a result, the far-field Lorenz-Mie amplitude S_1 transforms into

$$S_1 = \sum_{n=1}^{\infty} g_n C_n. \quad (2.70)$$

g_n is called the beam shape coefficient, which reads for a Gaussian beam

$$g_n = e^{-[b/w]^2} = e^{-[(n+\frac{1}{2})\frac{\lambda}{2\pi w}]^2}, \quad (2.71)$$

where the impact parameter b of a geometrical ray was introduced:

$$b = \frac{D}{2} \cos \tau \equiv (n + \frac{1}{2}) \frac{\lambda}{2\pi}. \quad (2.72)$$

Gréhan et al.[24] and Gouesbet et al.[22] demonstrated that the localization principle has a very large domain of validity concerning on-axis Gaussian illumination.

In this section an attempt is made to use the axisymmetric Lorenz-Mie theory in combination with the localization principle to model off-axis Gaussian illumination

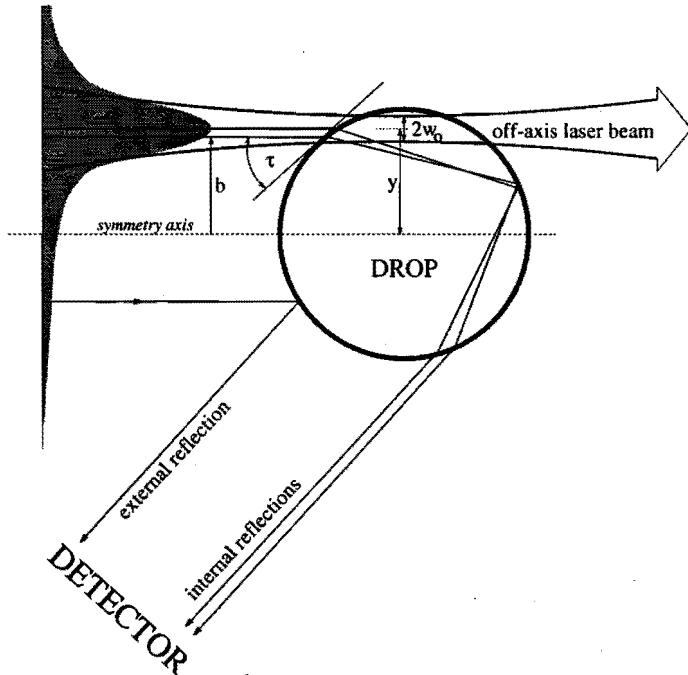


Figure 2.6: Off-axis laser-beam scattering treated by GLMT. The laser beam is Gaussian-shaped over its cross section and contains a waist radius w_0 . y is the off-axis distance between the centre of the laser beam and the centre of the drop. The geometrical rays contributing the most to the scattered-light intensity at the position of the detector have been traced. τ is the angle of incidence for a geometrical ray and b is the corresponding impact parameter (Eq. 2.72).

as sketched in Fig. 2.6. One aims at a simple approach which could serve as an alternative for the rigorous, but very complex, GLMT. It should agree with the latter as far as the scattered-light intensity in the primary rainbow is concerned.

Because the Lorenz-Mie theory can only handle symmetric scattering problems, one could first try to create a ring-shaped axisymmetric laser beam with its maximum intensity at a constant radius y , equaling the off-axis distance. The beam-shape coefficient for such a beam would be

$$g_n = e^{-[(n+\frac{1}{2})\frac{\lambda}{2\pi} - y]^2/w^2} \quad \text{for } n_{split} + 1 < n \leq n_{max}. \quad (2.73)$$

However, this attempt would fail because the contribution of external reflection to the rainbow would be overestimated, as can be derived from Fig. 2.8. To overcome this problem one has to take a look at Fig. 2.7. It shows that the ranges of impact parameters, related to the contributions of the different reflections to the rainbow,

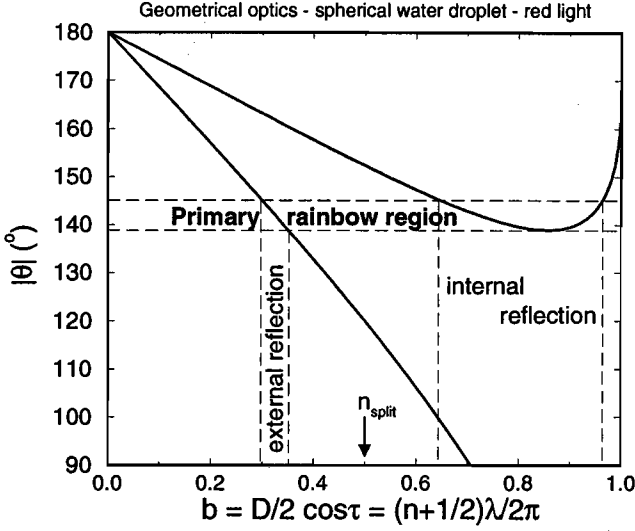


Figure 2.7: The relationship given by geometrical optics between the scattering angle and the impact parameter b (with $D/2 = 1$) for external and one internal reflection.

are well separated. Consequently, one can divide the sum of Eq. 2.70 in two parts:

$$S_1 = \sum_{n=1}^{n_{split}} g_n^{ext} C_n + \sum_{n=n_{split}+1}^{n_{max}} g_n^{int} C_n. \quad (2.74)$$

g_n^{int} refers to the beam shape coefficient in the range where internal reflection dominates whereas g_n^{ext} pertains to the coefficient that accounts for the influence of external reflection to the primary rainbow. n_{max} was already defined in Eq. 2.69. $C_{n_{split}}$ is assigned to a geometrical ray within the range of impact parameters that does not contribute to the primary rainbow. One can see in Fig. 2.7 that this interval is quite large. Thus, n_{split} can be put quite arbitrarily at

$$n_{split} = \frac{1}{2} n_{max}. \quad (2.75)$$

From Fig. 2.8 it is derived that g_n^{int} has to pertain to the intensity profile of the off-axis laser beam

$$g_n^{int} = e^{-[(n+\frac{1}{2})\frac{\lambda}{2\pi} - y]^2 / w^2} \quad \text{for } n_{split} + 1 < n \leq n_{max}. \quad (2.76)$$

The expression for g_n^{ext} is different because for external reflection the laser beam amplitude below the symmetry axis has to be taken:

$$g_n^{ext} = e^{-[(n+\frac{1}{2})\frac{\lambda}{2\pi} + y]^2 / w^2} \quad \text{for } 0 \leq n \leq n_{split}. \quad (2.77)$$

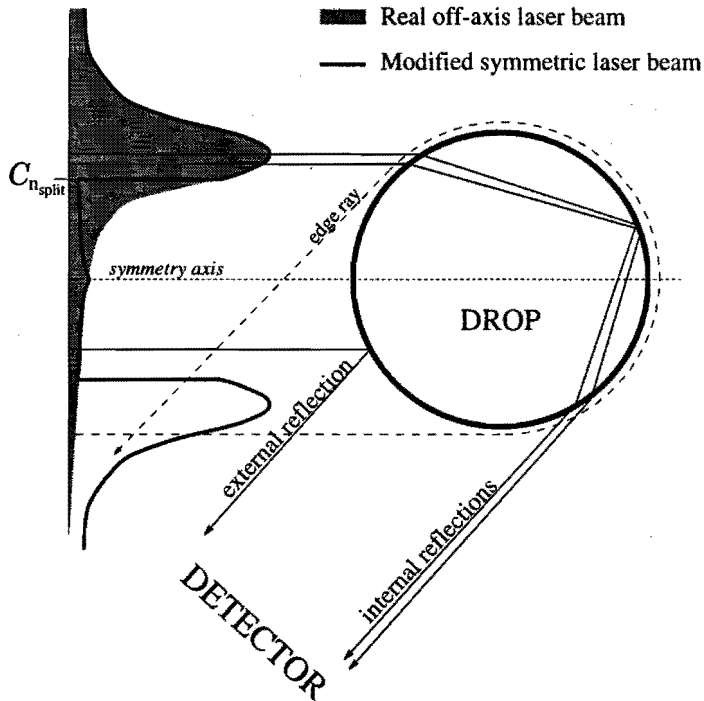


Figure 2.8: Off-axis scattering treated by the Lorenz-Mie theory combined with the localization principle. The approach implies an artificial symmetric laser-beam intensity profile. The main geometrical rays are traced that contribute to the scattered-light intensity at the position of the detector. The dashed rays represent an edge ray resulting from grazing incidence (See Chap. 1, Sec. 1.3)

This procedure leads to a ring-shaped laser beam with a discontinuity at the radius $(n_{split} + \frac{1}{2})\lambda/2\pi$, as depicted in Fig. 2.8. One has to realize that only in the rainbow region meaningful results can be obtained.

Fig. 2.9 depicts the primary rainbow for the case sketched in Fig. 2.6. The droplet diameter is $150\ \mu\text{m}$ and the wavelength is $632.8\ \text{nm}$. The off-axis distance measures $64\ \mu\text{m}$. The GLMT-curve has been computed employing the program *diagaus3.f* of Onofri et al.[57]. The narrow, focussed laser beam contains a waist diameter of $40\ \mu\text{m}$. For the localization approach the program *mie96.f* of Van Beeck[68] was utilized. Here, the beam has a constant diameter of $40\ \mu\text{m}$. As a reference case, a plane-wave scattering diagram has been plotted. The characteristics of the off-axis beam have been chosen such that the intensity of internally-reflected light prevails that of external reflection. The computation using GLMT gives the correct diagram revealing an interference pattern where the ripple structure has disappeared. For the localization approach, small undulations are still

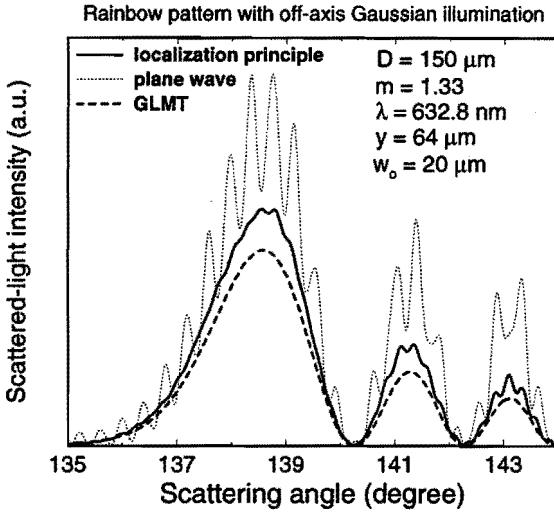


Figure 2.9: The rainbow pattern for an off-axis Gaussian laser beam. The distance between the centre of the laser beam and the symmetry axis is $y = 64 \mu\text{m}$. The three (normalized) curves result from computations using the Lorenz-Mie theory with localization principle, the reference case of plane-wave scattering and the rigorous GLMT.

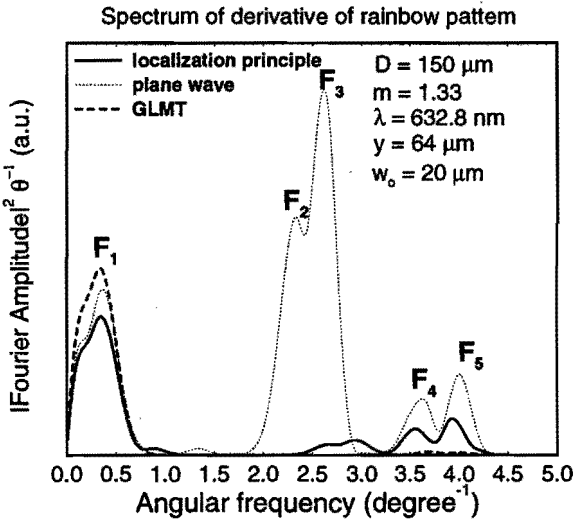


Figure 2.10: The spectrum of the scattering diagrams depicted in Fig. 2.9.

superimposed on the Airy fringes. To trace the origin of these wavelets, the power spectrum is calculated (Fig. 2.10), similarly to the survey in Sec. 1.3 in Chap. 1. The spectrum of the plane-wave rainbow resembles the one in Fig. 1.13, showing all five peaks labeled from F_1 to F_5 . For the GLMT-computation, only the peak corresponding to the Airy fringes, F_1 , remains. The curve with legend “localization principle” contains no peaks at F_2 and F_3 because they would result from interference between internal and external reflection, though the latter is absent. However, the Fourier amplitudes near F_4 and F_5 are clearly non-zero. In Sec. 1.3, it was concluded that these peaks have to result from interference between internal reflection and the edge-ray contribution to the rainbow. This edge ray arises due to an incoming ray at grazing incidence below the symmetry axis, schematically presented by the dashed ray in Fig. 2.8 which explains why there should not be any contribution at F_4 and F_5 . One could imagine to remove these peaks by modifying the beam shape coefficients near grazing incidence. Any attempt in this direction has failed so far; the amplitude of the undulations always increased. Apparently, sharp intensity changes, introduced in the artificial symmetric laser-beam, induces diffraction. In fact, the results of diffraction due to the discontinuity at n_{split} can be seen in the power spectrum, depicted in Fig. 2.10. The small peaks between $2.5^{\circ-1}$ and $3.2^{\circ-1}$ are not the left-overs of F_2 and F_3 but simply the results of interference between this diffraction and internally reflected rays. Namely, the structure moves when n_{split} is changed.

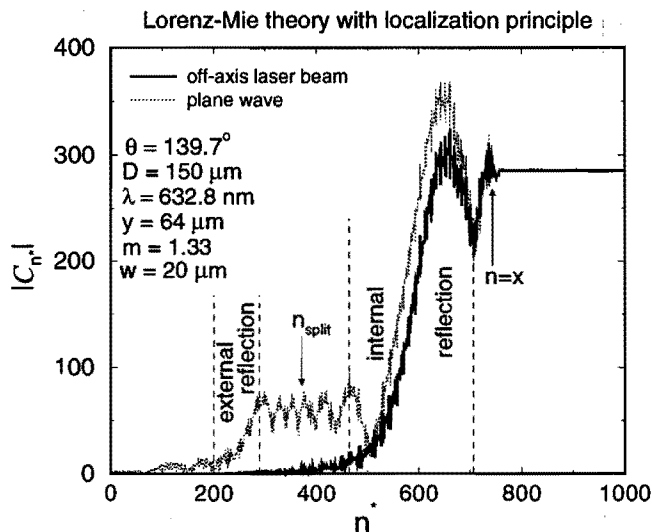


Figure 2.11: Illustration of the localized interpretation of the different terms in the Lorenz-Mie series by computing C_{n^*} instead of C_n (Eq. 2.78). Large jumps in the curves are related to geometrical rays.

In spite of the imperfections of the followed approach, one can nevertheless state that the localization principle is a powerful tool to predict in a easy manner the behaviour of the Airy fringes and the ripple structure in the primary rainbow when the Gaussian illumination of the droplet is not symmetric. One has to keep in mind though, that only the rigorous GLMT gives correct quantitative results.

At the end of this chapter, the evolution of the Lorenz-Mie series is shown in Fig. 2.11 for illustration purpose of the approach followed in this section. Plotting the amplitude of term C_n versus n , as was done in Fig. 2.4, would not reveal why a certain term would correspond to e.g. an externally-reflected ray. The reason for this is that both the phase and the amplitude of the successive terms change too rapidly. Therefore, the cumulative amplitude $|C_{n^*}|$ is computed:

$$C_{n^*} = \sum_{n=1}^{n^*} g_n C_n \quad \text{with } 0 \leq n^* \leq \infty. \quad (2.78)$$

where g_n denotes g_n^{ext} or g_n^{int} when $n < n_{split}$ or $n > n_{split}$, respectively. For $n^* = n_{max}$, C_{n^*} equals the Lorenz-Mie amplitude S_1 . The evolution of C_{n^*} is computed for plane-wave scattering and for the off-axis case treated throughout this section. Now, it is seen that a geometrical contribution to the scattered-light intensity is related to a jump in the evolution that brings C_{n^*} to another level. E.g. for the off-axis case, the jump around $n^* = 225$ is not present. This means that there was no contribution of external reflection as expected, thus demonstrating in a nice way the localization principle.

Chapter 3

SURFACE INTEGRAL METHOD FOR LIGHT SCATTERING BY ELLIPSOIDS

So far, only light scattering by spherical particles has been considered. In numerous applications the scattering particles are not spherical. It is therefore necessary to know the influence of the non-sphericity on the behaviour of the scattered-light intensity distribution. In this chapter, a theoretical approach will be presented and applied to the first-order rainbow formed by ellipsoids.

The approach starts by using ray optics to write an expression for the electromagnetic field just outside the scattering particle; here, phenomena such as the rainbow find their roots (Sec. 3.1). These near-field scattered waves propagate as spherically diverging waves at large distances. To find the far-field waves, the vector Kirchhoff integral relation will be employed (Sec. 3.2). Sec. 3.3 checks up on the validity of the hybrid approach followed. A discussion about the influence of the drop non-sphericity on the different rainbow interference patterns concludes the chapter.

3.1 Rainbow at surface of ellipsoidal droplet: a geometrical approach

3.1.1 Ray tracing in an ellipsoid

In order to trace the path of a light ray in an ellipsoidal particle with a uniform and real refractive index, mathematical descriptions for the ellipsoid and the light ray have to be found. Subsequently, a physical model for the interaction of a ray with an interface completes the set of tools that is required.

The scattering ellipsoidal obstacle can be defined in Cartesian and spherical

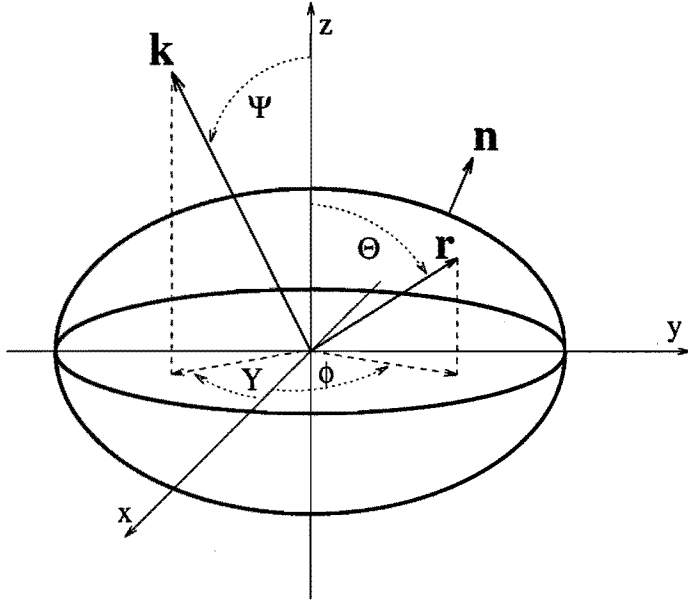


Figure 3.1: Definition of the coordinate systems for the ellipsoid and a wave vector.

polar coordinates (Fig. 3.1):

$$\frac{1}{4} = \left(\frac{x}{A}\right)^2 + \left(\frac{y}{B}\right)^2 + \left(\frac{z}{C}\right)^2, \quad (3.1)$$

$$\mathbf{r}(\Theta, \phi) = \frac{A}{2} \sin \Theta \cos \phi \mathbf{e}_x + \frac{B}{2} \sin \Theta \sin \phi \mathbf{e}_y + \frac{C}{2} \cos \Theta \mathbf{e}_z. \quad (3.2)$$

A , B and C are the 3 diameters of the ellipsoid. The unit vector representing the normal to the surface is essential for 3D ray-tracing. It points outward and is calculated following Kreyszig[34]:

$$\begin{aligned} \mathbf{n} &= \left(\frac{\partial \mathbf{r}}{\partial \Theta} \times \frac{\partial \mathbf{r}}{\partial \phi} \right) / \left\| \frac{\partial \mathbf{r}}{\partial \Theta} \times \frac{\partial \mathbf{r}}{\partial \phi} \right\| \\ &= \frac{1}{4} \left(BC \sin^2 \Theta \cos \phi \mathbf{e}_x + AC \sin^2 \Theta \sin \phi \mathbf{e}_y + AB \sin \Theta \cos \Theta \mathbf{e}_z \right) \\ &\quad / \left\| \frac{\partial \mathbf{r}}{\partial \Theta} \times \frac{\partial \mathbf{r}}{\partial \phi} \right\|. \end{aligned} \quad (3.3)$$

The geometrical ray is represented parametrically by the vector \mathbf{x} :

$$\mathbf{x} = \mathbf{r} + \mathbf{k}q. \quad (3.4)$$

q is the parameter indicating the position on the path of a ray. \mathbf{r} is the position vector given by Eq. 3.2. \mathbf{k} denotes the wave vector; its components contain the

“direction cosines” of the light ray:

$$\mathbf{k}(\Psi, Y) = \frac{2\pi}{\lambda} m (\sin \Psi \cos Y \mathbf{e}_x + \sin \Psi \sin Y \mathbf{e}_y + \cos \Psi \mathbf{e}_z). \quad (3.5)$$

The angles Ψ and Y are defined in Fig. 3.1. If one intersection point of a ray with the ellipsoid is known, then the other one can be found by solving Eqs. 3.1, 3.2, 3.4 and 3.5 for parameter q .

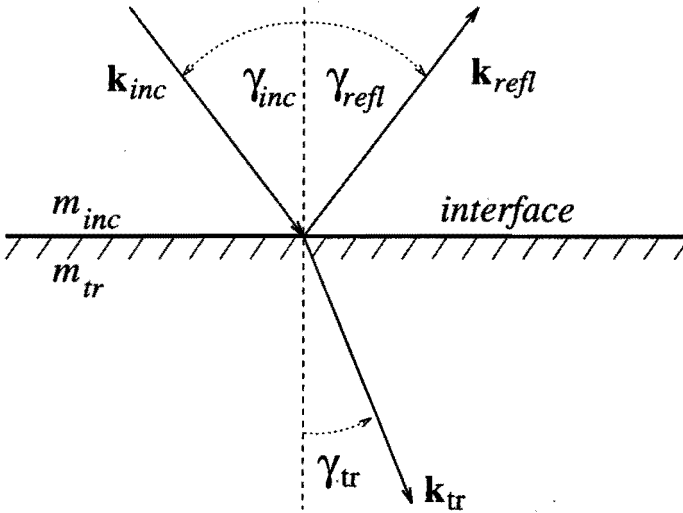


Figure 3.2: Interaction of a geometrical ray with an interface. The plane of incidence is formed by the three light rays represented by the wave vectors \mathbf{k}_{inc} , \mathbf{k}_{refl} and \mathbf{k}_{tr} .

A ray which is incident on an interface is partially reflected and transmitted, as sketched in Fig. 3.2. The transmitted ray is refracted according to Snell’s law:

$$m_{inc} \sin \gamma_{inc} = m_{tr} \sin \gamma_{tr}. \quad (3.6)$$

m_{inc} and m_{tr} designate the constant, real refractive indices of the media in which the incident (subscript *inc*) and transmitted ray (subscript *tr*) propagate. Similarly, γ_{inc} is the incident and γ_{tr} the transmitted angle with respect to the normal. In a three-dimensional environment the incident angle γ_{inc} can be represented as

$$\gamma_{inc} = \begin{cases} \arccos \frac{(\mathbf{k}_{inc} \cdot \mathbf{n})}{k_{inc}} & \text{if } (\mathbf{k}_{inc} \cdot \mathbf{n}) > 0, \\ \pi - \arccos \frac{(\mathbf{k}_{inc} \cdot \mathbf{n})}{k_{inc}} & \text{if } (\mathbf{k}_{inc} \cdot \mathbf{n}) < 0. \end{cases} \quad (3.7)$$

Consequently, $0 < \gamma_{inc} < 90^\circ$. k_{inc} is the amplitude of \mathbf{k}_{inc} . Eqs. 3.6 and 3.7 lead to the transmitted 3D wave vector:

$$\mathbf{k}_{tr} = \begin{cases} \frac{2\pi m_{tr}}{\lambda} \left(\frac{\mathbf{n} \times \mathbf{k}_{inc} \times \mathbf{n}}{\|\mathbf{n} \times \mathbf{k}_{inc} \times \mathbf{n}\|} \sin \gamma_{tr} + \mathbf{n} \cos \gamma_{tr} \right) & \text{if } m_{inc} > m_{tr}, \\ \frac{2\pi m_{tr}}{\lambda} \left(\frac{\mathbf{n} \times \mathbf{k}_{inc} \times \mathbf{n}}{\|\mathbf{n} \times \mathbf{k}_{inc} \times \mathbf{n}\|} \sin \gamma_{tr} - \mathbf{n} \cos \gamma_{tr} \right) & \text{if } m_{inc} < m_{tr}. \end{cases} \quad (3.8)$$

The conditions are valid when the refractive index inside the particle is higher than outside. The law of reflection states that the angle of reflection γ_{refl} equals the incident angle γ_{inc} . Therefore, the reflected wave vector holds

$$\mathbf{k}_{refl} = \begin{cases} \frac{2\pi m_{inc}}{\lambda} \left(\frac{\mathbf{n} \times \mathbf{k}_{inc} \times \mathbf{n}}{\|\mathbf{n} \times \mathbf{k}_{inc} \times \mathbf{n}\|} \sin \gamma_{refl} + \mathbf{n} \cos \gamma_{refl} \right) & \text{if } m_{inc} < m_{tr}, \\ \frac{2\pi m_{inc}}{\lambda} \left(\frac{\mathbf{n} \times \mathbf{k}_{inc} \times \mathbf{n}}{\|\mathbf{n} \times \mathbf{k}_{inc} \times \mathbf{n}\|} \sin \gamma_{refl} - \mathbf{n} \cos \gamma_{refl} \right) & \text{if } m_{inc} > m_{tr}. \end{cases} \quad (3.9)$$

It is evident that the transmitted and reflected rays remain in the plane of incidence formed by the incident wave vector and the normal to the surface at the intersection point.

All the relationships mentioned in this subsection form a complete set of equations that is necessary for describing the tracing of a light ray in an ellipsoid.

3.1.2 Polarization

A polarization vector \mathbf{p} can be assigned to a geometrical ray. The interaction of this vector with an interface is described by the laws of reflection and refraction (Subsec. 3.1.1) and by the Fresnel coefficients. These coefficients account for the diminishing of the light intensity of a ray and depend on the angles γ_{inc} , γ_{tr} and the angle that the polarization vector makes with the plane of incidence. For the component of \mathbf{p} perpendicular to this plane, the next amplitude-reflection coefficient has to be applied (see Ref. [30]):

$$r_{\perp} = \frac{-\sin(\gamma_{inc} - \gamma_{tr})}{\sin(\gamma_{inc} + \gamma_{tr})}, \quad (3.10)$$

where the media were assumed to be dielectric. For the parallel component the Fresnel coefficient reads

$$r_{\parallel} = \frac{\tan(\gamma_{inc} - \gamma_{tr})}{\tan(\gamma_{inc} + \gamma_{tr})}. \quad (3.11)$$

The amplitude-transmission coefficients are

$$t_{\perp} = \frac{2 \sin \gamma_{tr} \cos \gamma_{inc}}{\sin(\gamma_{inc} + \gamma_{tr})}, \quad (3.12)$$

$$t_{\parallel} = \frac{2 \sin \gamma_{tr} \cos \gamma_{inc}}{\sin(\gamma_{inc} + \gamma_{tr}) \cos(\gamma_{inc} - \gamma_{tr})}. \quad (3.13)$$

At normal incidence the above relationships reduce to

$$r_{\parallel}|_{\gamma_{inc}=0} = -r_{\perp}|_{\gamma_{inc}=0} = \frac{m_{tr} - m_{inc}}{m_{tr} + m_{inc}}, \quad (3.14)$$

$$t_{\parallel}|_{\gamma_{inc}=0} = t_{\perp}|_{\gamma_{inc}=0} = \frac{2m_{inc}}{m_{tr} + m_{inc}}. \quad (3.15)$$

To apply the Fresnel coefficients, one has to resolve the polarization vector into a perpendicular and parallel component with respect to the plane of incidence, i.e. $\mathbf{p}_{inc\perp}$ and $\mathbf{p}_{inc\parallel}$ respectively:

$$\mathbf{p}_{inc\perp} = \frac{(\mathbf{p}_{inc} \cdot (\mathbf{k}_{inc} \times \mathbf{n}))}{\|\mathbf{k}_{inc} \times \mathbf{n}\|^2} (\mathbf{k}_{inc} \times \mathbf{n}), \tag{3.16}$$

$$\mathbf{p}_{inc\parallel} = \frac{(\mathbf{p}_{inc} \cdot (\mathbf{k}_{inc} \times \mathbf{p}_{inc\perp}))}{\|\mathbf{k}_{inc} \times \mathbf{p}_{inc\perp}\|^2} (\mathbf{k}_{inc} \times \mathbf{p}_{inc\perp}). \tag{3.17}$$

From this, the 3D-transmitted vector components can be constructed:

$$\mathbf{p}_{tr\perp} = \mathbf{p}_{inc\perp} t_{\perp}, \tag{3.18}$$

$$\mathbf{p}_{tr\parallel} = \frac{((\mathbf{p}_{inc\perp} \times \mathbf{k}_{inc}) \cdot \mathbf{p}_{inc\parallel})}{\|\mathbf{p}_{inc\perp} \times \mathbf{k}_{inc}\| \|\mathbf{p}_{inc\perp} \times \mathbf{k}_{tr}\|} (\mathbf{p}_{inc\perp} \times \mathbf{k}_{tr}) t_{\parallel}. \tag{3.19}$$

The components of the polarization vector change by internal or external reflection following

$$\mathbf{p}_{refl\perp} = \mathbf{p}_{inc\perp} r_{\perp}, \tag{3.20}$$

$$\mathbf{p}_{refl\parallel} = \frac{((\mathbf{p}_{inc\perp} \times \mathbf{k}_{inc}) \cdot \mathbf{p}_{inc\parallel})}{\|\mathbf{p}_{inc\perp} \times \mathbf{k}_{inc}\| \|\mathbf{p}_{inc\perp} \times \mathbf{k}_{refl}\|} (\mathbf{p}_{inc\perp} \times \mathbf{k}_{refl}) r_{\parallel}. \tag{3.21}$$

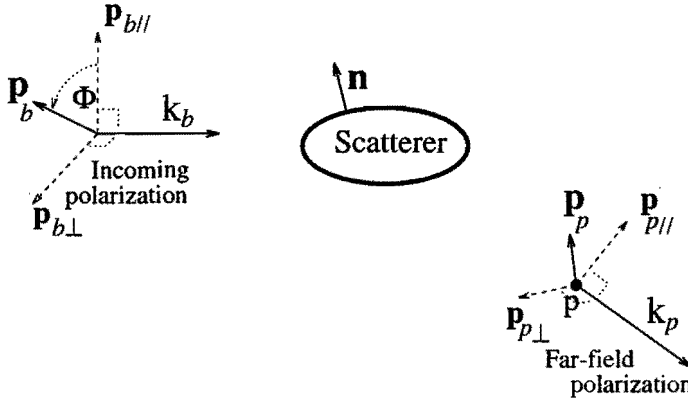


Figure 3.3: Definition of incoming and scattered polarization vector. The scattering plane is taken through the direction of the incident and scattered wave vectors. Φ is the angle between \mathbf{p}_b and the scattering plane.

The initial polarization vector to substitute for \mathbf{p}_{inc} in Eqs. 3.16 and 3.17 is \mathbf{p}_b , which is assigned to the incoming beam that illuminates the particle (Fig. 3.3). This vector makes an angle Φ with the scattering plane which is formed by the

wave vector of the incoming beam, \mathbf{k}_b , and the scattered wave vector \mathbf{k}_p in an observation point P at infinity:

$$\mathbf{p}_b = \frac{(\mathbf{k}_p \times \mathbf{k}_b)}{\|\mathbf{k}_p \times \mathbf{k}_b\|} \sin \Phi + \frac{(\mathbf{k}_p \times \mathbf{k}_b) \times \mathbf{k}_b}{\|(\mathbf{k}_p \times \mathbf{k}_b) \times \mathbf{k}_b\|} \cos \Phi. \quad (3.22)$$

It is important to notice that the components of \mathbf{p}_b parallel and perpendicular to the scattering plane are most likely to differ from the components with respect to the incident plane at the first interaction of the incoming ray with the ellipsoid.

3.1.3 Phase

Consider a ray in a planar wave front incident on an ellipsoidal droplet. When it leaves the droplet, the phase has changed. This can be due to three effects as described by Van de Hulst[81] and Hovenac[31] for example:

1. Either internal or external reflection can be attributed to a phase change of π . This is accounted for by the Fresnel reflection coefficients, treated in Subsec. 3.1.2.
2. Another effect is the length of the optical path followed. At the surface where the rays emerge from the droplet, the phase has shifted

$$\sigma = m_o (\mathbf{k}_b \cdot \mathbf{r}(\Theta_1, \phi_1)) + \frac{2\pi m_i}{\lambda} \sum_{i=1}^{N-1} \|\mathbf{r}(\Theta_{i+1}, \phi_{i+1}) - \mathbf{r}(\Theta_i, \phi_i)\| \quad (3.23)$$

with respect to the incident wave front. N is the number of intersections between the light ray and the ellipsoid; $\mathbf{r}(\Theta_i, \phi_i)$ points to the position at which the i^{th} intersection occurs (Eq. 3.2). m_i and m_o are the refractive indices inside and outside the particle, respectively.

3. The phase advances $\pi/2$ whenever two adjacent rays cross each other, i.e. focus. Therefore, while tracing rays one has to count the number of focal points denoted by integer l . In the case of external reflection ($N = 1$), there is no focus, whereas for $N = 2$ there is one focus before the rays exit the droplet. The first-order rainbow rays ($N = 3$) encounter two or three foci. The reason is that after one internal reflection there is a part of the wave front that folds before reaching the last interface. For this folded part the phase has advanced $3\pi/2$.

3.1.4 Gain factor

The gain factor accounts for the influence that the shape of the scatterer has on the angular dispersion of the light. *Gain* is defined as the ratio between the scattered energy flux near the droplet surface, I_s , and the incident energy flux I_b (Fig. 3.4):

$$\text{Gain} = \frac{I_s}{I_b}. \quad (3.24)$$

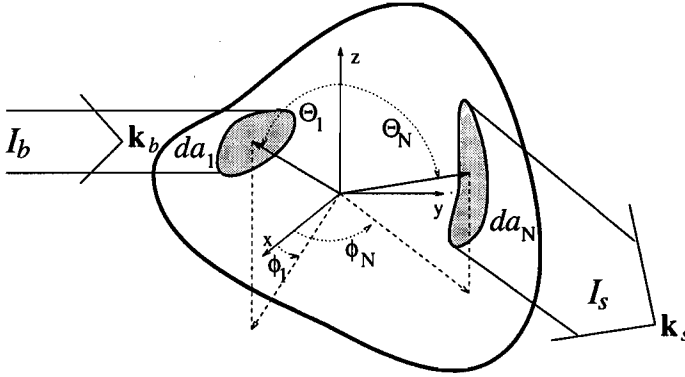


Figure 3.4: The influence of the shape of the scatterer on the angular light dispersion. I_b is the incident irradiance; k_b and k_s are the wave vectors for the incident and outgoing light pencils, respectively. $\mathbf{r}(\Theta_1, \phi_1)$ indicates the position of infinitesimal area da_1 . $\mathbf{r}(\Theta_N, \phi_N)$ refers to the position of the outgoing light pencil after having experienced N interactions with the surface of the scatterer.

To find an expression for *Gain*, the power P_b has to be defined as the radiant energy of a light pencil arriving on an infinitesimal surface element da_1 of the ellipsoid:

$$P_b = I_b da_1(\Theta_1, \phi_1) |(\mathbf{k}_b \cdot \mathbf{n}(\Theta_1, \phi_1))|/k_b. \tag{3.25}$$

This power is transmitted to surface da_N after N interactions of the light pencil with the interface of the obstacle. The scattered irradiance near da_N therefore holds

$$I_s = P_b/(da_N(\Theta_N, \phi_N) |(\mathbf{k}_s \cdot \mathbf{n}(\Theta_N, \phi_N))|/k_b). \tag{3.26}$$

Substitution of above expressions in Eq. 3.24 yields

$$Gain = \frac{da_1}{da_N} \frac{|(\mathbf{k}_b \cdot \mathbf{n}(\Theta_1, \phi_1))|}{|(\mathbf{k}_s \cdot \mathbf{n}(\Theta_N, \phi_N))|}. \tag{3.27}$$

For an isotropic spherical scatterer, *Gain* equals 1/4.

The area da_1 , characterized by $d\Theta_1$ and $d\phi_1$, and the area da_N , related to $d\Theta_N$ and $d\phi_N$, are defined by

$$da_1(\Theta_1, \phi_1) = \left\| \frac{\partial \mathbf{r}(\Theta_1, \phi_1)}{\partial \Theta} \times \frac{\partial \mathbf{r}(\Theta_1, \phi_1)}{\partial \phi} \right\| d\Theta_1 d\phi_1, \tag{3.28}$$

$$da_N(\Theta_N, \phi_N) = \left\| \frac{\partial \mathbf{r}(\Theta_N, \phi_N)}{\partial \Theta} \times \frac{\partial \mathbf{r}(\Theta_N, \phi_N)}{\partial \phi} \right\| d\Theta_N d\phi_N = \left\| \frac{\partial \mathbf{r}(\Theta_N, \phi_N)}{\partial \Theta} \times \frac{\partial \mathbf{r}(\Theta_N, \phi_N)}{\partial \phi} \right\| |\mathcal{J}| d\Theta_1 d\phi_1. \tag{3.29}$$

For an ellipsoid, geometrical tools can be employed to find the relationship between $\mathbf{r}(\Theta_1, \phi_1)$ and the vector pointing to the position where the light pencil leaves the particle after having experienced N interactions with the surface, i.e. $\mathbf{r}(\Theta_N, \phi_N)$. These tools are described in Subsec. 3.1.1 and help to calculate the Jacobian \mathcal{J} (see for example Kreyszig[35]):

$$\mathcal{J} = \frac{\partial(\Theta_N, \phi_N)}{\partial(\Theta_1, \phi_1)} = \begin{vmatrix} \frac{\partial\Theta_N}{\partial\Theta_1} & \frac{\partial\Theta_N}{\partial\phi_1} \\ \frac{\partial\phi_N}{\partial\Theta_1} & \frac{\partial\phi_N}{\partial\phi_1} \end{vmatrix}. \quad (3.30)$$

Upon combining the above formulas, the gain factor becomes

$$Gain = \frac{1}{|\mathcal{J}|} \frac{\|\partial\mathbf{r}(\Theta_1, \phi_1)/\partial\Theta \times \partial\mathbf{r}(\Theta_1, \phi_1)/\partial\phi\|}{\|\partial\mathbf{r}(\Theta_N, \phi_N)/\partial\Theta \times \partial\mathbf{r}(\Theta_N, \phi_N)/\partial\phi\|} \frac{|(\mathbf{k}_b \cdot \mathbf{n}(\Theta_1, \phi_1))|}{|(\mathbf{k}_s \cdot \mathbf{n}(\Theta_N, \phi_N))|}. \quad (3.31)$$

3.1.5 Scattered field at the droplet surface

The scattered electric field at the surface of the scattering obstacle can be obtained with the help of ray optics. Therefore, the path of the incoming ray through the droplet, the state of the scattered polarization vector \mathbf{p}_s , the phase changes and the gain factor have to be computed. This has all been covered before in the present section. From this, the electric field \mathbf{E}_s at the surface can be constructed:

$$\mathbf{E}_s = E_b \mathbf{p}_s \sqrt{Gain} e^{-i(\omega t - \sigma - l\pi/2)}. \quad (3.32)$$

ω is the angular frequency in vacuum. E_b is the amplitude of the incoming wave. σ represents the phase shift due to the length of the optical path followed. l refers to the number of focal points passed by the light ray inside the ellipsoid. The Fresnel coefficients are taken into account by the polarization vector.

The magnetic-field vector function \mathbf{H}_s is calculated from the Maxwell relation 2.3 yielding

$$\mathbf{H}_s = \frac{(\mathbf{k}_s \times \mathbf{E}_s)}{\mu_0 \omega}. \quad (3.33)$$

Thus, the magnetic field \mathbf{H}_s is perpendicular to the electric field \mathbf{E}_s and to the wave vector \mathbf{k}_s . When the $(\mathbf{E}_s, \mathbf{H}_s)$ -field results from once-internally reflected rays then it propagates away from the scatterer forming the Airy rainbow pattern in the far field.

3.2 Rainbow in the far field: a hybrid approach

3.2.1 The vector Kirchhoff integral relation

Consider the situation sketched in Fig. 3.5. A light wave, represented by vector \mathbf{k}_b , impinges on a transparent ellipsoid. By means of the geometrical approach of the previous section, an expression for the scattered field $(\mathbf{E}_s, \mathbf{H}_s)$ close to the particle on surface S_1 can be computed. Far away from the obstacle, the scattered field propagates as spherically diverging waves having wave vector \mathbf{k}_p in the observation point P. The aim is to express the influence of the field $(\mathbf{E}_s, \mathbf{H}_s)$, represented by \mathbf{k}_s , on the observation point P in volume \mathcal{V} bounded by surfaces S_1 and S_2 . The electromagnetic approach followed results in the vector Kirchhoff Integral relation.

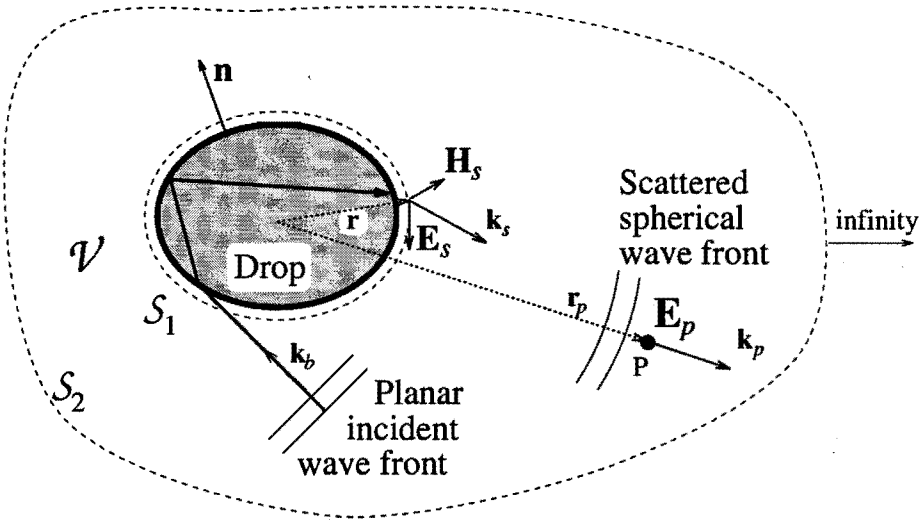


Figure 3.5: The electric field in point P, \mathbf{E}_p , can be expressed as a function of the scattered electromagnetic field, $(\mathbf{E}_s, \mathbf{H}_s)$, on surface S_1 enclosing the scatterer.

Let \mathbf{r} be the radial vector. Each rectangular component of the electric field $\mathbf{E}(\mathbf{r})$, satisfying Maxwell equations 2.1 to 2.4, is a solution of the scalar Helmholtz wave equation (Sec. 2.1):

$$\Delta \mathbf{E}(\mathbf{r}) + k^2 \mathbf{E}(\mathbf{r}) = 0. \tag{3.34}$$

Let \mathbf{r}_p be the position vector for the observation point P. In order to express $\mathbf{E}_p(\mathbf{r}_p)$ in the boundary conditions at surface S_1 , first the Green function $G(\mathbf{r}, \mathbf{r}_p)$ has to be introduced. This potential obeys

$$\Delta G(\mathbf{r}_p, \mathbf{r}) + k_p^2 G(\mathbf{r}_p, \mathbf{r}) = -\delta(\mathbf{r} - \mathbf{r}_p). \tag{3.35}$$

$\delta(\mathbf{r} - \mathbf{r}_p)$ denotes Dirac's delta function which makes $G(\mathbf{r}, \mathbf{r}_p)$ to be the time-harmonic scalar field resulting from a point source at $\mathbf{r} = \mathbf{r}_p$. The next step is to apply Green's second identity on the Green function and each rectangular component of $\mathbf{E}(\mathbf{r})$:

$$\int_{\mathcal{V}} [G(\mathbf{r}, \mathbf{r}_p) \Delta \mathbf{E}(\mathbf{r}) - \mathbf{E}(\mathbf{r}) \Delta G(\mathbf{r}, \mathbf{r}_p)] dx^3 = \oint_{\mathcal{S}} [G(\mathbf{r}, \mathbf{r}_p) (\mathbf{n} \cdot \nabla \mathbf{E}(\mathbf{r})) - \mathbf{E}(\mathbf{r}) (\mathbf{n} \cdot \nabla G(\mathbf{r}, \mathbf{r}_p))] da. \quad (3.36)$$

Combining this identity with the wave equations 3.34 and 3.35 leads to an integral expression for \mathbf{E}_p (where the position vectors have been left out):

$$\mathbf{E}_p = \oint_{\mathcal{S}} [\mathbf{E}_s (\mathbf{n} \cdot \nabla G) - G (\mathbf{n} \cdot \nabla \mathbf{E}_s)] da. \quad (3.37)$$

Notice that \mathbf{E} is put to \mathbf{E}_s on the surfaces bounding \mathcal{V} . This expression can be modified so that only the electric field \mathbf{E}_s is needed and not its gradient $\nabla \mathbf{E}_s$. Therefore one has to employ the divergence theorem, several vector formulas and vector calculus theorems. The exact derivation is given by Jackson[33] and leads to

$$\mathbf{E}_p = \oint_{\mathcal{S}} [(\mathbf{n} \cdot \mathbf{E}_s) \nabla G + (\mathbf{n} \times \mathbf{E}_s) \times \nabla G + iG(\mathbf{n} \times (\mathbf{k}_s \times \mathbf{E}_s))] da. \quad (3.38)$$

This is the vector Kirchhoff integral relation for \mathbf{E}_p in terms of the field on the boundary surfaces \mathcal{S}_1 and \mathcal{S}_2 . One has to proceed by solving wave Eq. 3.35 in order to obtain the Green function G . The scattering problem implies the free field solution:

$$G = \frac{e^{i(\mathbf{k}_p \cdot (\mathbf{r}_p - \mathbf{r}))}}{4\pi \|\mathbf{r}_p - \mathbf{r}\|}. \quad (3.39)$$

Based on this function one can show that the integral over \mathcal{S}_2 vanishes if the latter is a surface at infinity (see again Jackson[33]). As a result, the scattering amplitude is written as an integral of the scattered fields over surface \mathcal{S}_1 only, as was aimed for. The integral is simplified considerably when the observation point P is far from the obstacle. Then, the Green function takes its asymptotic form

$$G = \frac{1}{4\pi r_p} e^{ik_p r_p} e^{-i(\mathbf{k}_p \cdot \mathbf{r})}, \quad (3.40)$$

where r_p is the distance between the origin of the scatterer and point P. This expression for the Green function can be implemented into integral relation 3.38. At this stage, one can ask for the amplitude of the scattered radiation with wave vector \mathbf{k}_p and polarization vector \mathbf{p}_p :

$$(\mathbf{p}_p \cdot \mathbf{E}_p) = \frac{ie^{ik_p r_p}}{4\pi r_p} \oint_{\mathcal{S}_1} e^{-i(\mathbf{k}_p \cdot \mathbf{r})} [(\mathbf{n} \cdot \mathbf{E}_s)(\mathbf{k}_s \cdot \mathbf{p}_p) - (\mathbf{n} \cdot \mathbf{k}_s)(\mathbf{E}_s \cdot \mathbf{p}_p) - (\mathbf{n} \cdot \mathbf{k}_p)(\mathbf{E}_s \cdot \mathbf{p}_p) + (\mathbf{E}_s \cdot \mathbf{k}_p)(\mathbf{n} \cdot \mathbf{p}_p)] da. \quad (3.41)$$

Here the vector formula $\mathbf{a} \times (\mathbf{b} \times \mathbf{c}) = (\mathbf{a} \cdot \mathbf{c})\mathbf{b} - (\mathbf{a} \cdot \mathbf{b})\mathbf{c}$ was used. Eq. 3.41 is a scalar form of the vectorial equivalent of the Kirchhoff integral. The expression for the electric field \mathbf{E}_s is given by the geometrical approach presented in the previous section. Consequently, substitution of Eqs. 3.31 and 3.32 in Eq. 3.41 yields

$$(\mathbf{p}_p \cdot \mathbf{E}_p) = \frac{iE_b e^{i(k_p r_p - \omega t)}}{4\pi r_p} \int_0^{180^\circ} \int_{-180^\circ}^{180^\circ} g e^{i(k_p f + l\frac{\pi}{2})} d\Theta_1 d\phi_1, \quad (3.42)$$

with

$$\begin{aligned} f &= -((\mathbf{k}_p \cdot \mathbf{r}) - \sigma) / k_p, \\ g &= [(\mathbf{n} \cdot \mathbf{p}_s)(\mathbf{k}_s \cdot \mathbf{p}_p) - (\mathbf{n} \cdot \mathbf{k}_s)(\mathbf{p}_s \cdot \mathbf{p}_p) - (\mathbf{n} \cdot \mathbf{k}_p)(\mathbf{p}_s \cdot \mathbf{p}_p) + (\mathbf{p}_s \cdot \mathbf{k}_p)(\mathbf{n} \cdot \mathbf{p}_p)] \\ &\quad \|\partial \mathbf{r}(\Theta_1, \phi_1) / \partial \Theta \times \partial \mathbf{r}(\Theta_1, \phi_1) / \partial \phi\| \|\partial \mathbf{r}(\Theta_N, \phi_N) / \partial \Theta \times \partial \mathbf{r}(\Theta_N, \phi_N) / \partial \phi\| \\ &\quad |\mathcal{J}| \frac{|(\mathbf{k}_b \cdot \mathbf{n}(\Theta_1, \phi_1))|}{|(\mathbf{k}_s \cdot \mathbf{n}(\Theta_N, \phi_N))|}]^{1/2}. \end{aligned}$$

g includes the Jacobian \mathcal{J} that is necessary for the gain factor and for mapping from the coordinates of the scattered wave \mathbf{E}_s (e.g. Θ_3 and ϕ_3 for the primary rainbow) to the corresponding coordinates at which the incident wave impinges on the ellipsoid, i.e. Θ_1 and ϕ_1 (see Fig. 3.4). For this, the expressions in Sec. 3.1.4 and ray tracing tools were employed.

Eq. 3.42 is a simple diffraction-like integral, the basis of most of the work on diffraction (see e.g. Refs. [8, 17, 38]). It is the starting point for the following subsection.

3.2.2 Solving the Kirchhoff integral for the primary rainbow

Method of stationary phase

A solution for the Kirchhoff integral, Eq. 3.42, will be looked for. The integral is of the form

$$K(k_p) = \int_0^{180^\circ} \int_{-180^\circ}^{180^\circ} g(\Theta_1, \phi_1) e^{i(k_p f(\Theta_1, \phi_1) + l\frac{\pi}{2})} d\Theta_1 d\phi_1, \quad (3.43)$$

where f is the phase function and g the amplitude function. The phase in radian is given by $k_p f$. Eq. 3.43 represents a two-dimensional generalized Fourier integral. Before solving it, the one-dimensional equivalent will be treated; this is a line integral between $\eta = 0$ and $\eta = \infty$:

$$\Lambda(k_p) = \int_0^\infty g(\eta) e^{ik_p f(\eta)} d\eta. \quad (3.44)$$

For $k_p \rightarrow \infty$, $e^{ik_p f(\eta)}$ oscillates very rapidly. Then, $\Lambda(k_p)$ goes to zero provided that

- $g(\eta)$ does not change rapidly, that is to say $|g'(\eta)/g(\eta)| \ll |k_p f'(\eta)|$ and

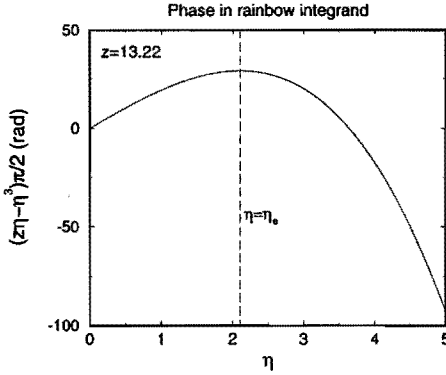


Figure 3.6: The phase in the rainbow integrand (Eq. 3.45) with an extremum at $\eta = \eta_e$.

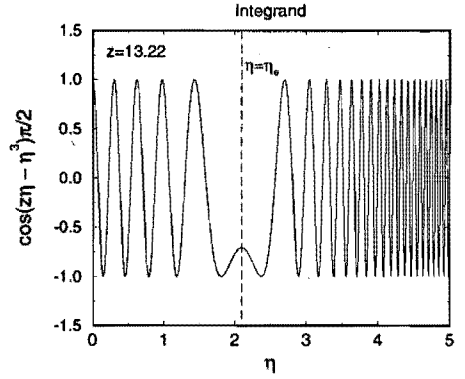


Figure 3.7: The integrand of the rainbow integral (Eq. 3.45) versus its integral variable η . At $\eta = \eta_e$ the integrand reveals a stationary point which is clearly influencing the integrand's periodic oscillation.

- $f(\eta)$ does not have any extremum nor singularity.

This makes the *Riemann-Lebesgue Lemma* (see Wilcox[88]).

If the phase function $f(\eta)$ has an extremum at $\eta = \eta_e$, then this point is called a stationary point. A stationary point plays a crucial role in the integral's asymptotic expansion. This is demonstrated by e.g. the integrand of the Airy or rainbow integral[82]:

$$\Omega_{rainbow}(z) = \int_0^{\infty} \cos \frac{1}{2} \pi (z\eta - \eta^3) d\eta. \quad (3.45)$$

Here $k_p f(\eta) = \frac{1}{2} \pi (z\eta - \eta^3)$. For $z = 13.22$, this function has one stationary point in the range of integration, namely at $\eta = \eta_e = \sqrt{13.22/3} = 2.10$. It is clear from Figs. 3.7 that this point affects the rapid period of oscillation of the integrand. This knowledge is used to generate the first term in the asymptotic expansion of Eq. 3.44. Therefore, by employing the *Riemann-Lebesgue Lemma*, $g(\eta)$ is set to $g(\eta_e)$ and $f(\eta)$ is expanded about $\eta = \eta_e$:

$$\Lambda(k_p) = 2g(\eta_e) e^{ik_p J(\eta_e)} \int_0^{\infty} e^{ik_p J''(\eta_e) (\eta - \eta_e)^2 / 2} d\eta. \quad (3.46)$$

Subsequently, from the fact that the Gamma function $\Gamma(\frac{1}{2})$ yields[1]

$$\Gamma(\frac{1}{2}) = \int_0^{\infty} e^{-\xi^2} d\xi = \sqrt{\pi}, \quad (3.47)$$

Eq. 3.46 becomes

$$\Lambda(k_p) = g(\eta_e) e^{i(k_p f(\eta_e) - \frac{\pi}{4})} \sqrt{\frac{2\pi}{k_p |f''(\eta_e)|}}. \quad (3.48)$$

The procedure followed refers to the method of stationary phase. If in the path of integration more extrema are encountered, one simply adds the contribution for each maximum as given by Eq. 3.48. However, this is only valid when the maxima are well separated.

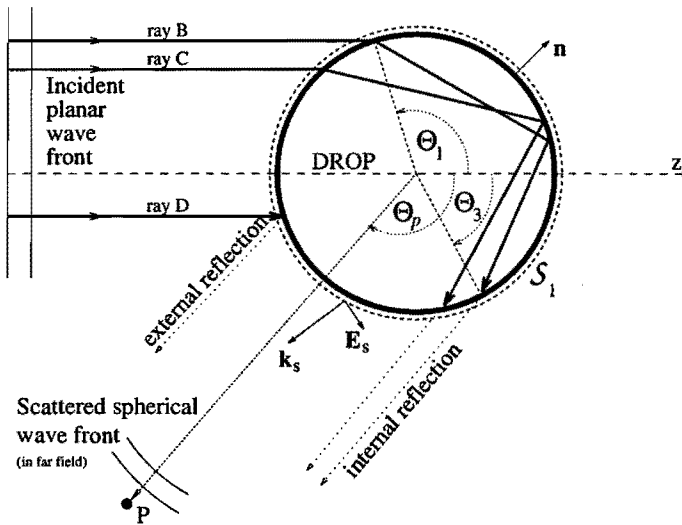


Figure 3.8: The scattering problem considered for the 2D-Kirchhoff integral solved for the primary rainbow arising from a sphere. Internal and external reflections constitute the electric field \mathbf{E}_s near the surface (Eq. 3.32). Definitions of angles Θ_1 and Θ_3 follow Fig. 3.4. The incoming wave is parallel to the z -axis so that Θ_p equals the scattering angle.

Airy fringes

Now, the Kirchhoff integral $K(k_p)$ will be solved for the primary rainbow arising from a spherical droplet with a diameter of $100 \mu\text{m}$, i.e. $A = B = C = 100 \mu\text{m}$. Ray optics states that the most important contribution comes from once-internally reflected rays as sketched in Fig. 3.8. The external reflection interferes with these rays but, at this stage, this will be neglected. For the scattering problem considered, the refractive indices inside and outside the sphere are $m_o = 1$ and $m_i = 1.33$, respectively. The incident beam of rays is parallel to the z -axis and linearly polarized in the x -direction. The coordinates for the observation point

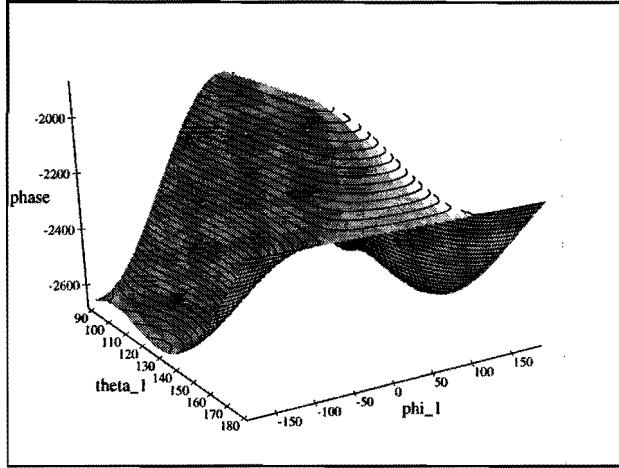


Figure 3.9: The phase $-k_p f^{int}(\Theta_1, \phi_1)$ as used for the Kirchoff integral (Eq. 3.43), calculated for a sphere of $100 \mu\text{m}$ in diameter and a real refractive index of $m_i = 1.33$. The observation point is placed where the rainbow is expected to be seen, i.e. $(\Theta_p, \phi_p) = (140^\circ, 180^\circ)$.

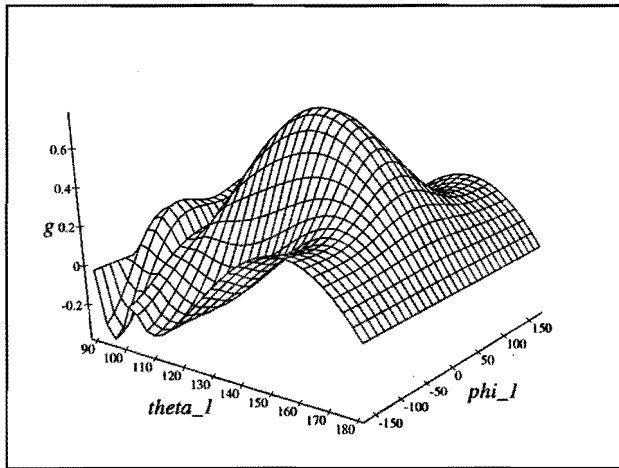


Figure 3.10: The function $g^{int}(\Theta_1, \phi_1)$ as defined in Eq. 3.42, applied to the Airy rainbow.

are $(\Theta_p, \phi_p) = (140^\circ, 180^\circ)$, which is in the primary rainbow region. It is an obvious choice to look for scattered-light linearly polarized in the x -direction, i.e. the polarization vector \mathbf{p}_p in the observation point is put to the unit vector in the x -direction (see Eq. 3.42).

For the scattering problem described, Figs. 3.9 and 3.10 depict the phase $-k_p f^{int}(\Theta_1, \phi_1)$ (superscript *int* pertains to internal reflection) and the amplitude function $g^{int}(\Theta_1, \phi_1)$ as a function of the integration variables Θ_1 and ϕ_1 . For this, the geometrical tools of Sec. 3.1 have been utilized. The plotted Θ_1 -interval ranges from 90° to 180° which covers the illuminated part of the sphere. A full-blown, 2D, numerical integration of the Kirchhoff integral over this domain appears highly unstable because the phase demonstrates steep edges that lead to numerous oscillations in the integrand. Therefore, it is appealing to look for the stationary points in the phase function and subsequently express the integral in terms of these points as was done for the 1D-integral of Eq. 3.44. Close study of Fig. 3.9 reveals stationary points at ¹

$$\begin{aligned} (\Theta_1^{\text{ray B}}, \phi_1^{\text{ray B}}) &= (110.4^\circ, 0^\circ), \\ (\Theta_1^{\text{ray C}}, \phi_1^{\text{ray C}}) &= (131.7^\circ, 0^\circ), \\ (\Theta_1^{\text{fold}}, \phi_1^{\text{fold}}) &= (103.1^\circ, 0^\circ). \end{aligned}$$

A stationary point in a phase function can be attributed to a geometrical ray (see Feynmann[17] and Lock and Andrews[38]). The first two stationary points correspond to internally-reflected rays B and C (see Fig. 3.8). The third one will not contribute to the integral because $g = 0$ at this point. Nevertheless, it plays an important role because it corresponds to the folding point of the internally-reflected wave front at the droplet surface, i.e. the extremum in the curve of Θ_3 versus Θ_1 (Fig. 3.11). The importance lies in the fact that between the edge and the folding ray, 3 foci have been passed whereas beyond the folding point, the wave front has only encountered 2 foci. In Subsec. 3.1.3 it was explained that this introduces a discontinuity of $\frac{\pi}{2}$ in the phase at the surface of the scatterer.

Unfortunately, a direct relationship between the integral and the stationary points in the phase function is not possible because the different extrema are not well isolated. They merge together when Θ_p approaches the geometric rainbow angle $\theta_{r,g}$ and even completely disappear for $\Theta_p < \theta_{r,g}$. Thus an alternative method of integration has to be found that is not affected by the merging and disappearance of stationary points. The approach followed here consists of choosing a path of integration which goes over the ridge of the phase function f^{int} from $(\Theta_1, \phi_1) = (90^\circ, 0^\circ)$ to $(\Theta_1, \phi_1) = (180^\circ, 0^\circ)$ (see Fig. 3.9). This path includes the stationary points that are related to the different geometrical rays. But each point on the ridge by itself already exhibits a maximum in f^{int} with respect to the direction perpendicular to the path of integration. Consequently, this extremum can be approximated by the method of stationary phase which was expressed in Eq. 3.48.

¹The stationary points in f^{int} for $\phi_1 = \pm 180^\circ$ do not contribute to the integral because function g^{int} causes the asymptotic expansions in the different extrema to cancel each other.

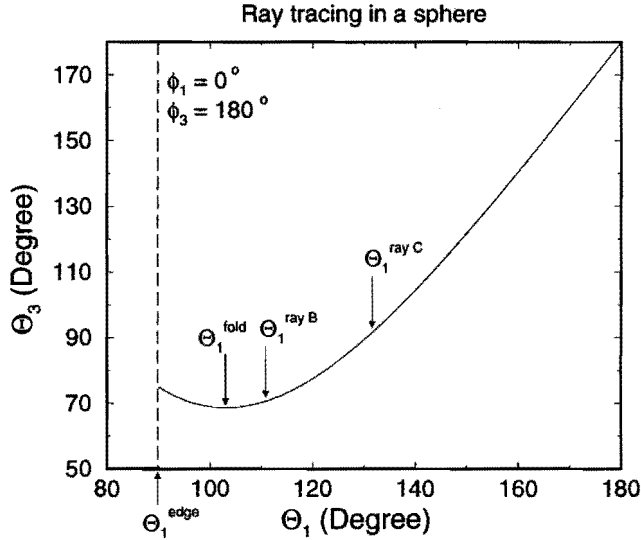


Figure 3.11: Θ_3 as a function of the angle Θ_1 for one internal reflection (see Fig. 3.8 for definition of the angles). The internally-reflected wave front, upon emerging from the spherical droplet, folds at $(\Theta_3^{\text{fold}}, \phi_3^{\text{fold}}) = (68.6^\circ, 180^\circ)$, corresponding to a light ray incident at $(\Theta_1^{\text{fold}}, \phi_1^{\text{fold}}) = (103.1^\circ, 0^\circ)$.

Therefore, one can reduce the surface integral $K^{\text{int}}(k_p)$ to a line integral:

$$K^{\text{int}}(k_p) = \int_{90^\circ}^{180^\circ} \int_{-180^\circ}^{180^\circ} g^{\text{int}}(\Theta_1, \phi_1) e^{i(k_p f^{\text{int}}(\Theta_1, \phi_1) + l\frac{\pi}{2})} d\Theta_1 d\phi_1 = \int_0^{90^\circ} g^{\text{int}}(\zeta^{\text{int}}) \sqrt{\frac{2\pi}{k_p |f_{\perp}^{\text{int}''}(\zeta^{\text{int}})|}} e^{i(k_p f^{\text{int}}(\zeta^{\text{int}}) - \frac{\pi}{4} + l\frac{\pi}{2})} d\zeta^{\text{int}}, \quad (3.49)$$

where ζ^{int} is the (positive) position parameter along the path of integration. $|f_{\perp}^{\text{int}''}(\zeta^{\text{int}})|$ is the second derivative with respect to the direction perpendicularly to this path. The integer l equals 2 or 3, according to the number of focal points passed by the internally-reflected light-rays (Subsec. 3.1.3).

The proposed integration method requires a robust algorithm for tracing the ridge of the phase function. Fig. 3.12 demonstrates the algorithm that is applied. It draws a straight line through the folding point $(\Theta_1^{\text{fold}}, \phi_1^{\text{fold}})$ and the edge point on the ridge of the phase function, $(\Theta_1^{\text{edge}}, \phi_1^{\text{edge}})$:

$$\Theta_1 = \Theta_1^{\text{edge}} \mp \zeta^{\text{int}} \cos(\kappa^{\text{int}}), \quad (3.50)$$

$$\phi_1 = \phi_1^{\text{edge}} \mp \zeta^{\text{int}} \sin(\kappa^{\text{int}}), \quad (3.51)$$

$$\kappa^{\text{int}} = \arctan \left[\frac{\phi_1^{\text{fold}} - \phi_1^{\text{edge}}}{\Theta_1^{\text{fold}} - \Theta_1^{\text{edge}}} \right]. \quad (3.52)$$

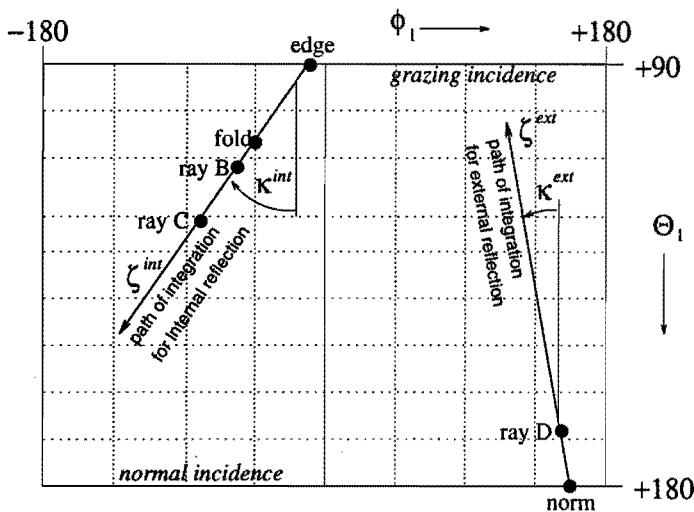


Figure 3.12: Paths of integration in the (Θ_1, ϕ_1) -plane. The path for internal reflection is determined by the ridge on the phase function and is represented by a straight line through the edge and folding point. The straight path of integration for external reflection is taken through the normal and stationary points. The latter is related to the geometrical ray D, as sketched in Fig. 3.8. For the scattering problem defined in that figure, $\kappa^{int} = \kappa^{ext} = 0$, the edge point “edge” lies on $\phi_1 = 0^\circ$ and the normal point “norm” on $\phi_1 = 180^\circ$.

The plus-sign applies for $\Theta_1^{fold} > \Theta_1^{dge}$ and the minus-sign for $\Theta_1^{fold} < \Theta_1^{dge}$. Minimizing the function $|\mathbf{n} \cdot \mathbf{k}_b| f^{int}$ leads to the edge point. The folding point is found by minimizing the function $k_p f^{int} - (\mathbf{r}(\Theta_3, \phi_3) \cdot \mathbf{k}_b)$. In the case of a spherical droplet, it is obvious that the straight line defined by $(\Theta_1^{dge}, \phi_1^{dge})$ and $(\Theta_1^{fold}, \phi_1^{fold})$ will also go through the stationary points $(\Theta_1^{ray B}, \phi_1^{ray B})$ and $(\Theta_1^{ray C}, \phi_1^{ray C})$, provided that the scattering plane contains one of the Cartesian axes. For an ellipsoid arbitrarily located in the incident light rays, the points do not necessarily lie on one line. However, the approximation of a straight line holds for certain as long as the 3D-scattering problem can be reduced to a 2D-problem. For now, this limits the applicability of the surface integral method to situations that correspond to geometrical rays that lie in one plane.

Fig. 3.13 shows the phase on the line of integration as a function of the position parameter ζ^{int} . Fig. 3.14 depicts the real and imaginary parts of the integrand of $K^{int}(k_p)$. Numerical integration between $\zeta^{int} = 0^\circ$ and $\zeta^{int} = 90^\circ$ would still cost days of CPU time on a DEC Alpha AXP 3000/400. This is mainly caused by the expensive computation of the amplitude function $g^{int}(\zeta^{int})$ for each value of ζ^{int} . Moreover, to obtain an entire angular rainbow pattern, $K^{int}(k_p)$ has to be evaluated for a whole range of different scattering angles Θ_p . It has therefore been decided to employ a least-squares fit of $g^{int}(\zeta^{int})$ with respect to ζ^{int} before

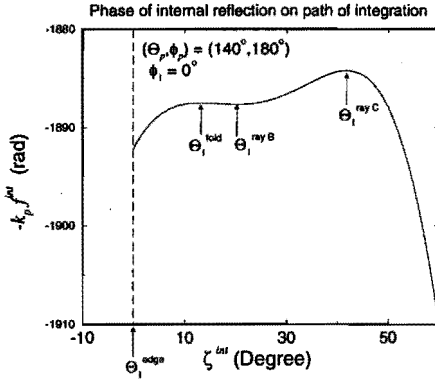


Figure 3.13: The function $-k_p f^{int}$ as a function of the integration variable ζ^{int} employed in the line integral of Eq. 3.49.

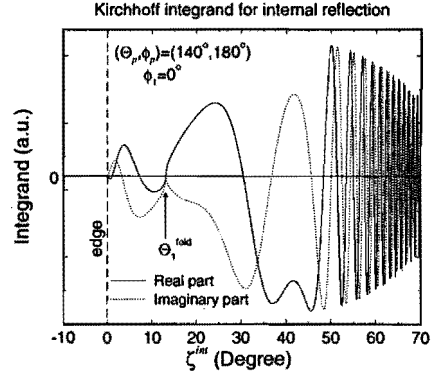


Figure 3.14: The real and imaginary part of the integrand of the Kirchhoff integral for internal reflection.

starting the numerical integration². It appears that this fit is almost identical for any Θ_p in the primary rainbow region. The CPU time is thus further reduced about 100 times when $g^{int}(\zeta^{int})$ is assumed to be independent of Θ_p . A similar fit is also constructed for phase function $f^{int}(\zeta^{int})$. This fit has to be recomputed for every Θ_p because the dependency of the phase function on Θ_p is an essential feature for the calculation of the Airy fringes. On the other hand, the second derivative $f_{\perp}^{int''}(\zeta^{int})$ with respect to the direction perpendicularly to the integration path is only evaluated at the folding point and then applied at every value of ζ^{int} .

Ripple structure

Before showing results, external reflection will be included. This is rather straightforward because of the hybrid character of the surface integral method. First, there is the Kirchhoff integral that results from the wave theory of light and expresses the far-field scattering amplitude in terms of the scattered field close to the droplet surface, i.e. \mathbf{E}_s . Secondly, ray optics is used to assign \mathbf{E}_s to geometrically-traced rays. The latter is employed to extend the Airy rainbow pattern with the ripple structure that results from interference between internal and external reflection. Therefore, one adds the scattered field that is assigned to external reflection, \mathbf{E}_s^{ext} , to the scattered field assigned to the internal reflection, \mathbf{E}_s^{int} :

$$\mathbf{E}_s = \mathbf{E}_s^{ext} + \mathbf{E}_s^{int}. \quad (3.53)$$

From substitution in Eq. 3.41 it follows that the Kirchhoff integral for the primary rainbow pattern is described as a linear combination of two Kirchhoff integrals,

²The numerical tools developed by the Numerical Algorithms Group[52] has been used to compute a least-squares polynomial approximation represented in Chebyshev-series form.

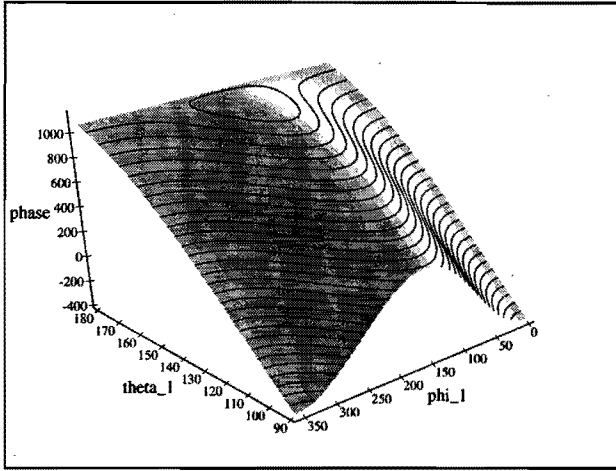


Figure 3.15: The phase $-k_p f^{ext}(\Theta_1, \phi_1)$ as used for the Kirchoff integral concerning external reflection. The scattering problem refers to Fig. 3.8. The sphere has a diameter of $100 \mu\text{m}$ and a real refractive index of $m_i = 1.33$. The observation point is placed where the primary rainbow is expected to be seen, i.e. $(\Theta_p, \phi_p) = (140^\circ, 180^\circ)$.

one for internal and the other for external reflection:

$$K(k_p) = K^{int}(k_p) + K^{ext}(k_p), \tag{3.54}$$

where $K^{int}(k_p)$ is given by Eq. 3.49. The Kirchoff integral for the external reflection can be expressed in a line integral over the ridge of the phase function for external reflection, as was done for $K^{int}(k_p)$:

$$K^{ext}(k_p) = \int_{0^\circ}^{90^\circ} g^{ext}(\zeta^{ext}) \sqrt{\frac{2\pi}{k_p |f_{ext}''(\zeta^{ext})|}} e^{i(k_p f^{ext}(\zeta^{ext}) - \frac{\pi}{4})} d\zeta^{ext}. \tag{3.55}$$

ζ^{ext} is the (positive) position parameter for the path of integration over the ridge of the phase $-k_p f^{ext}$ in the (Θ_1, ϕ_1) -plane (Fig. 3.15). The stationary point at $(\Theta^{ray D}, \phi^{ray D}) = (160^\circ, 180^\circ)$ corresponds to the position at the droplet surface for which the externally reflected ray D reaches the observation point (Fig. 3.8). The straight line of integration is taken through this stationary point and the point at normal incidence $(\Theta^{norm}, \phi^{norm})$:

$$\Theta_1 = \Theta_1^{norm} \mp \zeta^{ext} \cos(\kappa^{ext}), \tag{3.56}$$

$$\phi_1 = \phi_1^{norm} \mp \zeta^{ext} \sin(\kappa^{ext}), \tag{3.57}$$

$$\kappa^{ext} = \arctan \left[\frac{\phi_1^{norm} - \phi_1^{ray D}}{\Theta_1^{norm} - \Theta_1^{ray D}} \right]. \tag{3.58}$$

The plus sign is utilized when $\Theta_1^{\text{ray D}} > \Theta_1^{\text{norm}}$ and the minus sign refers to the condition $\Theta_1^{\text{ray D}} < \Theta_1^{\text{norm}}$. The stationary point follows from minimizing the phase function f^{ext} to (Θ_1, ϕ_1) . The normal incidence point on the ridge of the phase surface is related to the minimum of the function $-(\mathbf{n} \cdot \mathbf{k}_b) f^{\text{ext}}$. In Fig. 3.16, one can see the phase on the path of integration. Fig. 3.17 depicts the real and imaginary part of the integrand of $K^{\text{ext}}(k_p)$. The numerical integration is performed without applying least-squares fits of f^{ext} or g^{ext} with respect to the position parameter ζ^{ext} .

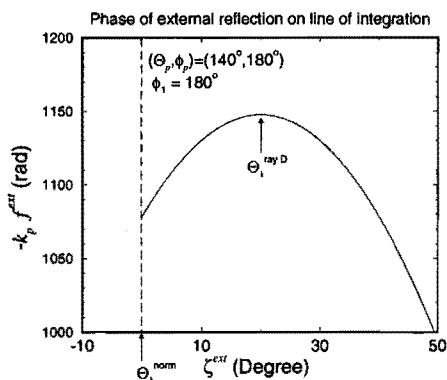


Figure 3.16: The phase $-k_p f^{\text{ext}}$ as a function of the integration variable ζ^{ext} employed in the line integral of Eq. 3.55. The stationary point refers to the position of the externally reflected ray.

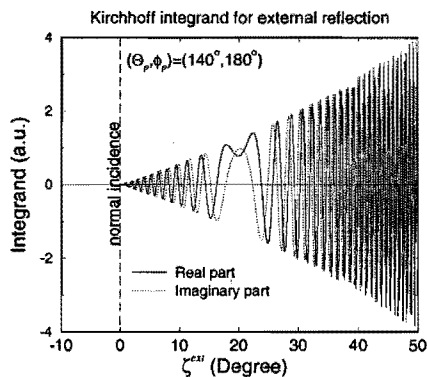


Figure 3.17: The real and imaginary part of the Kirchhoff integrand for external reflection. The influence of the stationary point on the oscillating function is evident.

The final solution for $K(k_p)$ is solved by treating the real and imaginary part of the integral separately. Subsequently, the intensity I for scattered light with polarization vector \mathbf{p}_p in the observation point follows Eq. 2.18:

$$\begin{aligned}
 I \propto & \operatorname{Re}(K^{\text{int}}) \operatorname{Re}(K^{\text{int}}) + \operatorname{Im}(K^{\text{int}}) \operatorname{Im}(K^{\text{int}}) + \\
 & \operatorname{Re}(K^{\text{ext}}) \operatorname{Re}(K^{\text{ext}}) + \operatorname{Im}(K^{\text{ext}}) \operatorname{Im}(K^{\text{ext}}) + \\
 & 2\operatorname{Re}(K^{\text{int}}) \operatorname{Re}(K^{\text{ext}}) + 2\operatorname{Im}(K^{\text{int}}) \operatorname{Im}(K^{\text{ext}}),
 \end{aligned} \tag{3.59}$$

where the variable k_p has been omitted. Re and Im denote the real and imaginary parts, respectively.

3.3 Surface integral method versus Lorenz-Mie theory

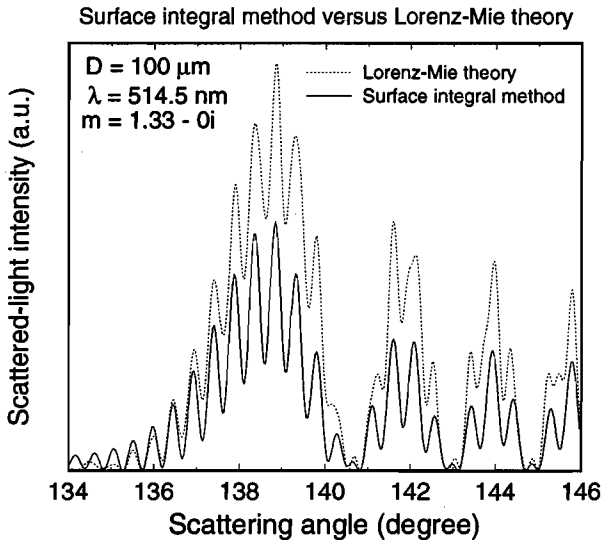


Figure 3.18: *The monochromatic rainbow according to Lorenz-Mie theory and the surface integral method. The scattering problem is a transparent sphere ($D = 100 \mu\text{m}$ and $m = 1.33$), illuminated by a planar wave front having a wavelength of 514.5 nm.*

Numerical results are presented for the spherical scattering problem of Fig. 3.8. The computer program *kirchhoff97.f* [69] solves the Kirchhoff integral for internal and external reflections following the hybrid approach of the preceding section. Fig. 3.18 depicts the resulting monochromatic primary rainbow. The computation took about 2000 s CPU time on a Dec Alpha AXP 3000/400. For the same case the Lorenz-Mie theory has been applied; the result is shown by the dotted curve and it took 50 s on the same machine. The angular positions of the extrema in both curves compare remarkably well. No effort was put into comparing absolute intensities in this work, but it is clear from the graph that the surface integral method overestimates the amplitude of the ripple structure relative to the amplitude of the Airy fringes. This remains to be examined.

The power spectra of both curves (Fig. 3.19) reveal that the angular frequencies connected to internal and external reflection are well predicted. However, the peaks at angular frequencies 2.95° and 3.3° only appear in the Lorenz-Mie computations. These resemble interference between internal reflection and rays coming from the edge of the scatterer (Sec. 1.3). Because the latter is not modeled in the surface integral method, peaks at mentioned frequencies do not exist for

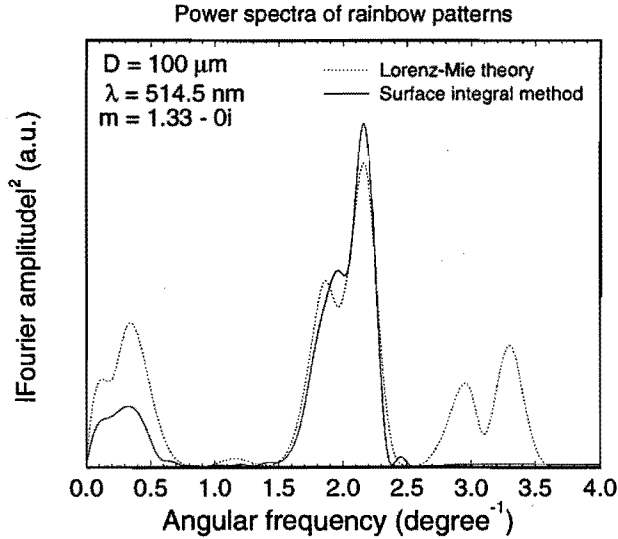


Figure 3.19: *The derivatives of the spectra of Fig. 3.18.*

this method.

3.4 Primary rainbow from prolates and oblates

In principle, the surface integral method can predict the primary rainbow pattern for an ellipsoid arbitrarily oriented with respect to an incident, planar wave front. However, the numerical method utilized in this thesis implies reliable solutions for 2D-scattering problems only (see Subsec. 3.2.2). Here, prolates and oblates are considered. A prolate is an ellipsoid with one long and two short axes of equal length, like a rugby ball. An oblate, on the other hand, has one short and two long axes, like a hamburger. Already in 1910, Moebius[49] found a simple formula for the deviation of the geometric rainbow angle, $\Delta\theta_{rg}$, for the case of collimated light illuminating a prolate or an oblate:

$$\Delta\theta_{rg} = 16 \left(\frac{C - B}{C + B} \right) \frac{\cos \tau_{rg}}{m} \sin^3 \left(\arccos \left(\frac{\cos \tau_{rg}}{m} \right) \right) \cos(\theta_{rg} - 2\Psi), \quad (3.60)$$

$$\text{with } \tau_{rg} = \arcsin \sqrt{\frac{m^2 - 1}{3}}.$$

θ_{rg} is the geometric rainbow angle for a sphere (Sec. 1.2 or Sec. 4.1). B and C are the diameters along the y - and z -axis, respectively. The purely geometrical expression is limited to $B/C \approx 1$. This ratio and the diameter A along the x -axis determine whether the ellipsoid represents an oblate or a prolate. Ψ is the

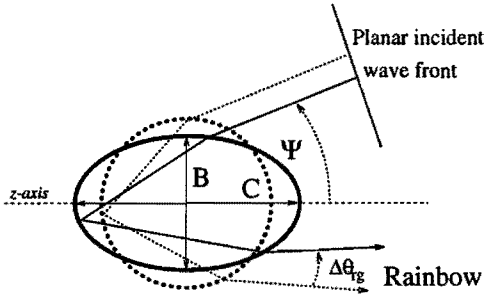


Figure 3.20: *The scattering problem considered by Moebius[49] in 1910.*

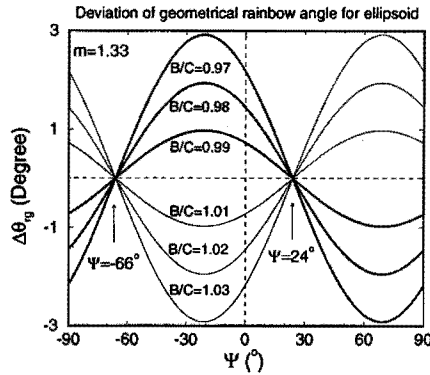


Figure 3.21: $\Delta\theta_{rg}$ as a function of B/C and the angle Ψ according to the expression 3.60.

angle between the incoming beam and the z -axis (Fig. 3.20). As for the surface integral method, the 2D-approach of Moebius only holds for ray paths that lie in the scattering plane taken through the incident and scattered rays. It is also important to realize that the Moebius' approach cannot predict the effect of the non-sphericity on the different interference structures. Yet, it gives an idea about the shift of the entire rainbow pattern as a function of the ratio B/C and the angle Ψ . Fig. 3.21 demonstrates that a non-sphericity of 1% may result in a shift of about 1° , although for $\Psi = -66^\circ$ and $\Psi = 24^\circ$ there is no deviation in θ_{rg} at all.

Fig. 3.22 is obtained using the surface integral method. Primary rainbows are shown for prolates having a short diameter of $100\ \mu\text{m}$ and a long axis length of $103\ \mu\text{m}$. The difference between both interference patterns is the relative position of the prolates. The dotted curve refers to a prolate with the long axis perpendicular to the incoming light rays, i.e. $B/C = 1.03$ and $\Psi = 0^\circ$. For the solid curve, the conditions are $B/C = 0.97$ and $\Psi = 0^\circ$. The angular difference between both main rainbow maxima is approximately 6° . Compared to the spherical case (Fig. 3.18), this difference is -3° and $+3^\circ$, respectively. From the curves of Moebius (Fig. 3.21) one can derive that $\Delta\theta_{rg} = \pm 2.2^\circ$, which is a bit lower.

The power spectra of the rainbow patterns (Fig. 3.23) are taken from the first three Airy fringes of each interference pattern. It reveals that the frequency F_3 , associated to the ripple structure, reveals a much smaller displacement than the peaks at F_1 and F_2 . As $F_1 + F_2 = F_3$ (Eq. 1.6), it is understandable why F_1 changes oppositely to F_2 . In Chaps. 5 and 6 it will be seen that this is an important observation for the rainbow technique.

Figs. 3.24 and 3.25 are equivalent to the two preceding figures except for the dimensions. The dotted curve now represents a sphere of $1015\ \mu\text{m}$. The CPU-time was approximately 10 hrs on the Dec Alpha AXP 3000/400. The solid curve

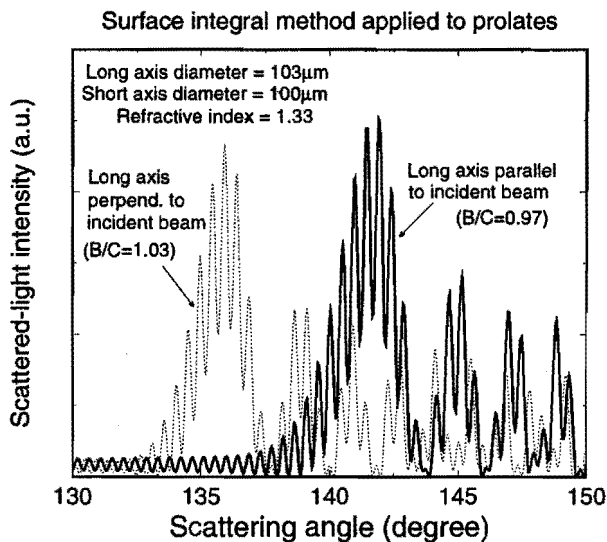


Figure 3.22: Monochromatic rainbow patterns from prolates with an approximate diameter of 100 μm . The ratio B/C refers to Fig. 3.20.

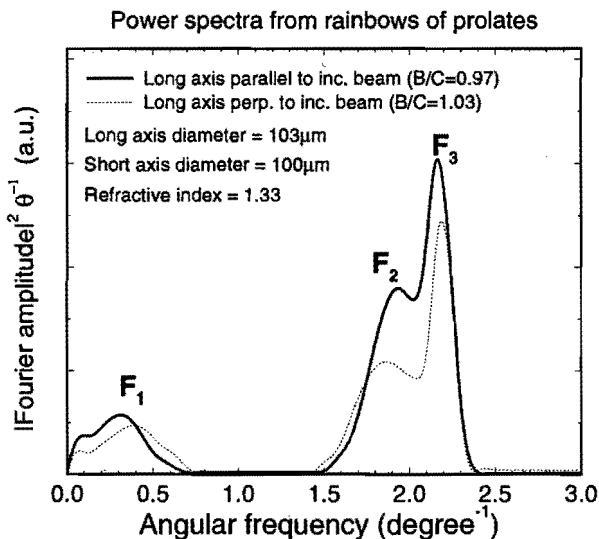


Figure 3.23: Derivative of power spectra of Fig. 3.22.

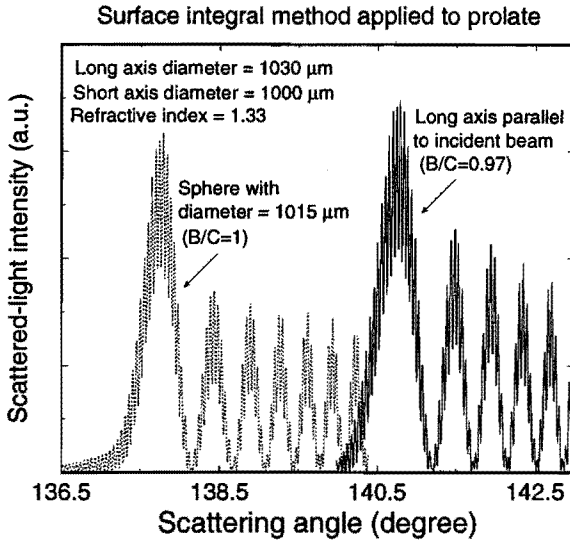


Figure 3.24: Monochromatic rainbow patterns from a sphere of 1015 μm and a prolate with a short axis of 1000 μm and two long axes of 1030 μm . The ratio B/C refers to Fig. 3.20.

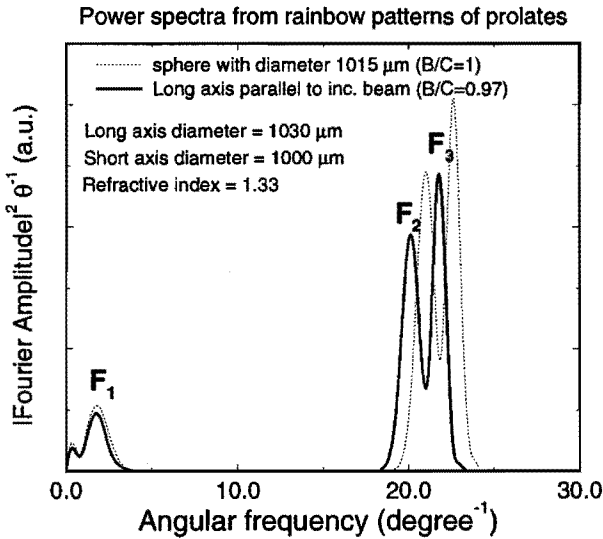


Figure 3.25: Power spectra of the curves in Fig. 3.24.

is produced by a prolate with one long axis of $1030\ \mu\text{m}$ and two short axes of $1000\ \mu\text{m}$. The angular difference between the main rainbow maxima is $\sim 3^\circ$. Comparison with Fig. 3.22 reveals that the angular shift of the rainbow pattern is independent of the dimension of the scatterer. This feature was already predicted by Moebius, though quantitatively his results differ from those obtained here. The absence of a dependence on the dimension does not hold for the angular frequencies as seen in the power spectra. In contrast to Fig. 3.23, F_1 has not moved, whereas the peaks at F_2 and F_3 are displaced by $\sim 5\%$. The implication on the rainbow technique will be discussed in Chap. 5.

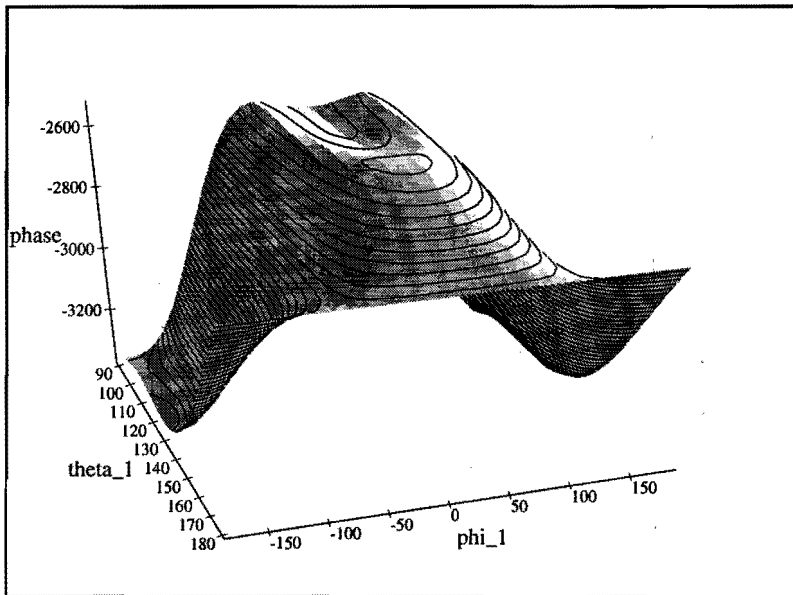


Figure 3.26: *The phase-surface for rays having experienced one internal reflection inside an oblate with axis ratio 1.3. The observation point is taken in the primary rainbow region and lies in the plane where the cross-section of the oblate is circular. The U-shaped ridge is caused by the interference between skew and in-plane rays.*

The results shown in this chapter reveal only a minor part of the potential of the surface integral method. As the geometrical tools given in Sec. 3.1 are fully three-dimensional, the method should in principle be able to predict rainbow patterns including out-of-plane rays when these exist. In 1984, Marston and Trinh[44] and Nye[55] demonstrated that the ordinary rainbow rays (i.e. ray B and ray C in Fig. 3.8) can interfere with two additional once-internally reflected rays for which the optical paths do not lie in one plane. The first authors took photographs

of the scattering diagrams in the rainbow region of an oblate. For certain axis ratios, they observed a *hyperbolic umbilic diffraction catastrophe* which in fact is a generalization of the primary rainbow formed by a spherical drop and manifests parallelograms of high intensity.

Fig. 3.26 shows the phase used for the Kirchhoff integral $K_{int}(k_p)$ (Eq. 3.49) for an oblate with axis ratio 1.3. The observation point lies in the plane taken through the circular cross-section of the oblate at a scattering angle of 150° . The integration is normally carried out over the ridge of the phase-surface which is approximated by a straight line in the (Θ_1, ϕ_1) -plane. However, the ridge in Fig. 3.26 is clearly not linear but U-shaped, which is caused by the skew rays which appeared because the scattering problem was three-dimensional. Therefore, if one aims at computing the resulting interference pattern, an alternative integration procedure has to be developed for the one used in this chapter. Fortunately, the non-sphericity of the scatterer has to be larger than $\sim 20\%$ before the main rainbow maximum consists of interference structures due to out-of-plane rays.

Chapter 4

AIRY THEORY FOR THE RAINBOW

The Lorenz-Mie theory and the surface integral method presented in the preceding chapters are powerful tools for describing various rainbow characteristics. However, they are mathematically complex and a physical interpretation is not always obvious. Therefore, it is interesting to discuss the applicability of ordinary geometrical optics to the rainbow. In Sec. 4.1, the geometric rainbow angle θ_{rg} is derived for a spherical non-absorbing scatterer. Sec. 4.2 employs geometrical optics together with Huygens' principle in order to obtain the Airy theory for the rainbow. Sec. 4.3 compares the latter with the Lorenz-Mie theory and the surface integral method.

4.1 The rainbow from a sphere according to geometrical optics

Geometrical optics treats light as rays. The light path of a ray through a transparent, spherical droplet results from refraction and reflection (Fig. 4.1). The relationship between the scattering angle θ , the incidence angle τ , and the angle inside the droplet τ' , was already found by Descartes and discussed in the Introduction:

$$\theta = 2\tau - 2(N - 1)\tau'. \quad (4.1)$$

N refers to the number of interactions that a scattered light ray has experienced with the droplet surface. Snell's law relates the angles τ and τ' as

$$\cos \tau = m \cos \tau', \quad (4.2)$$

where m is the refractive index of the medium inside the droplet; the refractive index of the surrounding medium has been taken unity. Substitution of Eq. 4.2 in Eq. 4.1 results in the scattering angle θ as a function of the incidence angle τ . This function is drawn in Fig. 4.2 for $N = 1$ to $N = 5$. The figure indicates maxima in the curves for $N \geq 3$. These maxima are related to rays for which the deflection is stationary with respect to small changes in τ . Rainbows are observed near the

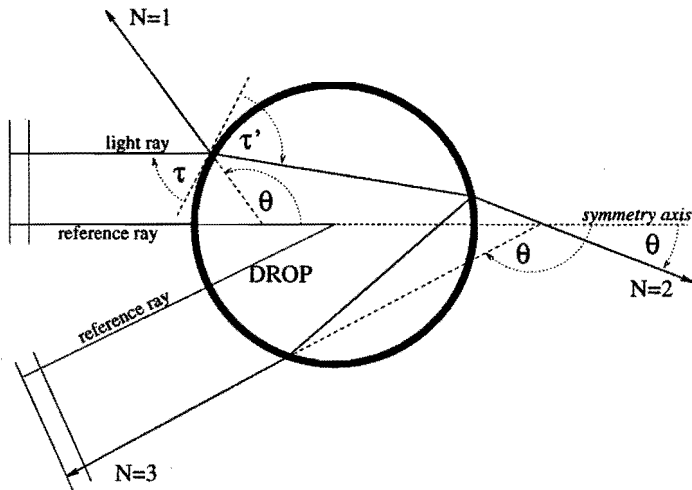


Figure 4.1: Light paths of refracted and reflected geometrical rays in a spherical transparent drop. Integer N refers to a scattered ray that has experienced N interface interactions. A scattering angle θ can be assigned to each ray. The phase difference between the scattered and incident ray is computed with respect to the reference ray.

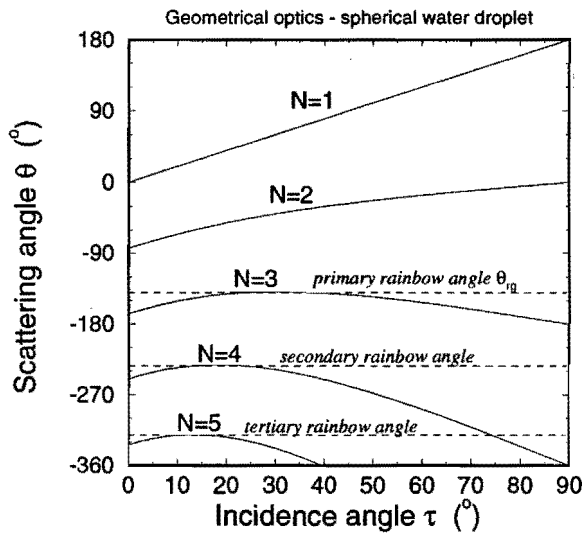


Figure 4.2: Scattering angle θ as a function of angle τ for refractive index $m = 1.33$ and for $N = 1$ to $N = 5$.

corresponding scattering angles. Consequently, the geometrical expression for the rainbow of order $N - 2$ can be found by solving Eqs. 4.1 and 4.2 by imposing

$$\left. \frac{d\theta}{d\tau} \right|_{N-2} = 0. \quad (4.3)$$

For the primary rainbow, this leads to the incidence angle τ_{rg} , for which the corresponding scattering angle is the geometric rainbow angle θ_{rg} :

$$\sin \tau_{rg} = \sqrt{\frac{m^2 - 1}{3}}, \quad (4.4)$$

$$\theta_{rg} = 2\tau_{rg} - 4 \arccos \left(\frac{1}{m} \cos \tau_{rg} \right). \quad (4.5)$$

Fig. 4.3 depicts $|\theta_{rg}|$ as a function of the refractive index.

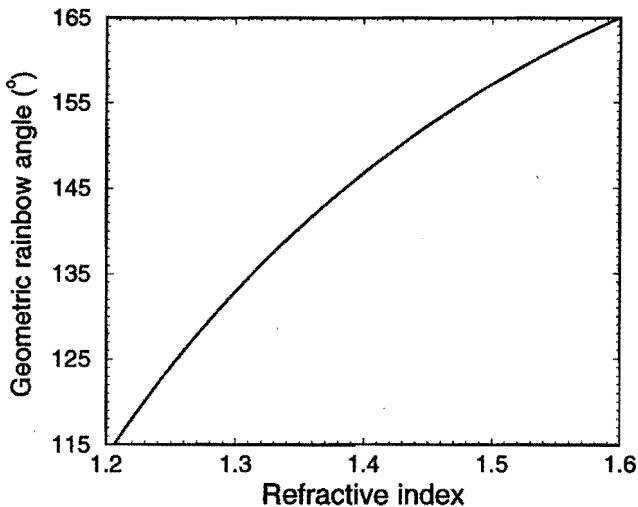


Figure 4.3: The geometric rainbow angle $|\theta_{rg}|$, for $N = 3$ as a function of the refractive index, m .

The refractive index m is a function of temperature T , the wavelength of the incident light λ , and the pressure P . Thormählen et al.[67] constructed a function for m of water with λ , T and P as independent variables. Its coefficients are directly deduced from available experimental data by least-squares fit. Fig. 4.4 depicts the refractive index as a function of the temperature at atmospheric pressure and at $\lambda = 514.5$ nm. Upon substitution of this function in Eqs. 4.4 and 4.5, the geometric rainbow angle depends only on the temperature when the pressure and wavelength

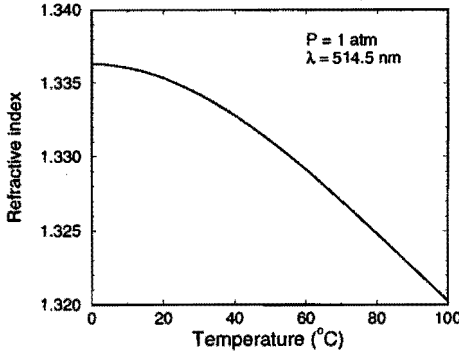


Figure 4.4: The refractive index of water as a function of the temperature for a pressure of $P = 1 \text{ atm}$ and a wavelength of light of $\lambda = 514.5 \text{ nm}$ (see Ref.[67]).

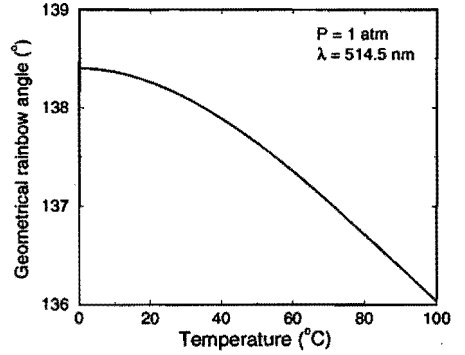


Figure 4.5: Geometric rainbow angle, $|\theta_{rg}|$, for water droplets as a function of temperature for $P = 1 \text{ atm}$, $\lambda = 514.5 \text{ nm}$ and for ray of order $p = 2$.

are constant. This is the case when a droplet at constant pressure is illuminated by a laser beam. Fig. 4.5 depicts $|\theta_{rg}|$ as a function of the droplet temperature. A change in temperature from 0°C to 100°C causes a shift of the geometric rainbow angle of about 2.3° . Note the small dependency of θ_{rg} on the temperature between 0°C and 20°C .

4.2 Airy fringes

Geometrical optics is only able to predict an approximate angle about which the rainbow pattern is situated. To determine rainbow phenomena such as the dependency of its interference structures on the droplet size, the principle of optical interference has to be applied, thus leaving the domain of geometrical optics. One can proceed by computing the phase difference $\Delta\beta$ between intersecting rays, that is to say between rays that are parallel in the far field. According to the phase difference, destructive or constructive interference occurs, resulting in a minimum or maximum in light intensity. This principle requires an expression for the phase β of a scattered light ray with respect to a reference ray as was depicted in Fig. 4.1:

$$\beta = \frac{2\pi D}{\lambda} (\sin \tau - (N - 1)m \sin \tau'). \quad (4.6)$$

The relationship between the angles τ and τ' is given by Snell's law (Eq. 4.2). Unfortunately, the computation of the scattered-light intensity, based on the evaluation of $\Delta\beta$ between two parallel rays having experienced one internal reflection, fails near the geometric rainbow angle θ_{rg} . For $|\theta| \downarrow |\theta_{rg}|$, the intensity would become infinite and for $|\theta| < |\theta_{rg}|$ geometrical rays are non-existent, thus the intensity

would drop to zero at once, which is not physical (see for example Nussenzveig[54] for graphical demonstration). To encompass these features, one needs to include diffraction of light rays in the neighborhood of the geometric rainbow angle. One possibility is to apply the diffraction-like Kirchoff integral which was the subject of Chap. 3. However, in the present chapter another approach is followed which gives more physical insight. It is the approach of Airy[4] who tried to include diffraction in the geometric rainbow description by using Huygens' principle on the propagation of an arbitrary wave front (see for example Van de Hulst[83]).

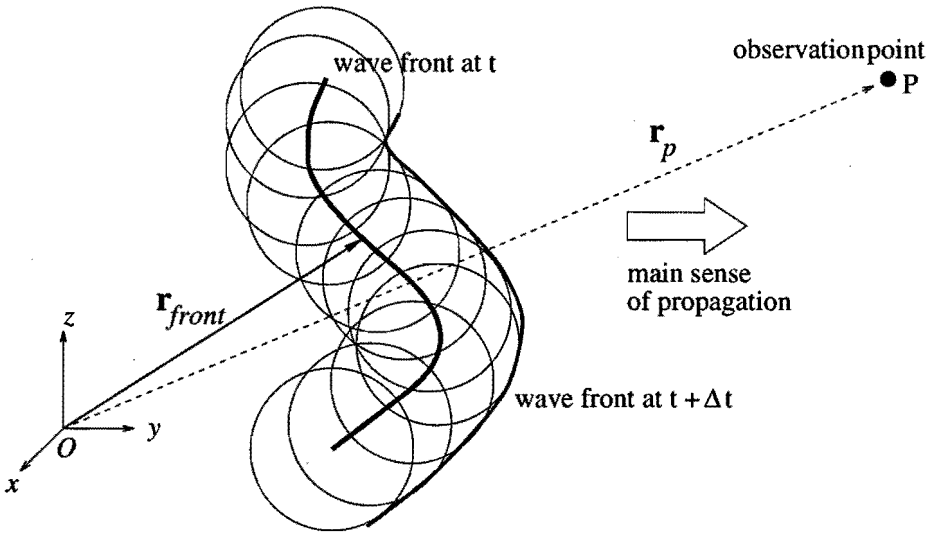


Figure 4.6: Propagation of a wave front according to Huygens' principle. The new wave front at time $t + \Delta t$ is made by the envelope of the secondary spherical waves emitted by each point on the wave front at time t . The principle has to be treated with care because by equal reasoning it allows the wave front to propagate backwards.

Huygens' principle dates from 1678 and states that each point on a wave front emits a secondary spherical wave at time t . The envelope of these waves at time $t + \Delta t$ interferes in a constructive manner to form the new wave front (Fig. 4.6). Based on Huygens' principle, in 1818 Fresnel found in a mathematical formulation for the amplitude of the electric field E_p in the observation point P. The formulation expresses E_p in terms of an integral over the electric-field amplitude in the wave front:

$$E_p = \frac{ie^{-i\omega t}}{\lambda \|\mathbf{r}_{front} - \mathbf{r}_p\|} \iint_{front} e^{i\frac{2\pi}{\lambda} \|\mathbf{r}_{front} - \mathbf{r}_p\|} da. \quad (4.7)$$

\mathbf{r}_{front} is the position vector for the wave front and \mathbf{r}_p points at the observation point. Note that the amplitude of the electric field in the wave front was taken unity. Moreover, the formula is only valid when $(\mathbf{r}_{front} - \mathbf{r}_p)$ is pointing in a

direction not too far from the main sense of propagation. Without this condition there would also exist a wave traveling backwards, as can be deduced from Fig. 4.6. Fresnel introduced an artificial inclination factor in his formula to correct for this inconsistency (see e.g. Hecht[30]). Later, in 1882, Kirchhoff found a more robust description of the Huygens' principle based on the differential wave equations; the forced introduction of an inclination factor was not necessary any longer. Kirchhoff's analysis led to Eq. 3.41 in Chap. 3.

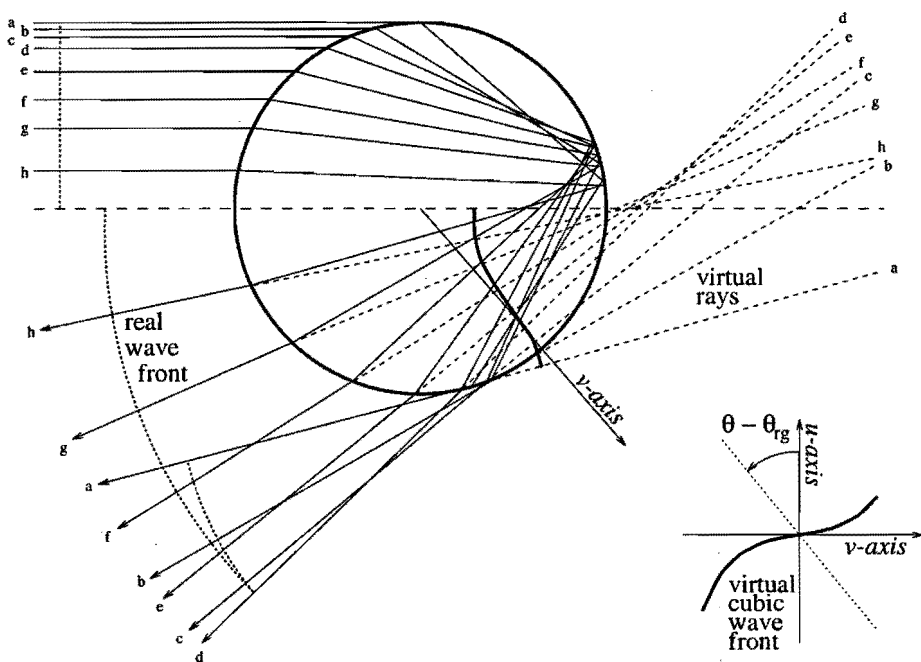


Figure 4.7: 8 rays in a plane wave front impinging on a droplet and emerging from it with a virtual cubic wave front near the geometric rainbow angle (see Van de Hulst[82]).

In order to apply Fresnel's integral to the primary rainbow, an expression for the wave front has to be found when it exits the droplet after one internal reflection. However, it is convenient to apply Huygens' principle to the virtual wave front as sketched in Fig. 4.7. The shape of this virtual front is approximately cubic in a local Cartesian (u, v) -coordinate system. The v -axis is tangential to the deflection point and goes through the centre of the sphere. Ray d leaves the droplet at the geometric rainbow angle and virtually passes the deflection point perpendicularly. In the vicinity of this point, the virtual cubic wave front is in first approximation planar, thus identical to the incident wave front. This means that the distances between the rays are about the same in the virtual as in the incident wave front

which leads to¹:

$$v = \frac{D}{2}(\cos \tau - \cos \tau_{rg}) \approx -\frac{D}{2} \sin \tau_{rg}(\tau - \tau_{rg}). \quad (4.8)$$

The relative angular direction $\theta - \theta_{rg}$, in which the observation point is placed, is related to the (u, v) -coordinates as

$$\frac{du}{dv} = (\theta - \theta_{rg}), \quad (4.9)$$

and can be expanded about $\tau = \tau_{rg}$:

$$\theta - \theta_{rg} = \left. \frac{\partial \theta}{\partial \tau} \right|_{\tau_{rg}} (\tau - \tau_{rg}) - \frac{1}{2} \left. \frac{\partial^2 \theta}{\partial \tau^2} \right|_{\tau_{rg}} (\tau - \tau_{rg})^2. \quad (4.10)$$

$\left. \frac{\partial \theta}{\partial \tau} \right|_{\tau_{rg}} = 0$ as was explained in Eq. 4.3 of the previous section. The same condition reduces the second derivative of the scattering angle with respect to the incidence angle into the simple expression

$$\left. \frac{\partial^2 \theta}{\partial \tau^2} \right|_{\tau_{rg}} = \frac{-3}{2 \tan \tau_{rg}}. \quad (4.11)$$

The four preceding expressions are combined to form the cubic equation of the virtual wave front:

$$u = \underbrace{\left(\frac{1}{\tan \tau_{rg} \sin^2 \tau_{rg}} \right)}_h \frac{v^3}{D^2} = h \frac{v^3}{D^2}. \quad (4.12)$$

With this knowledge, the vector \mathbf{r}_{front} for the wave front can be constructed:

$$\mathbf{r}_{front} = v \mathbf{e}_v + h \frac{v^3}{D^2} \mathbf{e}_u, \quad (4.13)$$

where the origin of the (u, v) -coordinate system served as origin for the vector. Taking the same origin for \mathbf{r}_p leads to

$$\mathbf{r}_p = r_p(\theta - \theta_{rg}) \mathbf{e}_v + r_p \mathbf{e}_u. \quad (4.14)$$

r_p is the absolute value of \mathbf{r}_p . The distance between the wave front and the point of observation can now be computed:

$$\|\mathbf{r}_{front} - \mathbf{r}_p\| = r_p \sqrt{1 + (\theta - \theta_{rg})^2 - \frac{2v(\theta - \theta_{rg})}{r_p} - \frac{2hv^3}{r_p D^2} + \frac{v^2}{r_p^2} + \frac{h^2 v^6}{r_p^2 D^4}}. \quad (4.15)$$

¹In this section the angles τ and θ are exceptionally expressed in radian.

Imposing the far-field condition implies that the 5th and 6th term can be neglected. Also the 2nd can be left out because $(\theta - \theta_{rg})^2 \ll 1$ and it is not a function of v . The simplified expression can be expanded in order to get rid of the square root:

$$\|\mathbf{r}_{front} - \mathbf{r}_p\| = r_p - v(\theta - \theta_{rg}) - h \frac{v^3}{D^2}. \quad (4.16)$$

Substitution into Fresnel's integral yields

$$E_p = \frac{i e^{i(\frac{2\pi}{\lambda} r_p - \omega t)}}{\lambda r_p} \int_{-\infty}^{+\infty} e^{i \frac{2\pi}{\lambda} (-v(\theta - \theta_{rg}) - h \frac{v^3}{D^2})} dv. \quad (4.17)$$

As stationary points in the integrand only exist close to $v = 0$, the integral over the virtual wave front could be extended to $v = -\infty$ and $v = +\infty$ to generalize the mathematical formulation. Airy combined the positive and negative part and dropped the term in front of the integral in order to arrive at the rainbow integral²

$$\Omega_{rainbow}(z) = \int_0^{\infty} \cos \frac{1}{2} \pi (z\eta - \eta^3) d\eta, \quad (4.18)$$

which is also known as the Airy function (see Abramowitz and Stegun[2]). To obtain the scattered light intensity in the observation point, $\Omega_{rainbow}^2(z)$ has to be evaluated. The relationship between integration variable η and the v -coordinate was defined as

$$\eta = v \left(\frac{4h}{\lambda D^2} \right)^{1/3}. \quad (4.19)$$

The non-dimensional parameter z denotes the normalized angular deviation from the geometric rainbow angle and reads

$$z = -(\theta - \theta_{rg}) \left(\frac{16D^2}{h\lambda^2} \right)^{1/3}. \quad (4.20)$$

Note that the rainbow integral was already utilized in Subsec. 3.2.2 (Eq. 3.45) as an example to illustrate the influence of stationary points on the outcome of the integral. The resulting method of stationary phase has been employed by Lock and Andrews[38] to solve the rainbow integral. The method runs into difficulties near θ_{rg} because the stationary points merge together and disappear for $|\theta| < |\theta_{rg}|$. To avoid these kind of problems here, a full numerical integration has been performed from $\eta = 0$ to $\eta = \infty$. The integration has to be done with care because the integrand oscillates more and more between -1 and $+1$ when η goes to infinity. Consequently, the η -axis cannot be divided into equidistant intervals because then the numerical computation would be divergent. Therefore, one has to rewrite

²It is important to realize that in 1937, Van der Pol and Bremmer[85, 10] successfully deduced the rainbow integral starting from the far-field approximated Lorenz-Mie series S_1 , expressed in Eq. 2.63. More than forty years later, Nussenzeig[53] presented the complex angular momentum (CAM) theory of the rainbow based on the same derivation.

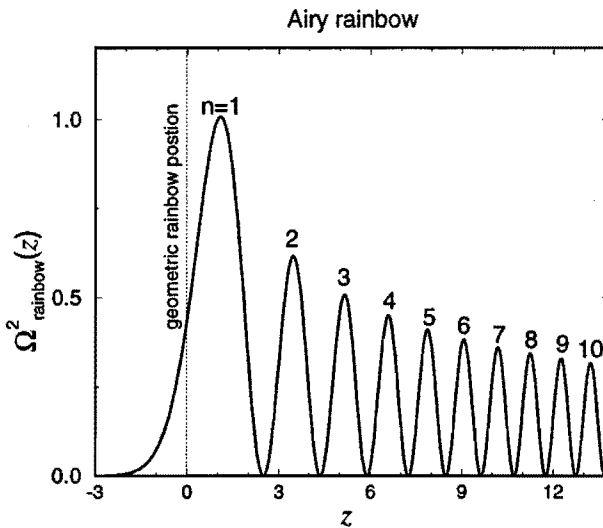


Figure 4.8: The square of the rainbow integral, $\Omega^2_{rainbow}(z)$, as a function of z , i.e. the non-dimensional deviation of the scattering angle from the geometric rainbow angle.

$\Omega_{rainbow}(z)$ as a sum of finite-range integrals. The boundaries of those intervals are η_i and correspond to values at which the integrand goes through the zero-axis:

$$\Omega_{rainbow}(z) = \sum_{i=0}^{\infty} \int_{\eta_i}^{\eta_{i+1}} \cos \frac{1}{2} \pi (z\eta - \eta^3) d\eta. \quad (4.21)$$

The numerical value of each finite-range integral decreases with increasing η_i . In addition, it is alternately positive and negative. Thus, convergence of the series is ensured.

Figure 4.8 depicts $\Omega^2_{rainbow}(z)$ versus z . The interference pattern is known as the Airy rainbow consisting of the main rainbow maximum and the subsidiary supernumerary bows. Note that the geometric rainbow angle is positioned at $z = 0$ and that at this angle the light intensity is only 43.93 % of the intensity in the main rainbow maximum.

The Airy theory is thus able to predict a rainbow without discontinuities or infinite values near $z = 0$. Table 4.1 lists the values of z at which the first ten extrema in the Airy rainbow occur. It will be seen in Chaps. 5 and 6 that these values are of practical use for the rainbow technique.

	n	z	$\Omega_{\text{rainbow}}^2(z)$
<i>Main rainbow maximum</i>	1	1.08728	1.0075
<i>Minimum</i>		2.49550	0
<i>1st subsidiary maximum</i>	2	3.46687	0.6165
<i>Minimum</i>		4.36314	0
<i>2nd subsidiary maximum</i>	3	5.14458	0.5081
<i>Minimum</i>		5.89219	0
<i>3rd subsidiary maximum</i>	4	6.57824	0.4498
<i>Minimum</i>		7.24358	0
<i>4th subsidiary maximum</i>	5	7.86847	0.4114
<i>Minimum</i>		8.47892	0
<i>5th subsidiary maximum</i>	6	9.05989	0.3835
<i>Minimum</i>		9.63004	0
<i>6th subsidiary maximum</i>	7	10.17736	0.3619
<i>Minimum</i>		10.71606	0
<i>7th subsidiary maximum</i>	8	11.23636	0.3444
<i>Minimum</i>		11.74960	0
<i>8th subsidiary maximum</i>	9	12.24753	0.3299
<i>Minimum</i>		12.73952	0
<i>9th subsidiary maximum</i>	10	13.21851	0.3176
<i>Minimum</i>		13.69238	0

Table 4.1: Extrema in the square of the rainbow-integral.

4.3 Domain of validity of the Airy theory

The domain of validity of the Airy theory has first been estimated by Van de Hulst[82]. He stated that “*Airy’s approximation is useful as a quantitative rainbow theory only if no rays with a deflection more than about half a degree from the geometric rainbow are involved*”. Later, when sufficiently fast computers were available, Wang and Van de Hulst[87] carried out a comparison between the Lorenz-Mie theory and the Airy approximation in order to justify this statement. A similar comparison will be performed here but biased towards the rainbow technique which employs the Airy theory. The technique (Chaps. 5 and 6) does not rely on the accuracy of the predicted intensity distribution. It depends on the precision in the positions of the maxima that were listed in Table 4.1.

In order to make a comparison between Airy and Lorenz-Mie theory, one has to realize that this is only possible for light polarized perpendicularly to the scattering plane. The reason is that no Fresnel coefficients are utilized in the Airy

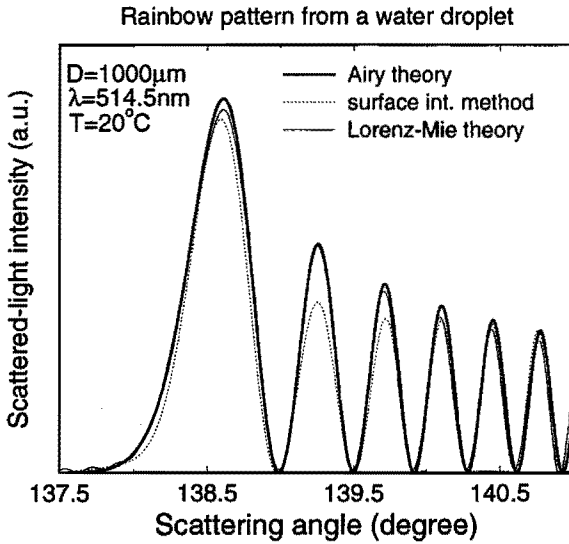


Figure 4.9: The scattered-light intensity as a function of the scattering angle in the primary rainbow region according to three different theories. The size of the water droplet is $D = 1 \text{ mm}$, the wavelength is $\lambda = 514.5 \text{ nm}$ and the temperature equals $T = 20^\circ\text{C}$.

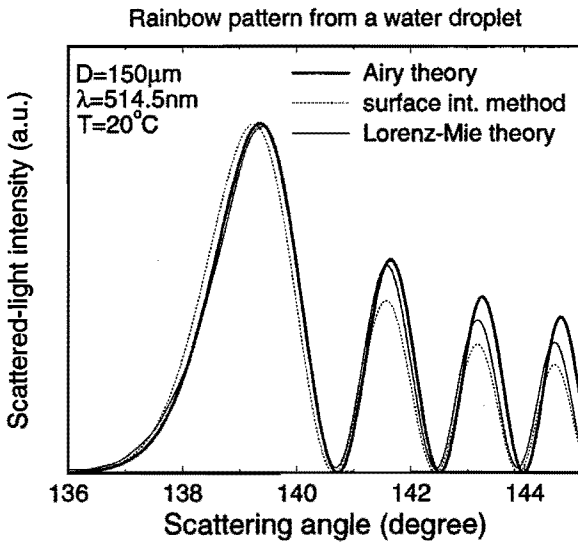


Figure 4.10: Identical to Fig. 4.9 but for a droplet diameter of $D = 150 \mu\text{m}$.

theory to account for the diminishing of the light intensity assigned to a light ray (Subsec. 3.1.2). This is why the amplitude of the electric field in the virtual cubic wave front was taken constant (Eq. 4.7). For the polarization parallel to the scattering plane, the internal-reflection coefficient is zero and changes sign at the Brewster angle. This means that part of the cubic wave front will have advanced π in phase with respect to the other part. For refractive indices between 1.3 and 1.4, the resulting discontinuity of π in phase occurs coincidentally near the geometric rainbow ray, thus near the deflection point of the wave front. The first consequence is that the scattered-light intensity will approach zero near θ_{rg} which explains the polarized behaviour of the rainbow, as mentioned in the Introduction. Secondly, the sign change of the Fresnel coefficient dictates that the intensity maxima will be situated where the Airy theory predicts minima.

Fig. 4.9 has been produced with the polarization perpendicular to the scattering plane. It shows the scattered-light diagram according to three different methods for $D = 1$ mm, $T = 20^\circ\text{C}$ and $\lambda = 514.5$ nm. The bold curve represents $\Omega_{rainbow}^2(z)$ resulting from the Airy theory. Therefore, the normalized angular deviation z had to be transformed into the scattering angle $|\theta|$ using Eq. 4.20:

$$|\theta| = -\theta_{rg} + z \left(\frac{h\lambda^2}{16D^2} \right)^{1/3} \frac{180^\circ}{\pi}. \quad (4.22)$$

Note that, in contrast to Eq. 4.20, $|\theta|$ is expressed in degree angle. The thin curve in Fig. 4.9 arises from the Lorenz-Mie theory. The high-frequency oscillations have been filtered out so that the Airy fringes remain. The third curve is obtained by means of the surface integral method (Chap. 3). For this method no filtering procedure was necessary because the ripple structure can be “switched off” through considering only internally-reflected light rays (Eq. 3.49). The comparison between the three methods is astonishing. It shows that Van de Hulst was a bit too pessimistic in 1957, which he and Wang[87] recognized in 1991. The domain of validity of the Airy theory can be extended to rays with a deflection of at least 2° from the geometric rainbow angle. The surface integral method performs worst of the three methods. This is believed to be due to the approximations that had to be made in order to decrease the CPU time to an acceptable value (see Sec. 3.2).

Fig. 4.10 is identical to Fig. 4.9 except for the size which now measures $150 \mu\text{m}$ instead of 1 mm. Note the widening of the interference pattern. The main rainbow maximum of the Airy pattern agrees almost perfectly with the one of the Lorenz-Mie theory. The first subsidiary maximum lies already outside the limits of validity which is manifested by the angular shift of 0.07° . Remark that the surface integral method reveals the opposite behaviour, that is to say that correct angular positions of the supernumerary arcs are predicted whereas the main rainbow maximum is shifted $\sim 0.2^\circ$.

As mentioned before, the rainbow technique relies on the precision in the determination of the positions of the intensity maxima, in particular the first two. Therefore, Figs. 4.11 and 4.12 have been plotted (see Van Beeck and Riethmuller[71]).

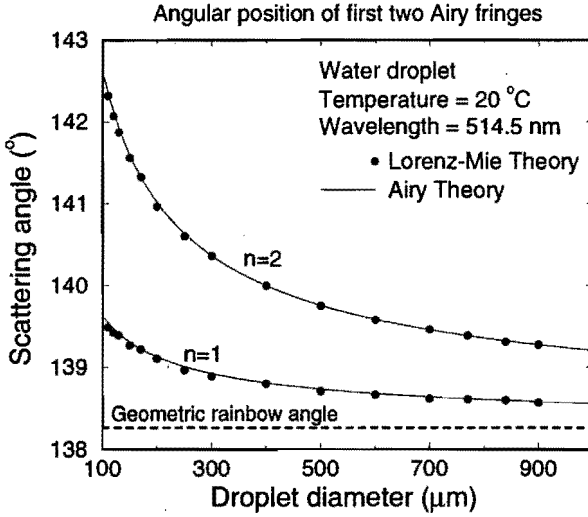


Figure 4.11: The angular positions of the first two maxima in the Airy rainbow (i.e. $n = 1$ and $n = 2$) as a function of the droplet diameter for $T = 20\text{ }^\circ\text{C}$, $\lambda = 514.5\text{ nm}$ and $P = 1\text{ atm}$.

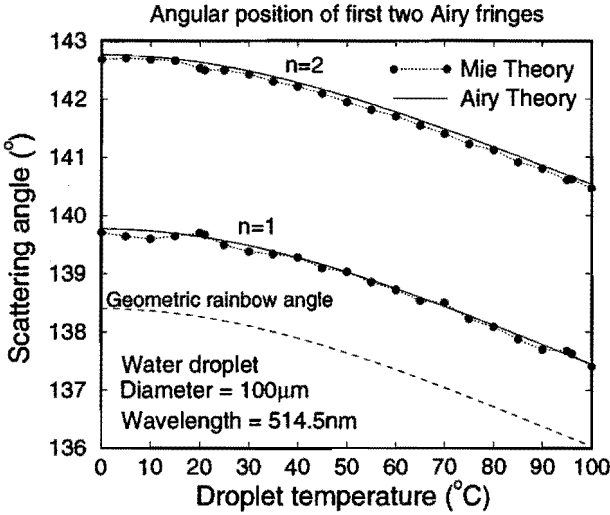


Figure 4.12: The angular positions of the first two maxima in the Airy rainbow as a function of the droplet temperature for $D = 100\text{ }\mu\text{m}$, $\lambda = 514.5\text{ nm}$ and $P = 1\text{ atm}$.

Fig. 4.11 shows the angular positions of the first two maxima as a function of the diameter of a water droplet at $T = 20^\circ\text{C}$. Airy and Lorenz-Mie theory compare well. Yet, for diameters smaller than $200\ \mu\text{m}$, small deviations occur for both maxima in the order of 0.1° . In Fig. 4.11, this is studied more in detail by depicting the maxima for $D = 100\ \mu\text{m}$ as a function of the droplet temperature. The wiggles in the computations of the Lorenz-Mie theory are remarkable. They are not due to the filtering procedure. For the main rainbow maximum, i.e. $n = 1$, they even cause an ambiguity in the scattering angle around $T = 20^\circ$. The curve for $n = 2$ reveals less wiggles but an angular shift of $\sim 0.1^\circ$.

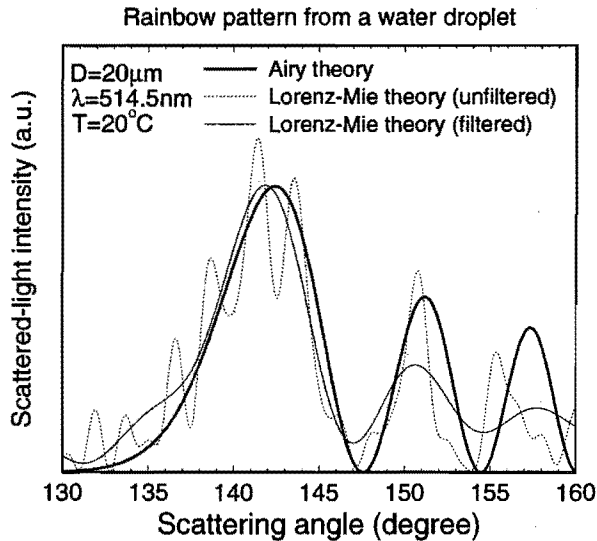


Figure 4.13: *Rainbow patterns according to Lorenz-Mie and Airy theory for a droplet of $D = 20\ \mu\text{m}$ and a size parameter of $x = 122$. This size represents about the lower limit for which two Airy fringes in the rainbow can be recognized.*

Fig. 4.13 demonstrates that it is dangerous to compare the Airy and Lorenz-Mie theories for sizes smaller than $100\ \mu\text{m}$ (see also Roth et al.[61]). A rainbow pattern for a droplet having a diameter of $D = 20\ \mu\text{m}$ is shown (with size parameter $x = 122$). Apart from Airy's rainbow and the filtered Lorenz-Mie curve, the un-filtered one is plotted. It is clear that the angular frequency of the ripple structure approaches the angular frequency of the Airy fringes. Moreover, *ripple* structure is a euphemism for an interference structure that almost dominates the supernumerary bows. As a consequence, the filtered pattern has to be produced with great care. Even then, a comparison with the Airy theory is only meaningful for the main rainbow maximum and one subsidiary Airy fringe. The angular shift between the theories is present for both maxima and has increased to $\sim 1^\circ$.

Chapter 5

RAINBOW-INTERFEROMETRIC MEASUREMENTS OF DROPLET SIZE AND TEMPERATURE

The monochromatic rainbow can be used to non-intrusively measure size and temperature of single droplets. Therefore, it is possible to detect the primary rainbow by means of a linear charge-coupled device (CCD) camera (Sec. 5.1). The Airy theory for the rainbow is used to determine both scalar physical quantities (Sec. 5.2) after the signal has been identified as coming from a spherical droplet (Sec. 5.3). Sec. 5.4 describes the dynamic calibration procedure necessary for the rainbow technique. Experimental results are presented in Sec. 5.5 and the chapter ends with a short discussion on a frequently-recorded type of abnormal rainbow pattern.

5.1 Detection of the monochromatic rainbow by a linear CCD camera

The experimental setup is depicted in Fig. 5.1. At ambient conditions ($T = 21.7^\circ\text{C}$), satellite droplets around a downward-directed unstable water-jet cross a laser beam coming from an Ar-ion laser operated at 2 W and a wavelength of $\lambda = 514.5\text{ nm}$. The beam diameter measures $\sim 4\text{ mm}$. The generated monochromatic rainbow is projected onto the digital linear CCD camera "IDC100" from I2S. The linear array of the camera counts 1728 pixels and measures $17.28\text{ mm} \times 0.013\text{ mm}$. The camera and laser beam form a horizontal scattering plane. The polarization of the laser light is linear and perpendicular to this plane.

The linear CCD array is placed in the focal plane of a positive lens. As such, the detected scattered-light intensity satisfies the far-field condition. The relationship between the scattering angle θ (as defined in Fig. 5.1) and the position y of the

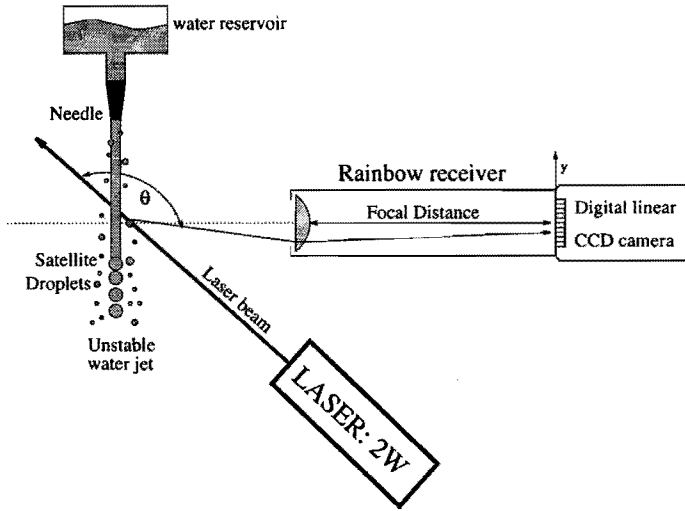


Figure 5.1: Schematic of the optical configuration utilized to detect a rainbow signal with a linear charge-coupled device (CCD). Satellite droplets ($0.5 \text{ mm} < D < 1 \text{ mm}$) nearby an unstable water jet are illuminated by an Ar-ion laser beam to create the rainbow pattern. y indicates the position on the CCD array.

scattered ray at the CCD array, holds

$$\theta - \theta_{ref} = \frac{1}{f}(y - y_{ref}) \frac{180^\circ}{\pi}, \quad (5.1)$$

provided that $y - y_{ref} \ll f$. y_{ref} is the reference position on the CCD array where a ray with reference angle θ_{ref} hits the array. It is important to notice that Eq. 5.1 does not involve the position of the droplet with respect to the lens. This means that the position of a rainbow pattern on the CCD array is independent of the position of the droplet in the laser beam. Nevertheless, one has to ensure that the range of scattering angles reaching the lens at least matches the angular view of the camera, which is here $\sim 5^\circ$.

The camera has both analog and digital outputs. The digitized signal contains 64 intensity levels and is recorded by a data-acquisition card installed inside a personal computer. The camera continuously takes samples of linear images that are integrated over 0.3 ms, which is about the transient time of the droplet in the laser beam. This time is long enough to acquire sufficient scattered light and is short enough to ensure the detection of one rainbow at a time. A signal will be stored as soon as the camera has detected a pattern with a peak intensity higher than 10 intensity levels.

Fig. 5.2 shows the scattered-light intensity for a rainbow pattern as a function of the pixel number. It shows rainbow phenomena such as the Airy fringes and the ripple structure; related frequencies appear in the derivative of the power spectrum

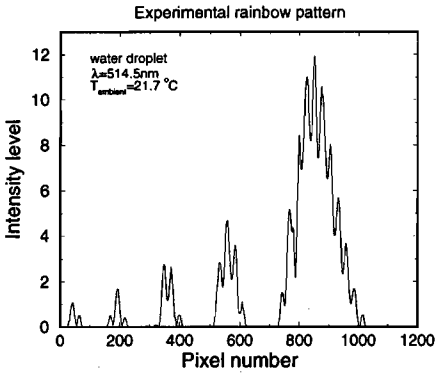


Figure 5.2: *Experimental rainbow pattern recorded by the linear CCD camera in the experimental set-up of Fig. 5.1. The signal is averaged over 5 pixels to suppress the noise and the discretized behaviour. The dip near pixel number 787 is a camera defect.*

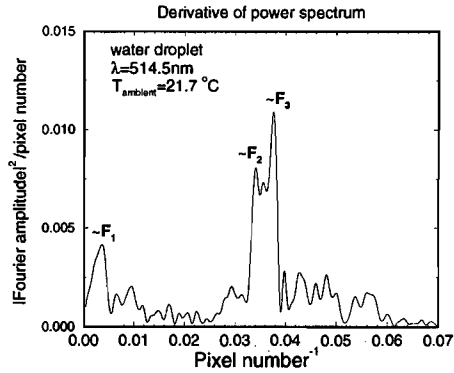


Figure 5.3: *Derivative of the power spectrum of the experimental rainbow pattern of Fig. 5.2.*

(Fig. 5.3). How to relate these characteristics to physical quantities is explained in the following section.

5.2 Simultaneous determination of droplet size and temperature

In previous chapters it was seen that the rainbow pattern depends on droplet size and refractive index, therefore on the temperature. Both size and temperature can be determined from an experimental rainbow pattern detected by the linear CCD camera depicted in Fig. 5.1. To achieve this, a measurement procedure has to be applied that is explained with the help of Figs. 5.4 and 5.5. The various curves correspond to the angular positions of the maxima, θ_1 to θ_5 , of the 5 first Airy fringes according to the Airy theory (Chap. 4). The wavelength of the laser light is $\lambda = 514.5$ nm. In Fig. 5.4, the droplet size is varied for a constant temperature $T = 20^\circ\text{C}$. Fig. 5.5 represents the 5 maxima as a function of the droplet temperature for a diameter of $D = 1$ mm. From the latter figure, one can see that the distance between the Airy fringes is independent of the droplet temperature; close study reveals a change of only 1% in this distance over a temperature range of 100°C . Consequently, the droplet diameter can be deduced from any fringe spacing without knowing the temperature precisely beforehand. The domain of validity of the Airy rainbow decreases the further the Airy fringes elongate from

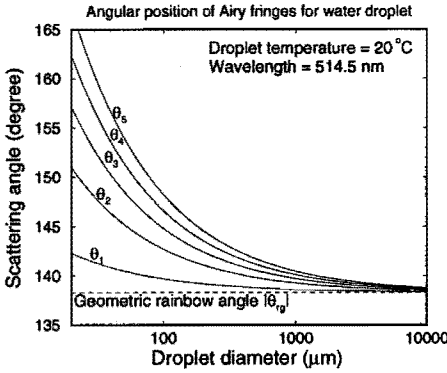


Figure 5.4: First five maxima in the Airy rainbow pattern as a function of the diameter of a water droplet at $T = 20^\circ\text{C}$.

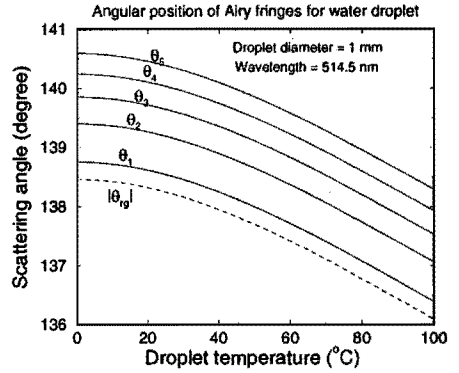


Figure 5.5: First five maxima in the Airy rainbow pattern as a function of the temperature of a water droplet having a diameter of $D = 1\text{ mm}$.

the geometric rainbow angle. It has therefore been decided to relate the so-called Airy diameter D_{Airy} to the distance between the first two Airy fringes. Van Beeck and Riethmuller[72] employed Eq. 4.20 and table 4.1 in order to arrive at

$$D_{Airy} = \frac{\lambda}{4} \left(\frac{\cos \tau_{rg}}{\sin^3 \tau_{rg}} \right)^{\frac{1}{2}} \left(\frac{2.37959}{(\theta_2 - \theta_1)} \frac{180^\circ}{\pi} \right)^{\frac{2}{3}}, \quad (5.2)$$

with $\sin \tau_{rg} = \sqrt{\frac{m^2 - 1}{3}}$.

For $m = 4/3$, the relationship reduces to

$$D_{Airy} = 1016.2 \lambda (\theta_2 - \theta_1)^{-\frac{3}{2}}, \quad (5.3)$$

with θ_1 and θ_2 defined as a positive scattering angle expressed in degree angle and λ the wavelength in metre. The fringe spacing $(\theta_2 - \theta_1)$ has to be deduced from the Airy rainbow after the ripple structure has been filtered out.

Once D_{Airy} has been determined, one can, in principle, obtain the real part of the refractive index from any Airy fringe (Fig. 5.5). For the rainbow technique, the first fringe at θ_1 is applied because it compares best with the Lorenz-Mie computations (Sec. 4.3). θ_1 follows again from Eq. 4.20 and table 4.1:

$$\theta_1 = |\theta_{rg}| + \frac{1.08728}{\sin \tau_{rg}} \left(\frac{\lambda^2 \cos \tau_{rg}}{16D^2} \right)^{\frac{1}{3}} \frac{180^\circ}{\pi}, \quad (5.4)$$

and reduces for $m = 4/3$ to

$$\theta_1 = |\theta_{rg}| + 46.18 \left(\frac{\lambda}{D} \right)^{\frac{2}{3}}. \quad (5.5)$$

The dependency on the refractive index lies thus mainly in the geometric rainbow angle θ_{rg} (Eq. 4.5). It is solved implicitly from this expression. The temperature is then derived from the empirical relationship between m and T , P and λ , as was established by Thormählen et al.[67].

Already in 1991, Roth et al.[60] applied an algorithm based on Eq. 5.4 to measure the droplet temperature. The knowledge needed about the diameter was measured from the fringes which are visible in the forward-scattered light, hence requiring two detectors. In the present section, it has been shown that it is possible to deduce the size information from fringes which are visible in the rainbow itself, thus needing only one detector. Moreover, the fringe spacing does not depend on the temperature so that the size can be measured without preliminary knowledge of the droplet temperature. This approach has been utilized by Van Beeck and Riethmüller[72, 71] and later by Sankar et al.[62] in their “Rainbow Refractometer System”. As such, it has been shown that it is possible from one primary rainbow signal to simultaneously derive the size and temperature of a single droplet. However, one has to realize that by using the Airy theory, the error in temperature grows larger than 1°C for $T < 20^\circ\text{C}$ and $D < 100\ \mu\text{m}$ in the case of water droplets at ambient temperature, as can be derived from the results in Sec. 4.3. From the same section, it is found that the uncertainty in the Airy diameter exceeds 3% for droplets smaller than $100\ \mu\text{m}$.

5.2.1 Ripple structure

In the experimental signal of Fig. 5.2, the ripple structure superimposed on the Airy fringes can be clearly identified as well as the corresponding peaks related to the angular frequencies F_2 and F_3 . It is obvious to believe that these frequencies can be related to the droplet diameter as well.

The ripple structure results from interference between internal and external reflection. Because the latter is not included in the Airy theory, it does not appear in the Airy rainbow pattern. Yet, the frequencies F_2 and F_3 have already been discussed in Sec. 1.3 of the Introduction. They can be obtained from an analysis which is similar to Young’s double-slit experiment:

$$F_3 = F_2 + F_1. \quad (5.6)$$

From Young’s experiment it follows that the angular frequency F_1 equals the distance between the two interfering internally-reflected rays, divided by the wavelength λ (Fig. 5.6). This distance is zero at the geometric rainbow angle θ_{rg} , leading to

$$F_1|_{\theta_{rg}} = 0. \quad (5.7)$$

For this condition, F_2 and F_3 are the same and are defined as the ripple frequency F_{ripple} :

$$F_{\text{ripple}} \equiv F_2|_{\theta_{rg}} = F_3|_{\theta_{rg}}. \quad (5.8)$$

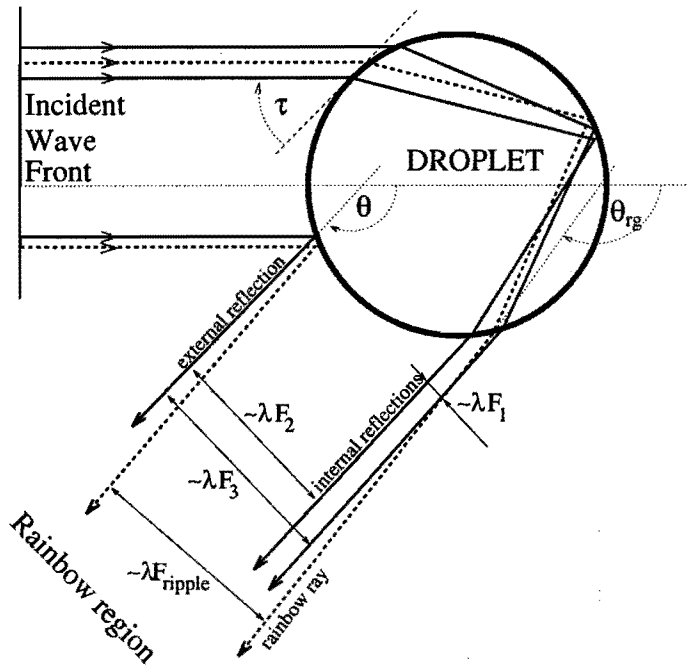


Figure 5.6: Explanation of ripple frequency F_{ripple} as the frequency of the rainbow interference pattern that results from interference between the geometrical rainbow ray at θ_{rg} and external reflection. F_{ripple} splits up in F_2 and F_3 for $|\theta| > |\theta_{rg}|$.

The analogy with Young's fringe analysis dictates that the ripple frequency can be found from the distance between the geometric rainbow ray at θ_{rg} and the externally-reflected ray at infinity (see Fig. 5.6 and Van Beeck and Riethmuller[70]):

$$F_{ripple} = \frac{D}{2\lambda} (\cos \tau_{rg} + \cos \frac{\theta_{rg}}{2}) \frac{\pi}{180^\circ}. \quad (5.9)$$

τ_{rg} and θ_{rg} are given in Eqs. 4.4 and 4.5. F_{ripple} can be determined experimentally from the power spectrum of a rainbow pattern. However, because this spectrum results from the Fourier transform over a finite range of scattering angles near θ_{rg} , the peak at F_{ripple} will split in two peaks at angular frequencies F_2 and F_3 , differing F_1 . If the interval of scattering angles covers two Airy fringes, then F_1 approaches the Airy frequency F_{Airy} , defined as

$$F_{Airy} \equiv \frac{1}{(\theta_2 - \theta_1)}. \quad (5.10)$$

Subsequently, F_2 and F_3 hold

$$F_2 = F_{ripple} - (1 - \alpha)F_{Airy} = F_{ripple} - \frac{1}{2}F_{Airy}, \quad (5.11)$$

$$F_3 = F_{ripple} + \alpha F_{Airy} = F_{ripple} + \frac{1}{2}F_{Airy}, \quad (5.12)$$

where the coefficient α was put quite arbitrarily at $\frac{1}{2}$. The validity of Eq. 5.12 has been checked by comparing it with Lorenz-Mie computations (see Van Beeck and Riethmuller[70]). The results are shown in Fig. 5.7, depicting F_3 as a function of the droplet diameter for $\lambda = 514.5 \text{ nm}$. The difference between both computations never exceeds 1% as long as $D > 100 \mu\text{m}$. This means that Eq. 5.12 expresses an accurate, almost linear, relationship between the droplet diameter and F_3 ¹.

Following the above analysis, one can state that it is possible to measure the droplet size from the ripple structure visible in the rainbow pattern. The resulting diameter is called the ripple diameter D_{ripple} . It can be demonstrated that no exact preliminary knowledge of droplet temperature is required, similarly to the size measurement from the Airy fringes. For $m = 4/3$, the relationship between F_3 and D_{ripple} reduces

$$F_3 = 0.01064 \frac{D_{\text{ripple}}}{\lambda} + 0.004947 \left(\frac{D_{\text{ripple}}}{\lambda} \right)^{2/3}, \tag{5.13}$$

from which the ripple diameter has to be solved implicitly.

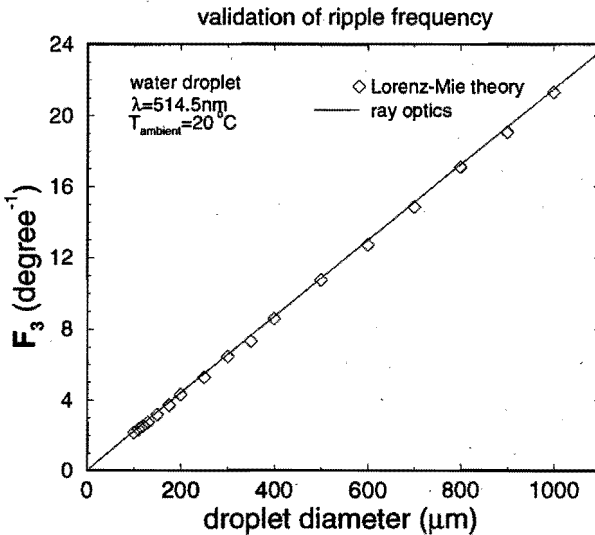


Figure 5.7: The angular frequency F_3 according to Eq. 5.12 and the Lorenz-Mie theory as a function of the droplet diameter for $m = 1.33$ and $\lambda = 514.5 \text{ nm}$.

¹Anders et al.[5] studied the ripple frequency in the micrometre range. The authors successfully established a numerical fit based on Lorenz-Mie computations.

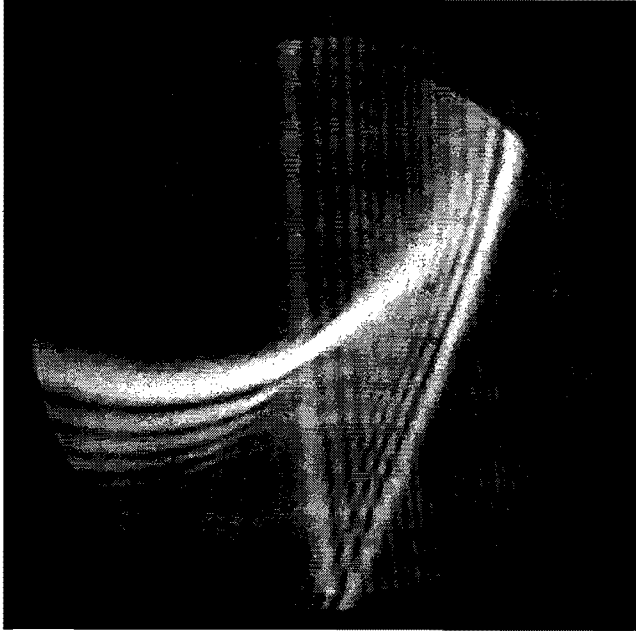


Figure 5.8: *Severely distorted Airy fringes. An intrusion of a cusp-shaped secondary rainbow into the primary rainbow region can be observed. The picture was taken by a camera, focused at infinity, pointed at a hanging tear-shaped drop.*

5.3 Non-sphericity detection

5.3.1 Non-circular rainbows

The Airy theory is valid for spherical particles. Clift et al.[11] have empirically investigated the shape of a free-falling droplet. They observed that the shape is clearly non-spherical and approaches that of an oblate. From an equivalent sphere diameter of 1 mm to 4 mm, the ratio between the axis diameters increases from 1.03 to 1.30. Unfortunately, the rainbow strongly depends on the shape of the droplet. Marston[43] published in 1980 a study on the changes in the rainbow pattern produced by acoustically deformed droplets. He reported a shift of the rainbow as was already predicted theoretically in 1910 by Moebius[49]. However, the impact of drop non-sphericity on individual interference structures remained unclear. This was studied in Chap. 3 by applying Kirchhoff's theory to an ellipsoidal droplet. The preliminary results show that the percent change in ripple frequency is different from that of the Airy frequency. Moreover, this feature seems to depend on the equivalent sphere diameter.

Fig. 5.8 shows a severely distorted rainbow-interference structure. The structure reveals an intrusion of a cusp caustic (see for example Lock and Andrews[38]

or Berry[8]), probably related to the secondary rainbow, into the primary rainbow region. The pattern is created by a large pendant tear-shaped drop. The optical axis of the photo-camera lies in the horizontal plane containing the drop and the laser beam. The camera is focused at infinity to obtain the far-field scattered-light intensity. The picture demonstrates that the rainbow pattern can exhibit more than just a shift or change in frequency as a result of non-sphericity. This was also pointed out at the end of Chap. 3. The preliminary results of Chap. 3 and pictures such as in Fig. 5.8 make it clear that obtaining physical quantities from non-spherical drops by means of rainbow interferometry is not obvious. At this stage, it is better simply to reject rainbows produced by non-spherical particles, which implies the need for some form of detection.

5.3.2 Selection of spherical droplets

The detection of non-sphericity in drops is based on the comparison of the Airy diameter D_{Airy} and the ripple diameter D_{ripple} (see Van Beeck and Riethmuller[70, 74]). In Sec. 5.2, it was explained that these diameters can be derived independently from the Airy fringes and the ripple structure using theories only valid for spheres. Therefore, one can expect that D_{Airy} equals D_{ripple} when the droplet is spherical. In that case, a reliable temperature measurement can be made using the Airy theory (see Eq. 5.4). In case of inequality in the diameters, the rainbow pattern is rejected. This non-sphericity detection method is based on the fact that the optical interference structures employed originate from different local curvatures of the droplet surface. The preliminary results of Chap. 3 endorse this principle for ellipsoids.

5.4 Dynamic calibration procedure for the rainbow technique

The rainbow receiver meets the requirement for the high accuracy concerning the resolution in the scattering angle with respect to the optical axis of the receiving optics (Fig. 5.1). However, to determine the temperature, the scattering angle with respect to the laser beam has to be known. Because with the present set-up an accurate enough geometrical measurement of this angle cannot be obtained, a dynamic calibration procedure has to be performed in order to find the reference angle θ_{ref} and the reference position at the linear CCD array, i.e. y_{ref} (Eq. 5.1). Therefore, a rainbow pattern coming from a transparent spherical particle with known refractive index has to be recorded. To this end, one applies the non-sphericity detection method, described in the previous section, to a rainbow signal acquired at isothermal conditions; the signal can be utilized for calibration provided the difference between ripple and Airy diameter is smaller than the uncertainty of $\sim 2\%$ in the size-measurement. In that case, the reference position y_{ref}

is assigned to the position at the CCD array at which the main rainbow maximum was recorded. The corresponding reference angle is then computed by Eq. 5.4.

5.5 Experimental results

Basic experiments have been carried out to check the non-sphericity detection method. The experimental setup has been discussed in Sec. 5.1. Fig. 5.9 shows a recorded signal. D_{Airy} is derived with the help of the Airy theory from the difference between the main rainbow maximum and the first supernumerary bow. D_{ripple} comes from the properly identified peak in the spectrum of the signal (Fig. 5.10). D_{Airy} equals D_{ripple} , so the droplet is spherical; as expected, the temperature derived from the main maximum is the same as the ambient temperature. Another rainbow is presented in Fig. 5.11 with its spectrum in Fig. 5.12. Here, D_{Airy} differs from D_{ripple} by almost $50\mu m$, indicating that the droplet is non-spherical. The temperature derived from the rainbow is about $6^\circ C$ from ambient. Several signals of this type have been analyzed, revealing that the difference $\left| \frac{D_{Airy} - D_{ripple}}{D_{Airy}} \right|$ has to be less than $\frac{5}{100}$ in order to ensure an accuracy of $5^\circ C$ in the droplet temperature. This accuracy is expected to be higher for heated water droplets because for $T > 20^\circ C$, θ_1 reveals a stronger dependency on the temperature, as shown in Fig. 5.5.

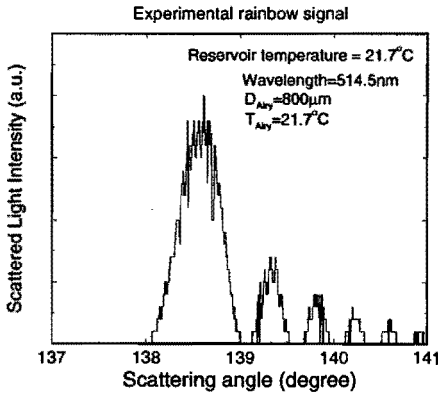


Figure 5.9: Rainbow signal coming from a droplet that is spherical, i.e., the droplet diameter D_{Airy} , derived from the distance between the first two Airy fringes, equal to diameter D_{ripple} that is derived from the ripple structure.

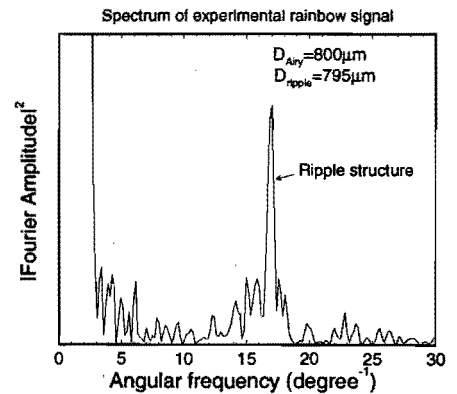


Figure 5.10: Magnitude squared of the Fourier transform of the rainbow in Fig. 5.9.

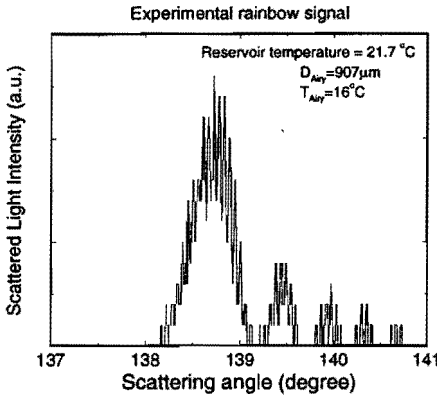


Figure 5.11: Rainbow signal coming from a non-spherical droplet, i.e., the droplet diameter D_{Airy} unequal to D_{ripple} .

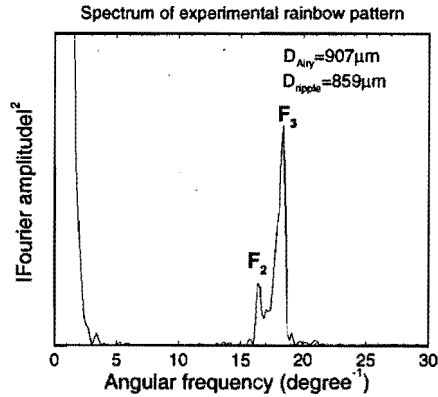


Figure 5.12: Magnitude squared of the Fourier transform of the rainbow depicted in Fig. 5.11.

These quantitative results are different from the preliminary results of Figs. 3.24 and 3.25 in Chap. 3. There, a rainbow pattern was computed for an ellipsoid with a non-sphericity of 3%. Applying the formulas in Sec. 5.2 would yield $\left| \frac{D_{Airy} - D_{ripple}}{D_{Airy}} \right| \approx \frac{5}{100}$ and the shift of the main rainbow maximum would correspond to a temperature difference of more than 100 °C and not 5 °C as in the experiments. Further computations should clarify this contradiction. However, in order to perform a more valid comparison between theory and practice, it is essential that the shape of the droplet is known, or better, can be controlled. For this, it is suggested to record at the same time the rainbow pattern and the image of the droplet that is for instance optically or acoustically levitated.

5.6 Rainbow patterns without ripple structure

The non-sphericity detection method works, although its high accuracy is not yet understood. Sankar et al.[62] used a similar method to detect non-sphericity in drops. It was based on the comparison between the Airy diameter D_{Airy} and the diameter provided by the phase-Doppler system. The reason for not using the ripple diameter D_{ripple} was that for oscillating or evaporating droplets, the ripple structure can be completely damped out due to the finite integration time of the linear CCD camera. This was already predicted by Roth et al.[61]. Fig. 5.13 shows a rainbow pattern without ripple structure. The exact cause can only be traced by recording the (change in) shape of the droplet during the integration time of the CCD camera. But in any case, signals without ripple structure have to be rejected

if the rainbow technique is used as stand-alone apparatus. In the next chapter a solution to this problem will be proposed.

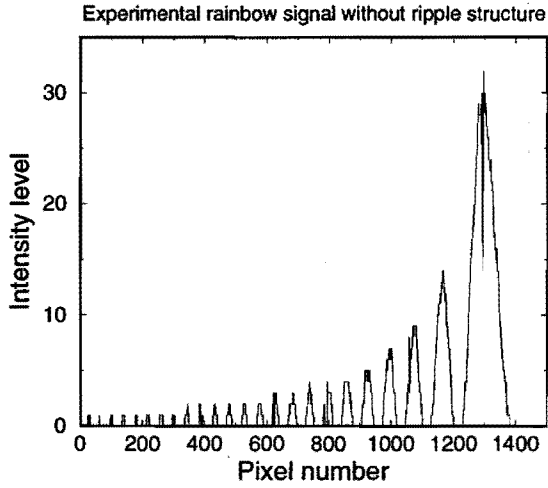


Figure 5.13: *Experimental rainbow pattern recorded by the linear CCD camera. No ripple structure is superimposed on the numerous Airy fringes.*

Chapter 6

RAINBOW INTERFEROMETRY WITH WIRE DIFFRACTION

In Chap. 5, a rainbow technique was presented for simultaneous measurement of droplet size and temperature. Here, a technique is discussed that in addition to these scalar quantities measures one velocity component of individual droplets in a water spray. The technique is based on rainbow interferometry in combination with diffraction by a wire, placed in the spatial filter of the scattered-light detector (Sec. 6.1 and Van Beeck and Riethmuller[73, 76]). A photomultiplier detects the wire-diffraction pattern superimposed on the rainbow interference pattern created by a droplet scattering laser-light. The velocity is determined from the equivalent geometric wire shadow. The necessary sphericity validation is performed by comparing the Airy and the ripple droplet diameters, resulting from the respective interference structures. The temperature is recovered from the relative position of the wire diffraction pattern to the main rainbow maximum (Sec. 6.2). The technique has been applied to a water spray at ambient temperature (Sec. 6.3). The results show the importance of non-sphericity detection. A discussion on transient events concludes the chapter.

6.1 Photomultiplier set-up for detection of the rainbow in a spray

In Sec. 5.6, it was seen that the finite integration time of the CCD camera causes the ripple structure sometimes to disappear. This problem is overcome by using a photomultiplier instead (see Refs. [74, 75]). Moreover, a photomultiplier has the advantage of being more sensitive to the scattered-light intensity than a linear CCD array.

Fig. 6.1 demonstrates the principle of the detection of a rainbow pattern by means of a photomultiplier placed in front of a pin hole. When the droplet is situated in the laser beam, the fringes, visible in the rainbow, appear on concentric cones with the droplet as apex and the axes parallel to the laser beam. These cones

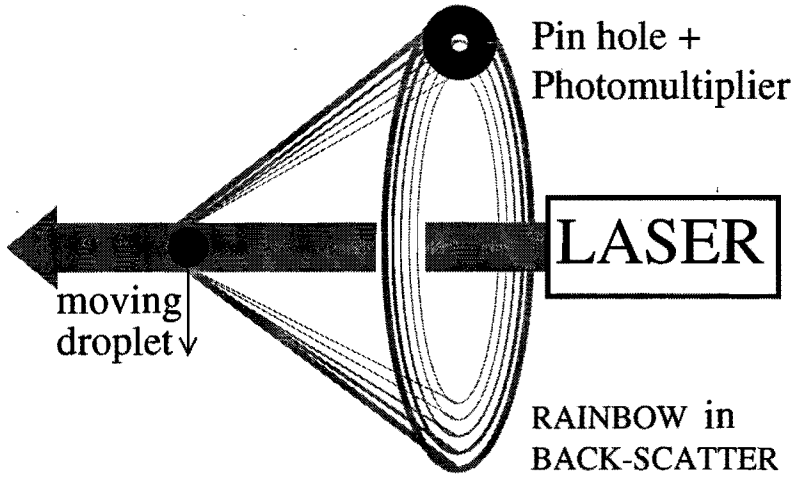


Figure 6.1: The principle of the detection of a time-varying rainbow interference-pattern by means of a photomultiplier placed behind a pin hole. The rainbow fringes move in front of the pin hole when the droplet passes the laser beam.

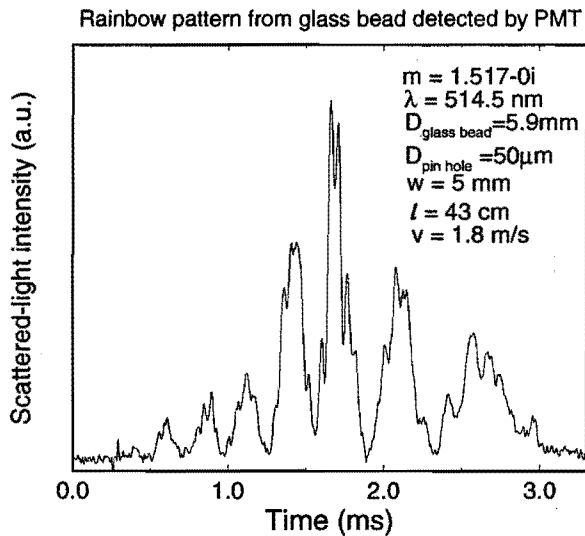


Figure 6.2: Experimental rainbow pattern detected by the photomultiplier set-up, depicted in Fig. 6.1. The scattering particle was a spherical glass bead ($D = 5.9 \text{ mm}$) that crossed the laser beam (beam diameter $w = 5 \text{ mm}$) with velocity $v = 1.8 \text{ m/s}$ at a distance of $l = 43 \text{ cm}$ from the pin hole.

move in front of the pin hole when the droplet traverses the laser beam. In this way, a time-varying rainbow signal is detected. Fig. 6.2 shows an experimental rainbow pattern coming from a spherical glass bead. It gives an illustration of the principle of detection by a photomultiplier. The experimental set-up was based on the sketch in Fig. 6.1.

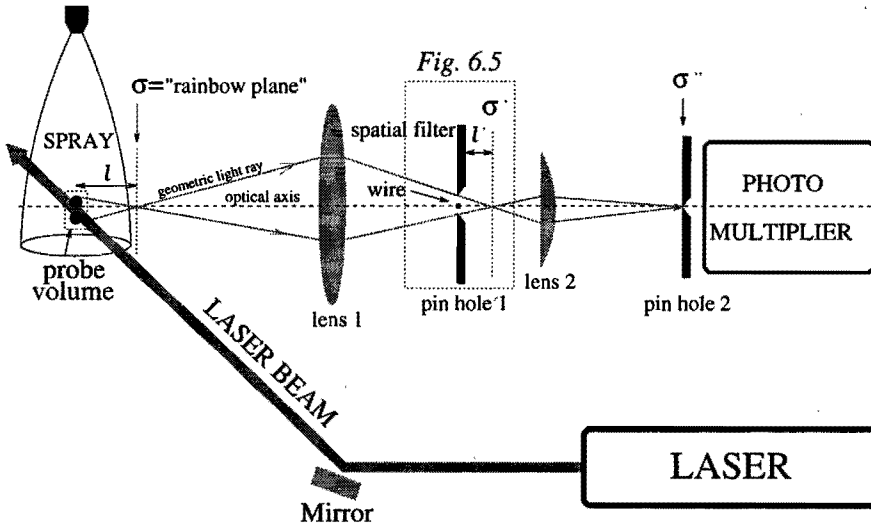


Figure 6.3: The photomultiplier set-up for detection of a rainbow pattern in a spray. The polarization is perpendicular to the (vertical) scattering plane which is formed by the laser beam and the optical axis of the rainbow detector. A wire is placed in pin hole 1 perpendicularly to this scattering plane in order to find a reference position of the droplet in the laser beam.

In a spray, several droplets cross the laser beam at the same time. In order to detect a rainbow coming from one single droplet, a probe volume has to be selected by means of a spatial filter that is placed in front of the photomultiplier as depicted in Fig. 6.3. The virtual measurement plane σ is positioned very close to the probe volume with the help of lens 2; this is to ensure a detection of a sufficiently large range of scattering angles around the main rainbow maximum so that at least two Airy fringes are observed.

At the centre of pin hole 1, a wire is fixed perpendicularly to the scattering plane. When the image of the droplet passes the wire, the light intensity detected by the photomultiplier is expected to fall to zero. In this way, a reference position of the droplet in the laser beam is found which serves to relate each moment in the time-varying rainbow signal to an absolute scattering angle. This information is needed to obtain the droplet temperature from the rainbow, as will be explained in Sec. 6.2.

Fig. 6.4 shows a simulation of the photomultiplier signal for a refractive index

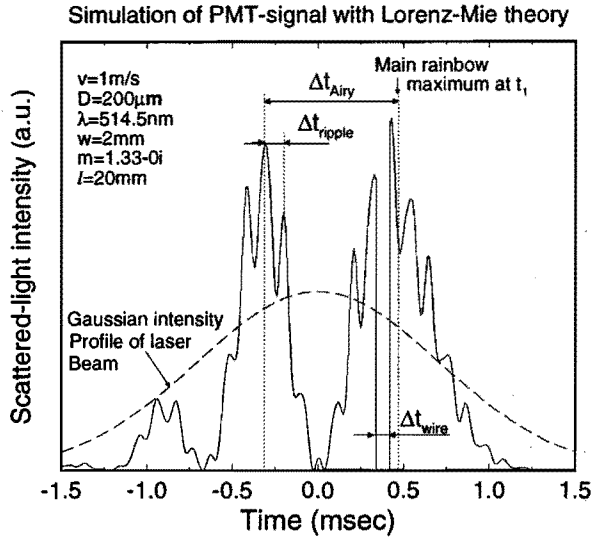


Figure 6.4: Simulation of the photomultiplier signal (using the extension of the Lorenz-Mie theory, as described in Sec. 2.5) for the set-up depicted in Fig. 6.3. A water droplet having a diameter of $200\ \mu\text{m}$, a velocity of $1\ \text{m/s}$ and a refractive index of $m = 1.33 - 0i$ was used. The impact of the wire diffraction is modeled as a geometric shadow.

$m = 1.33 - 0i$ and a droplet diameter $D = 200\ \mu\text{m}$, concerning the experimental set-up of Fig. 6.3. The Lorenz-Mie theory was employed, using the method described in Sec. 2.5. The droplet velocity is $v = 1\ \text{m/s}$ and the beam diameter measures $w = 2\ \text{mm}$. The distance between the probe volume and the virtual measurement plane σ is $20\ \text{mm}$. The rainbow pattern is modulated by the Gaussian intensity profile of the laser beam but apart from that it reveals the same optical interference structures as identified in Fig. 1.12; Δt_{Airy} denotes the time interval between two Airy fringes and Δt_{ripple} is related to the ripple structure. The influence of the wire on the rainbow is modeled as a geometric shadow. In this case, the velocity of the droplet would simply be given by

$$v = \frac{D_{\text{wire}}}{\Delta t_{\text{wire}}} \frac{1}{M}, \quad (6.1)$$

where M is the magnification factor and Δt_{wire} the time it takes the image of the droplet to pass the wire with diameter D_{wire} . This idea refers to Fiedler et al.[18] who used the shadow of a grating-like structure to determine the particle velocity. Similarly to that method, the accuracy of relationship (6.1) is determined by the diffraction induced by the wire which will be discussed in the following subsection.

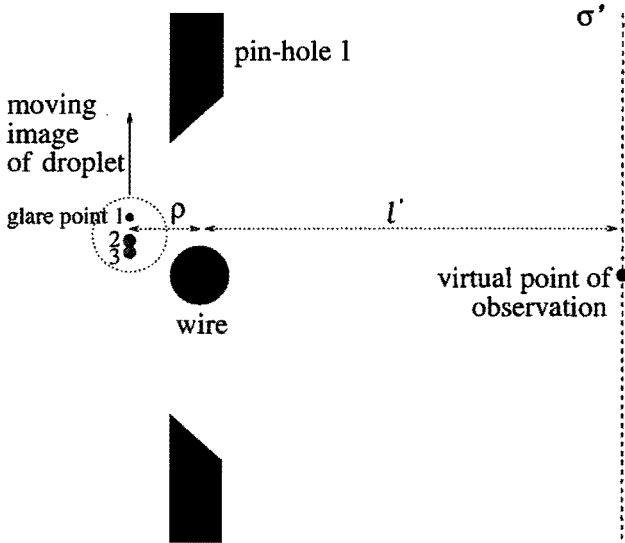


Figure 6.5: *The scattering problem to be considered in order to describe the effect of wire diffraction on the rainbow pattern concerning the set-up of Fig. 6.3.*

6.1.1 The effect of wire diffraction on the rainbow pattern

To gain proper insight into the influence of the wire diffraction on the rainbow pattern, the photomultiplier set-up in Fig. 6.3 has to be carefully considered. Fig. 6.5 shows a simplification of the wire diffraction problem. ρ is the distance between the light source and the diffracting object, i.e. the wire, whereas l' denotes the distance between the wire and the virtual observation plane σ' . Although this plane is placed in the far-field region for the rainbow pattern, the wire diffraction cannot be described by Fraunhofer diffraction. The reason for this is that the incident light is not a plane wave because the imaging lens 1 of the spatial filter (see Fig. 6.3) creates an image of the light source, i.e. the droplet, ideally at the position of the wire. Consequently, we are dealing with Fresnel diffraction (see Hecht[30]).

It is important to recognize that the image of the droplet consists mainly of three glare points which form the origin of the rainbow (see Sec. 1.3, Van Beeck and Riethmuller[74] or Van de Hulst and Wang[84]). External reflection forms glare point 1 but for the diffraction problem its light intensity will be neglected in comparison with the two closely-positioned spots 2 and 3 coming from internally-reflected rays (Fig. 3.8). As these two rays have scattering angles around the geometrical rainbow angle θ_{rg} , the corresponding glare points 2 and 3 merge to one bright spot. As long as the size of this spot is smaller than the wire diameter, a deep shadow is to be expected when this single spot passes the obstacle. However, when the spot touches the edge of the wire, a diffraction pattern is generated. In

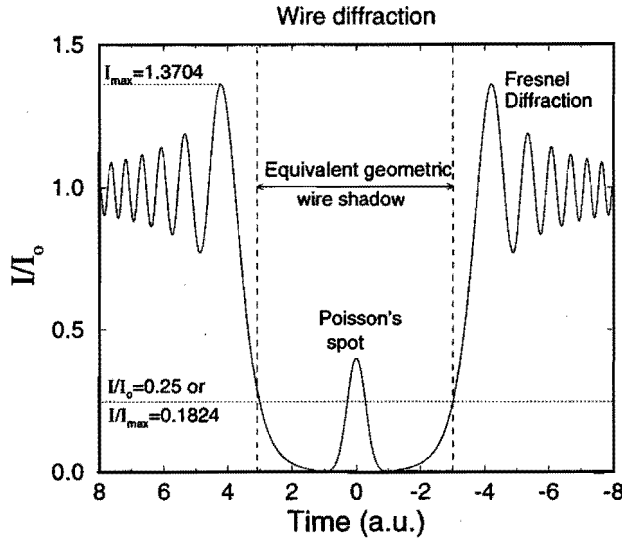


Figure 6.6: *Heuristic model of the wire diffraction pattern at the point of observation in Fig. 6.5.*

the scattering plane, this pattern is assumed to be similar to the Fresnel diffraction pattern of a straight edge illuminated by a cylindrical wave front (Fig. 6.6) provided that the following condition is fulfilled (Hecht[30]):

$$D_{wire} \left[\frac{2(l' + \rho)}{\lambda l' \rho} \right]^{\frac{1}{2}} > 10. \quad (6.2)$$

Here λ denotes the wavelength of the light and D_{wire} , ρ and l' correspond to the dimensions given above. When the image of the droplet is well positioned near the wire, that is to say when ρ is about $D_{wire}/2$, the condition is satisfied if $D_{wire} > 25\lambda$. Then, the width of the geometric wire shadow can be related to the time duration between signal intensities $I/I_0 = 0.25$, or with respect to the maximum signal intensity $I/I_{max} = 0.1824$, as shown in Fig. 6.6.

Fig. 6.7 shows an experimental rainbow pattern, recorded using the set-up of Fig. 6.3. The droplet image passed the wire between $200 \mu s < t < 220 \mu s$. The resulting wire diffraction structure is not symmetric due to interference with the rainbow pattern. Each edge reveals a maximum, denoted by $I_{max,1}$ and $I_{max,2}$, which corresponds to the main maximum in the Fresnel pattern. Supernumerary Fresnel maxima are not clearly observed because of interference with the ripple structure. Following the heuristic explanation of the wire diffraction in Fig. 6.6, it

is assumed that the droplet image touches the borders of the wire when¹

$$\frac{I - I_{min,i}}{I_{max,i} - I_{min,i}} = 0.1824 \quad \text{with } i=1,2. \quad (6.3)$$

As a result, the time interval τ_{wire} is found, that corresponds to the time it takes for the geometric wire shadow to pass in front of the photomultiplier. Subsequently, Eq. 6.1 can successfully be applied to determine the droplet velocity if one knows the wire diameter D_{wire} and the magnification factor M .

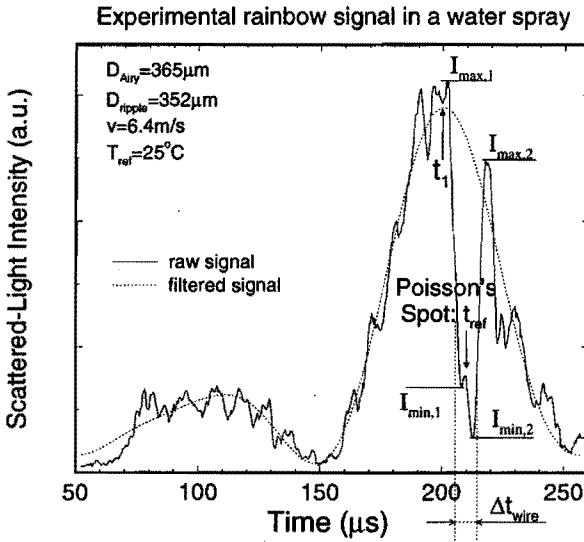


Figure 6.7: The calibration rainbow pattern recorded by the photomultiplier in the set-up of Fig. 6.3. The dip in the rainbow pattern at $200 \mu s < t < 220 \mu s$ results from the passage of the image of the droplet across the wire. The edges of this shadow reveal the Fresnel diffraction of Fig. 6.6. The width, Δt_{wire} , is related to the droplet velocity as explained in Subsec. 6.1.1. The centre of the wire shadow reveals the Poisson spot which is connected to a certain reference scattering angle.

A remarkable feature in the dip of Fig. 6.7 is that at its centre, i.e. at time $t = 210 \mu s$, there appears to be a small peak. This phenomenon is believed to be analogous to the Poisson spot which is always visible at the centre of the shadow behind an illuminated circular opaque object (Ref. [30]). Therefore, the maximum of this peak corresponds exactly to the moment that the glare point is at the centre of the wire. A reference scattering angle will be assigned to the Poisson spot which is employed for the temperature measurement.

¹Note that $I_{min,1}$ and $I_{min,2}$ had to be introduced because total obscurity was not entirely obtained. The validity of the factor 0.1824 in Eq. 6.3 has therefore still to be examined.

6.2 Determination of droplet velocity, size and temperature

In this section, the algorithm to process the rainbow photomultiplier-signal is presented. It is based on the determination of one velocity component from the time Δt_{wire} as suggested in the previous section. The component measured is the one perpendicular to the optical axis of the rainbow receiver. The advantage of this velocity measurement, described by Eq. 6.1, is its independence of the droplet shape and temperature. This advantage can hardly be overestimated, especially when dealing with arbitrarily oriented spheroids.

Velocity v of the droplet is related to the Airy frequency $1/\Delta t_{Airy}$ (see Fig. 6.4) as explained by Van Beeck and Riethmuller[74]:

$$v = -l \frac{d\theta}{dt} \frac{\pi}{180^\circ} = 1.777 \frac{l}{\Delta t_{Airy}} \left(\frac{\lambda}{D}\right)^{\frac{2}{3}}. \quad (6.4)$$

The relationship between the ripple frequency $1/\Delta t_{ripple}$ and the droplet velocity is given by the following expression, where Δt_{ripple} is deduced from the corresponding peak in the power spectrum (Refs. [70, 74]):

$$v = -l \frac{d\theta}{dt} \frac{\pi}{180^\circ} = \frac{l}{\Delta t_{ripple}} \frac{1}{0.613(D/\lambda) + 0.281(D/\lambda)^{2/3}}. \quad (6.5)$$

The constants are valid for a real refractive index of $m = 4/3$. From Eq. 6.4, an Airy diameter D_{Airy} can be deduced whereas Eq. 6.5 yields a ripple diameter D_{ripple} . As v does not depend on the droplet non-sphericity, but Δt_{Airy} and Δt_{ripple} do, the diameter comparison will allow the detection of non-sphericity in the same way as the non-sphericity detection method for the CCD camera set-up, described in Sec. 5.3.

When the droplet is identified as being spherical, a reliable temperature can be derived from the angular position of the main rainbow maximum. Because the photomultiplier provides a time-varying signal, each moment has to be related to a certain absolute scattering angle. The relative scattering angle is found from Eq. 6.4:

$$\frac{d\theta}{dt} = -\frac{v}{l} \frac{180^\circ}{\pi}. \quad (6.6)$$

Integration over the time interval $t - t_{ref}$ yields the required absolute scattering angle

$$\theta = \theta_{ref} - (t - t_{ref}) \frac{v}{l} \frac{180^\circ}{\pi}, \quad (6.7)$$

where θ_{ref} is a reference scattering angle at the time $t = t_{ref}$. The reference time is taken to be at the Poisson spot (Fig. 6.6). The spot is related to a fixed position of the droplet in the laser beam thus to a certain reference scattering angle θ_{ref} .

To find the relationship between θ_{ref} and t_{ref} , the Airy theory has to be applied to a calibration rainbow coming from a spherical particle with known refractive index (see Van Beeck and Riethmuller[71, 72]):

$$\theta_{ref} = |\theta_{rg}| + \left(\frac{1.08728}{\sin \tau_{rg}} \left(\frac{\lambda^2 \cos \tau_{rg}}{16D^2} \right)^{1/3} + (t_1 - t_{ref}) \frac{v}{l} \right) \frac{180^\circ}{\pi}. \quad (6.8)$$

Time t_1 corresponds to the position of the main rainbow maximum. This can be found accurately by filtering the ripple structure and the wire shadow out of the rainbow signal, as shown in Fig. 6.7. The geometrical rainbow angles θ_{rg} and τ_{rg} were already given in Eqs. 4.4 and 4.5:

$$\theta_{rg} = 2\tau_{rg} - 4 \arccos \left(\frac{1}{m} \cos \tau_{rg} \right), \quad (6.9)$$

$$\sin \tau_{rg} = \sqrt{\frac{m^2 - 1}{3}}. \quad (6.10)$$

Once the reference angle has been established, the refractive index, thus the temperature, of any rainbow signal can be measured. Therefore, time t_1 has to be determined and then Eqs. 6.8, 6.9 and 6.10 have to be solved implicitly for the refractive index.

6.3 Experimental results in a water spray

The method described in the previous section to determine droplet velocity, size and temperature has been applied to individual droplets in a liquid spray. The experimental set-up is based on the sketch in Fig. 6.3. A “full-cone” water spray is directed downwards and is produced by the nozzle “UniJet TG03” of *Spraying Systems Co.* The water pressure applied is 2.5 bar and measurements are taken in the centre of the spray, 20 cm below the nozzle exit. The droplets are assumed to be at ambient temperature because the water is not heated. The Ar-ion laser is operated at a power of 500 mW and a wavelength of 514.5 nm. No beam expander is utilized. The laser beam and optical axis of the scattered-light detector form a vertical scattering plane. The detector, or rainbow receiver, is positioned horizontally to ensure the measurement of the main velocity component of the droplets. Pin hole 1 of the receiver measures 2 mm and the wire, placed at the centre of the pin hole, has a diameter of 50 μm . Pin hole 2 in front of the photomultiplier is no larger than 50 μm to prevent integration over the ripple structure. The distance l between the probe volume and the virtual plane of observation σ measures 25.8 mm. The rainbow signal is 8-bit digitized by using a digital oscilloscope, *Tektronix 2430*, as a transient recorder. A signal consists of 1024 samples taken at a sampling frequency of 2.5 MHz. With the aid of an IEEE interface, the stored waveform is transferred to a personal computer.

A dynamic calibration had to be performed in order to relate the centre of the wire shadow, i.e. the Poisson spot, to an absolute reference angle θ_{ref} as explained

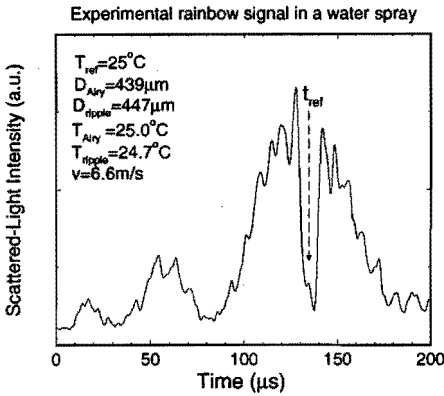


Figure 6.8: An experimental rainbow pattern recorded by the photomultiplier in the set-up of Fig. 6.3. This signal passes the sphericity check because the difference between the Airy and ripple diameter is smaller than the measurement uncertainty.

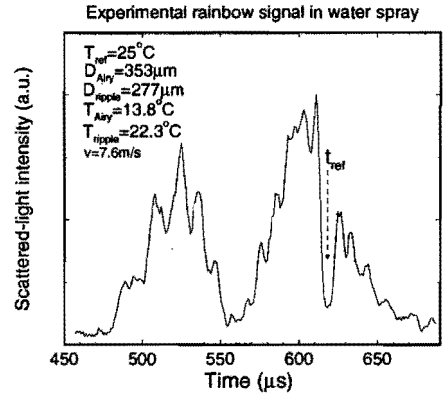


Figure 6.9: An experimental rainbow pattern recorded by the photomultiplier in the set-up of Fig. 6.3. The droplet is non-spherical, thus the signal is rejected.

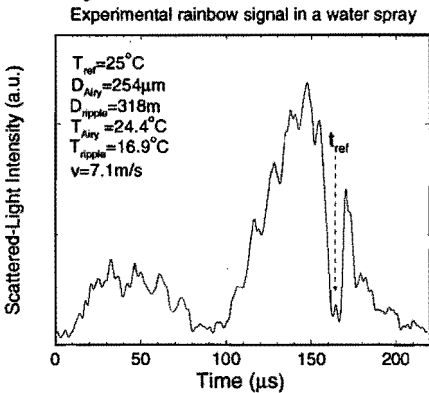


Figure 6.10: An experimental rainbow pattern recorded by the photomultiplier in the set-up of Fig. 6.3. Although the temperature based on the Airy diameter is close to the reference temperature, the signal is rejected because of the large difference between both diameters.

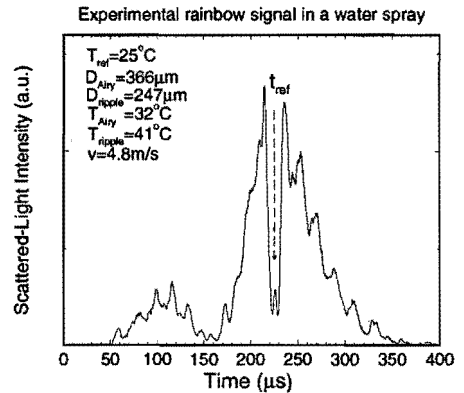


Figure 6.11: An experimental rainbow pattern recorded by the photomultiplier in the set-up of Fig. 6.3. Exceptionally, the sampling frequency was 1 MHz instead of 2.5 MHz. The signal is rejected.

Signal	v [m/s]	D_{Airy} [μm]	D_{ripple} [μm]	ΔD [μm]	T_{Airy} [$^{\circ}\text{C}$]	T_{ripple} [$^{\circ}\text{C}$]	ΔT [$^{\circ}\text{C}$]
Fig. 6.7	6.4	365	352	13	$T_{ref} = 25$	$T_{ref} = 25$	0
Fig. 6.8	6.6	439	447	-8	25.0	24.7	0.3
Fig. 6.9	7.6	353	277	76	13.7	22.3	-8.6
Fig. 6.10	7.1	254	318	-64	24.4	16.9	7.5
Fig. 6.11	4.8	366	247	119	32.4	41.4	-9.0

Table 6.1: *Experimental results obtained from rainbow-interferometric measurements of different droplets at a fixed position in a water spray.*

in Sec. 6.2. Therefore, a rainbow pattern coming from a spherical droplet in the water spray at ambient temperature was recorded for which the Airy diameter, obtained from Eq. 6.4, agrees with the ripple diameter (Eq. 6.5) within the measurement uncertainty of $\pm 20 \mu\text{m}$. This was the case for the signal depicted in Fig. 6.7. Its velocity, deduced from the dip caused by the shadow of the wire projected on pin hole 2, was found to be $6.4 \pm 0.4 \text{ m/s}$. The droplet diameters deduced were $D_{Airy} = 365 \mu\text{m}$ and $D_{ripple} = 352 \mu\text{m}$. The reference temperature assigned to this calibration pattern equaled 25°C , i.e. the ambient temperature. The resulting reference angle, corresponding to the centre of the dip, was computed with the help of Eqs. 6.8, 6.9 and 6.10; $\theta_{ref} = 138.636^{\circ}$. Based on this information, Table 6.1 has been drawn up which lists the velocity v , the diameters D_{Airy} and D_{ripple} and the difference $\Delta D = D_{Airy} - D_{ripple}$ for four individual droplets at the same position in the water spray. The corresponding signals are depicted in Fig. 6.8, 6.9, 6.10 and 6.11. The listed temperatures T_{Airy} and T_{ripple} are computed using the Airy and ripple diameters, respectively. The uncertainties in the determination of size and velocity limits the precision in the temperature measurement to $\pm 3^{\circ}\text{C}$. From the four signals only the one depicted in Fig. 6.8 passes the non-sphericity detection method; ΔD is $-8 \mu\text{m}$ and the difference $\Delta T = T_{Airy} - T_{ripple}$ equals 0.3°C which is smaller than the measurement uncertainty. Although ΔT approaches zero when ΔD does, it is premature to extract a characteristic correlation between ΔD and ΔT from the different values in Table 6.1. To find this correlation, a larger number of data will have to be evaluated in the future.

6.4 Transient events

Since the water spray utilized for the experiments in Sec. 6.3 was employed at ambient conditions, no internal temperature gradients were present. Consequently, this phenomenon did not influence the accuracy of the measurements. However, it should be mentioned that at non-ambient conditions, large deformations of the rainbow pattern can occur as reported by Anders et al.[6] and Corbin et al.[12].

Investigating whether a droplet-size comparison method can deal with this situation is suggested. Without internal temperature gradients, the influence of the droplet non-sphericity on the rainbow pattern can successfully be circumvented by selecting spherical droplets which is achieved by comparing the ripple to the Airy diameter (Sec. 6.3).

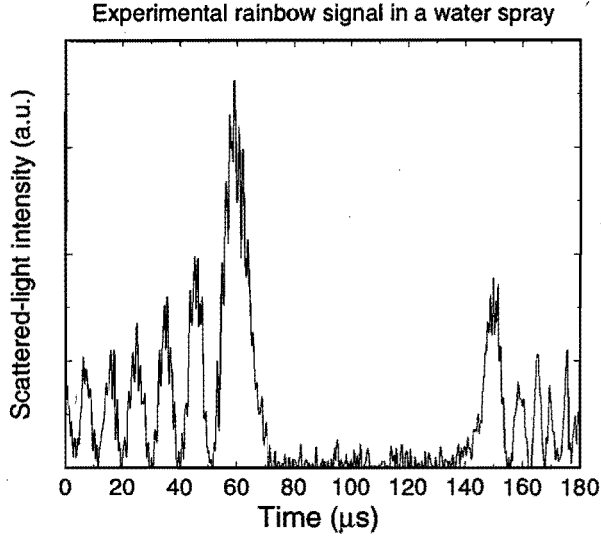


Figure 6.12: *An experimental rainbow pattern resulting from an oscillating droplet. Note the absence of the shadow of the wire. Therefore, the signal is rejected.*

Apart from non-sphericity and internal temperature gradient effects, transient events can also influence the applicability of the rainbow technique. In combustion engines for instance, the rapid droplet evaporation causes Δt_{ripple} and Δt_{Airy} to change during the passage of the droplet through the laser beam. In this case, no single droplet diameter can be assigned to the rainbow pattern. However, Sankar et al.[63] used this effect to measure the instantaneous droplet vaporization rate in controlled experiments with a burning stream of ethanol droplets.

In our experiments, transient events also occurred through the oscillation of the light-scattering droplet. Fig. 6.12 shows a rainbow signal recorded using the photomultiplier set-up. Two strange features are observed. Firstly, two rainbows can be seen. Secondly, the number of Airy fringes is much higher than for the signals presented in the previous section. The enlargement of the angular view is believed to be artificial because the rainbow fringes move in front of pin hole 2 (Fig. 6.3) not only because the droplet traverses the laser beam but also because the droplet, and thus the rainbow, oscillates. Fortunately, this transient event is revealed by the absence of a narrow wire shadow in the main rainbow maximum. In our case, where $\Delta t_{\text{wire}} \approx 20 \mu\text{s}$, the shadow could easily have covered

two entire Airy fringes! Rainbow signals without the wire diffraction pattern or those missing one or more Airy fringes are rejected. This implies that, when a narrow wire shadow is seen in the main rainbow maximum, the droplet must be non-oscillating. To find out whether the non-oscillating droplet is spherical, the diameter comparison method is used as was explained in Sec. 6.2.

Finally, it is important to realize that, by imposing the condition that the wire shadow has to be somewhere in the primary rainbow maximum, the dynamic range of the temperature measurement is restricted, though not severely. For water droplets, the dynamic range would be 100°C for a droplet diameter of $500\ \mu\text{m}$ increasing up to 800°C when the droplet measures about $20\ \mu\text{m}$.

Chapter 7

DISCUSSION AND CONCLUSIONS

The rainbow technique, first presented by N. Roth, K. Anders, and A. Frohn in 1988, has been further developed in this Ph.D. thesis. The technique is based on the detection of a monochromatic rainbow that is created by a droplet scattering laser light. This artificial rainbow reveals Airy fringes (with angular frequency F_{Airy}) and a ripple structure as a result of optical interference between internal and external reflection of laser light by the droplet. The ripple structure contains two closely-spaced peaks in the power spectrum, taken over two Airy fringes. The corresponding angular frequencies at F_2 and F_3 respect

$$F_3 - F_2 = F_{Airy}.$$

The rainbow interference pattern is conventionally detected by a linear CCD camera. From the angular position of the main rainbow maximum, the refractive index of the droplet can be determined, therefore the temperature, provided the droplet size is known. This necessary diameter can be deduced from either the Airy fringe spacing or the ripple interference structure by using the Airy theory for the rainbow. Because this theory is valid for spherical particles, both diameters are the same when the droplet is spherical. When the difference between the diameters exceeds the uncertainty in the size measurement, the particle is supposed to be non-spherical. In that case, no confidence can be established in the temperature measurement from the main rainbow maximum because the latter depends strongly on the droplet shape. Therefore, rainbow signals from non-spherical particles are rejected following the diameter comparison method.

A theoretical approach has been described to validate the non-sphericity detection method. Therefore, the change in angular frequency of the Airy fringes and ripple structure as well as the angular shift of the main rainbow maximum were predicted for an ellipsoidal droplet with constant and real refractive index. A vectorial equivalent of the Kirchhoff integral relation has been applied to express the far-field rainbow pattern in terms of the scattered field at the droplet surface. This near field was obtained by assigning an electric field vector to geometrically traced rays. As such, the contribution of internal and external reflection to the rainbow pattern could be written as a sum of Kirchhoff integrals for each geometrical contribution. Both integrals were solved by integrating over the respective

ridges in the phase functions of the integrands. In this thesis, only straight ridges have been treated which reduces the applicability of the presented surface integral method to geometrical rays that lie in one plane taken through the incoming and scattered wave vectors.

The shift of the rainbow pattern due to drop non-sphericity has been computed for prolates using the surface integral method. The results have been compared to the geometrical computations of W. Moebius, made in 1910. He predicted an angular shift that was independent of the droplet size. This agrees with the results of the surface integral method, although not quantitatively. The surface integral method computes an angular shift of 1° for 1% non-sphericity concerning a prolate illuminated by a plane wave along the long axis; Moebius predicted a shift of 0.75° .

The surface integral method is able to indicate that the influence of drop non-sphericity on the Airy fringes is different from the influence on the ripple structure. This feature was essential for the non-sphericity detection method. The computation revealed that for a prolate with $D_{short-axis} = 100 \mu\text{m}$ and $D_{long-axis} = 103 \mu\text{m}$, the Airy frequency, F_{Airy} , changes oppositely to F_2 , whereas F_3 hardly deviates from its value for an equivalent sphere. With increasing size, the dependency of the Airy fringes on droplet non-sphericity decreases. On the other hand, both F_2 and F_3 will alter in the same way; for an equivalent size of 1 mm, the ripple frequencies change 5% for 3% non-sphericity. These theoretical results are different from the experimental ones that were obtained from rainbow patterns created by satellite droplets around an unstable water jet. 5% change in F_3 for a millimetre-size droplet corresponded to an error in the temperature of about 5°C which would relate to a non-sphericity of only a fraction of 1% instead of 3%. However, because the shape of the droplets was not known during the experiments, it is dangerous to compare theory and practice in a quantitative manner. For this, it is suggested to perform fundamental experiments on acoustically or optically levitated droplets so that the droplet shape can easily be assessed and/or controlled.

The diameter-comparison method runs into difficulties when the ripple structure does not appear in the rainbow signal. One has to realize that the phase of the ripple structure changes 90° when the surface of the droplet deviates from the spherical shape by a fraction of the wavelength of the laser light. Therefore, it is plausible to believe that the ripple structure will be blurred when the rainbow pattern is created by an oscillating drop and then detected by the linear CCD camera with a finite time of integration of more than 0.1 ms. A solution to this could be to use a laser generating a light pulse with a duration much shorter than the oscillation time of the droplet. In this work, another solution has been chosen. The CCD camera has been replaced by a photomultiplier positioned behind a pin hole. A time-varying rainbow signal is detected when the rainbow interference structures move in front of the pin hole when the droplet traverses the laser beam. Experimental rainbow signals in a full-cone water spray have been recorded, showing that the ripple structure is always present.

In order to simulate the photomultiplier signal, the Lorenz-Mie theory had to be generalized so that off-axis Gaussian illumination could be described. Instead of using the rigorous generalized Lorenz-Mie theory (GLMT) of G. Gouesbet and G. Gréhan, a simplified approach was employed, based on a ring-shaped laser beam that respects the circular symmetry of the Lorenz-Mie theory. The localization principle was applied to the infinite Lorenz-Mie series in order to account for the non-uniform intensity profile of the laser beam. The symmetric approach of a non-symmetric situation dictates that meaningful results were only expected in the primary rainbow region where the detector was placed. There, the theoretical approach generates a spurious ripple structure and incorrect edge-ray contributions. Nevertheless, these artifacts are minor and the agreement with GLMT-computations is quite encouraging.

To relate the time-base of the photomultiplier signal to scattering angles, the droplet velocity had to be known. Therefore, a wire has been placed in the centre of the spatial filter of the rainbow receiver. This filter selects a probe volume in the water spray that contains only one droplet at a time. When the image of the droplet crosses the wire, a shadow is projected on the photomultiplier leading to a narrow dip in the main rainbow maximum. The width of the dip is related to one velocity component. Subsequently, the angular Airy and ripple frequencies are utilized to measure the droplet size and detect non-sphericity. Finally, the absolute scattering angle is recovered by a dynamic calibration procedure, such as for the CCD-camera set-up. After this, the position of the wire shadow with respect to the main rainbow maximum is a reliable measure for the droplet temperature.

The photomultiplier set-up has the advantage to be very sensitive to the scattered-light intensity and to be able to detect a rainbow pattern with clear Airy fringes and a proper ripple structure. In addition to the size and temperature measurements, one velocity component is obtained. This velocity measurement is independent of the (non-spherical) droplet shape and temperature. Unfortunately, the superposition of a wire diffraction pattern on the monochromatic rainbow is quite intrusive and can interfere with the ripple frequency in the power spectrum. The linear CCD camera set-up does not have this major disadvantage. It is obvious to examine whether an apparatus combining the pros of both detectors would result in a more robust, non-intrusive, diagnostic tool.

List of symbols

Roman symbols and abbreviations

symbol	dimension	definition
a_n	-	scattering coefficient
A	m	diameter of ellipsoid along the x -axis
A_{ln}	$J C^{-1} m^{-1/2} s^{-1/2}$	expansion coefficient
b	m	impact parameter of a geometrical ray
b_n	-	scattering coefficient
B	m	diameter of ellipsoid along the y -axis
B_{ln}	$J C^{-1} m^{-1/2} s^{-1/2}$	expansion coefficient
c	m/s	speed of light
c_n	-	coefficients for internal electromagnetic field
CCD	-	charge-coupled device
C	m	diameter of ellipsoid along the z -axis
C_n	-	term in Lorenz-Mie series
C_n^*	-	Lorenz-Mie series up to $n = n^*$
da	m^2	area element
d^3x	m^3	volume element
d_n	-	coefficients for internal electromagnetic field
DBT	-	dual burst technique
D	m	diameter
EPDA	-	extended phase-Doppler anemometry
f	m	phase function
f	m	focal length
F	$1/^\circ$	angular frequency
GLMT	-	generalized Lorenz-Mie theory
g	$J C^{-1} m^{1/2} s^{-1/2} 1/^\circ$	amplitude function in Kirchoff integral
g_n	-	beam shape coefficient
$g(p)$	-	normalized glare-point amplitude function
Gain	-	ratio between close-field scattered and incident irradiance
$G(\mathbf{r}, \mathbf{r}_p)$	m^{-1}	Green function
$G(\theta)$	-	Fourier transform of $g(p)$ over a limited range of scattering angles

h	-	coefficient in Eq. 4.12
$h_n^{(1)}$	-	spherical Hankel function
I	$\text{J m}^{-2} \text{s}^{-1}$	irradiance or light intensity
i	-	imaginary unit
$i_1(\theta)$	-	normalized Lorenz-Mie scattered-light intensity distribution for a polarization normal to the scattering plane
$i_2(\theta)$	-	normalized Lorenz-Mie scattered-light intensity distribution for a polarization parallel to the scattering plane
j_n	-	spherical Bessel function
$J_{n+\frac{1}{2}}$	-	Bessel function of the first kind
\mathcal{J}	-	Jacobian
K	-	two-dimensional normalized Kirchhoff integral
k	rad m^{-1}	wave number
LDV	-	laser-Doppler velocimetry
l	-	separation constant
l	-	number of focal points passed by a light ray
l	m	distance between probe volume and plane σ (Fig. 6.3)
l'	m	distance between pin hole 1 and plane σ' (Figs. 6.3 and 6.5)
M	-	magnification factor
m	-	refractive index
n	-	separation constant
n^*	-	separation constant
N	-	number of interactions between light ray and surface of scatterer
PDA	-	phase-Doppler anemometry
PIV	-	particle-image velocimetry
PMT	-	photomultiplier tube
P	J s^{-1}	radiant power
P_n^l	-	associated Legendre polynomial
P	bar	pressure
p	-	normalized position on cross section of sphere
q	m	parameter
r	m	polar spherical coordinate
r	-	Fresnel amplitude-reflection coefficient
R	m	radius
$S_1(\theta)$	-	normalized Lorenz-Mie scattering amplitude for a polarization normal to the scattering plane
$S_2(\theta)$	-	normalized Lorenz-Mie scattering amplitude for a polarization parallel to the scattering plane

t	s	time
t	-	Fresnel amplitude-transmission coefficient
TUE	-	Technische Universiteit Eindhoven
T	°C	temperature
u	m	space coordinate
u	$J C^{-1} m^{-1/2} s^{-1/2}$	scalar function employed to compute \mathcal{M} and \mathcal{N}
VKI		von Karman Institute
v	$m s^{-1}$	velocity
v	m	space coordinate
v	$J C^{-1} m^{-1/2} s^{-1/2}$	scalar function employed to compute \mathcal{M} and \mathcal{N}
w	-	laser beam radius
x	-	size parameter based on m_o
x	m	space coordinate
y	m	off-axis distance between the centre of the laser beam and the centre of the droplet
y	-	size parameter based on m_i
y	m	space coordinate
y	m	position on linear CCD array
y_n	m	spherical Bessel function of the second kind
Y	°	angle between wave vector and x -axis in (x, y) -plane
z	m	space coordinate
z	-	normalized angular deviation from the geometrical rainbow angle
z_n	-	arbitrary spherical Bessel function

Greek symbols

symbol	dimension	definition
α	-	coefficient in Eqs. 2.53, 2.54, 5.11 and 5.12
β	rad	phase between scattered and reference ray
γ	°	angle between wave vector and normal
$\delta(\mathbf{r} - \mathbf{r}_p)$	-	Dirac's delta function
δ	m	distance between two rays
$\Delta\Phi$	°	minimum angular separation
ϵ	$J^{-1} C^2 m^{-2} s$	electric permittivity
ζ	°	integration variable
ζ_n	-	Riccati-Bessel function
η	-	integration variable
θ	°	scattering angle

θ_1	°	scattering angle of main rainbow maximum
θ_2	°	scattering angle of first subsidiary maximum
Θ	°	polar spherical coordinate for ellipsoid
κ	rad	angle in Θ_1, ϕ_1 -plane used for definition of path of integration
λ	m	wavelength of light in vacuum
Λ		one-dimensional generalized Fourier integral
μ	J C ⁻² s	permeability
π_n	-	auxiliary polynomial
ρ	-	arbitrary argument of elementary solution
ρ	m	distance between the image of the droplet and the wire placed in the spatial filter
σ	rad	phase shift due to optical path length
σ	-	virtual measurement plane (Fig. 6.3)
σ'	-	image of virtual measurement plane (Fig. 6.3)
σ''	-	measurement plane (Fig. 6.3)
τ	°	angle between the ray, incident on the external droplet surface, and the tangential
τ'	°	angle between the ray, incident on the internal droplet surface, and the tangential
τ_n	-	auxiliary polynomial
φ	°	polar spherical coordinate
ϕ	°	polar spherical coordinate for ellipsoid
Φ	°	angle between polarization vector of incident beam and scattering plane
ψ_n	-	Riccati-Bessel function
Ψ	J C ⁻¹ m ^{-1/2} s ^{-1/2}	scalar function
Ψ	°	angle between wave vector and z-axis
ξ	-	integration variable
ω	m ⁻¹	circular frequency of light
$\Omega_{rainbow}$	-	rainbow integral

Vector quantities

symbol	dimension	definition
A	-	arbitrary vector function
e	-	unit vector
E	J C ⁻¹ m ^{-1/2} s ^{-1/2}	electric field
\mathcal{E}	J C ⁻¹ m ^{-1/2} s ^{-1/2}	space part of electric field
H	J C ⁻¹ m ^{-3/2} s ^{1/2}	magnetic field intensity
\mathcal{H}	J C ⁻¹ m ^{-1/2} s ^{-1/2}	space part of magnetic field intensity
k	rad m ⁻¹	wave vector

M	$J C^{-1} m^{-1/2} s^{-1/2}$	electromagnetic vector function
\mathcal{M}	$J C^{-1} m^{-1/2} s^{-1/2}$	space part of electromagnetic vector function
n	-	unit normal vector
N	$J C^{-1} m^{-1/2} s^{-1/2}$	electromagnetic vector function
\mathcal{N}	$J C^{-1} m^{-1/2} s^{-1/2}$	space part of electromagnetic vector function
p	-	polarization vector
r	m	radial vector
x	m	parametric representation of light ray

Subscripts

symbol	pertains to
\parallel	component parallel to a plane
\perp	component perpendicular to a plane
Airy	Airy fringes
b	beam incident on scatterer
e	extremum
i	inside the scatterer
inc	ray incident on a interface
l	integer separation constant l
min	minimum
max	maximum
n	integer separation constant n
n	maximum of n^{th} Airy fringe
o	outside the scatterer
o	laser beam waist
p	observation point
ref	reference
refl	reflected ray
rg	rainbow according to geometrical optics
ripple	ripple structure
s	scattered
tr	transmitted ray

Superscripts

symbol pertains to

'	first derivative
*	complex conjugate

φ	component in φ -direction
θ	component in θ -direction
ext	external reflection
int	internal reflection
norm	normal
r	component in radial direction

Mathematical operators

symbol denotes

\cdot	inner product
\times	cross product
\odot	autocorrelation of two functions
*	complex conjugate
$\mathcal{F}\{\}$	Fourier transform over a limited range of scattering angles
$\mathcal{F}^{-1}\{\}$	inverse Fourier transform over a limited range of scattering angles
$ \dots $	modulus
$\ \dots\ $	norm
$\langle \dots \rangle$	time average
Re	real part
Im	imaginary part
∇	gradient
Δ	Laplacian

References

- [1] Milton Abramowitz and Irene A. Stegun, *Handbook of mathematical functions*, 10th ed., Dover Publications, Inc., New York, 1972, Chap. 6, pp. 255-293.
- [2] ———, *Handbook of mathematical functions*, 10th ed., Dover Publications, Inc., New York, 1972, Chap. 10, pp. 446-452.
- [3] R.J. Adrian, *Multi-point optical measurements of simultaneous vectors in unsteady flow - a review*, *Int. J. Heat & Fluid Flow* **7** (1986), 127-145.
- [4] G.B. Airy, *On the intensity of light in the neighbourhood of a caustic*, *Trans. Camb. Phil. Soc.* **6** (1838), 379-402.
- [5] K. Anders, N. Roth, and A. Frohn, *Light scattering at the rainbow angle: Information on size and refractive index*, 3th International Congress on Optical Particle Sizing (Yokohama, Japan), August 1993, pp. 237-242.
- [6] ———, *Theoretical and experimental studies of the influence of internal temperature gradients on rainbow refractometry*, 4th International Congress on Optical Particle Sizing (PARTEC, ed.), Nuernberg, Germany, March 1995, pp. 419-428.
- [7] W.D. Bachalo and M.J. Houser, *Phase-doppler spray analyzer for simultaneous measurements of drop size and velocity distributions*, *Optical Engineering* **23** (1984), 403-429.
- [8] M.V. Berry and C. Upstill, *Catastrophe optics: Morphologies of caustics and their diffraction patterns*, *Progress in Optics* **18** (1980), 259-346.
- [9] C.F. Bohren and D.R. Huffman, *Absorption and scattering of light by small particles*, Wiley, New York, 1983, Chap. 4, pp. 82-101.
- [10] H. Bremmer, *Terrestrial radio waves*, New York, Elsevier, 1949.
- [11] R. Clift, J.R. Grace, and M.E. Weber, *Bubbles, drops and particles*, Ed. Academic Press, 1978.

- [12] F. Corbin, A. Garo, G. Gouesbet, and G. Gréhan, *Réfractométrie d'arc-en-ciel: Application au diagnostic des gouttes avec gradient d'indice*, Recueil des actes du 5^e Congrès Francophone de Vélocimétrie Laser (Rouen, France), Université & INSA de Rouen, URA CNRS 230/CORIA, September 1996, pp. E1.1–E1.8.
- [13] L. W. Davis, *Theory of electromagnetic beams*, Phys. Rev. A **19** (1979), 1177–1179.
- [14] F. Durst, A. Melling, and J.H. Whitelaw, *Principles and practice of laser-Doppler anemometry*, Academic Press Inc., 1976.
- [15] ———, *Principles and practice of laser-Doppler anemometry*, Academic Press Inc., 1976, Chap. 1, p. 12.
- [16] F. Durst and M. Zaré, *Laser Doppler measurements in two-phase flows*, LDA Symposium (Copenhagen, Denmark), 1975, pp. 403–429.
- [17] R.P. Feynman, *Qed: The strange theory of light and matter*, Princeton U.P., Princeton, NJ, 1985, Chap. 2.
- [18] O. Fiedler, N. Labahn, J. Kumpart, and K. Christofori, *Usage of the spatial filter method for measurements of local particle velocities in circulating fluidized beds*, 8th International Symposium on Applications of Laser Techniques to Fluid Mechanics (Lisbon, Portugal), July 1996, pp. 12.1.1–12.1.8.
- [19] Alistair B. Fraser, *Why can the supernumerary bows be seen in a rain shower?*, J. Opt. Soc. Am. **73** (1983), no. 12, 1626–1628.
- [20] Joseph W. Goodman, *Introduction to Fourier optics*, 2nd ed., McGraw-Hill companies, Inc, 1996, Chap. 6, pp. 154–156.
- [21] G. Gouesbet, B. Maheu, and G. Gréhan, *Light scattering from a sphere arbitrarily located in a gaussian beam, using a Bromwich formulation*, J. Opt. Soc. Am. A **5** (1988), no. 9, 1427–1443.
- [22] Gérard Gouesbet, Gérard Gréhan, and Bruno Maheu, *Computations of the g_n coefficients in the generalized Lorenz-Mie theory using three different methods*, Appl. Opt. **27** (1988), no. 23, 4874–4883.
- [23] Gérard Gouesbet and James A. Lock, *Rigorous justification of the localized approximation to the beam-shape coefficients in generalized Lorenz-Mie theory. II. off-axis beams*, J. Opt. Soc. Am. A **11** (1994), no. 9, 2516–2525.
- [24] G. Gréhan, B. Maheu, and G. Gouesbet, *Scattering of laser beams by Mie scatter centers: Numerical results using a localized approximation*, Appl. Opt. **25** (1986), 3539–3548.

- [25] Eugene Hecht, *Optics*, 2th ed., Addison Wesley Publishing Company, 1987, Chap. 14, p. 578.
- [26] ———, *Optics*, 2th ed., Addison Wesley Publishing Company, 1987, Chap. 10, pp. 401-434.
- [27] ———, *Optics*, 2th ed., Addison Wesley Publishing Company, 1987, Chap. 10, pp. 406-409.
- [28] ———, *Optics*, 2th ed., Addison Wesley Publishing Company, 1987, Chap. 11, pp. 500-501.
- [29] ———, *Optics*, 2th ed., Addison Wesley Publishing Company, 1987, Appendix 1, pp. 620-622.
- [30] ———, *Optics*, 2th ed., Addison Wesley Publishing Company, 1987, Chap. 4, pp. 92-113.
- [31] Edward A. Hovenac, *Calculation of far-field scattering from nonspherical particles using a geometrical optics approach*, *Appl. Opt.* **30** (1991), no. 33, 4739-4746.
- [32] W.J. Humphreys, *Physics of the air*, Dower Publishing, Inc., New York, 1964.
- [33] J.D. Jackson, *Classical electrodynamics*, 2th ed., John Wiley & Sons, Inc., New York, 1975, Chap. 9, pp. 432-435.
- [34] Erwin Kreyszig, *Advanced engineering mathematics*, 6th ed., John Wiley & Sons, Inc., New York, 1988, Chap. 9, pp. 534-540.
- [35] ———, *Advanced engineering mathematics*, 6th ed., John Wiley & Sons, Inc., New York, 1988, Chap. 9, pp. 519-527.
- [36] James A. Lock, *Theory of the observation made of high-order rainbows*, *Appl. Opt.* **26** (1987), no. 24, 5291-5297.
- [37] ———, *Cooperative effects among partial waves in Mie scattering*, *J. Opt. Soc. Am. A* **5** (1988), no. 12, 2032-2044.
- [38] James A. Lock and James H. Andrews, *Optical caustics in natural phenomena*, *Am. J. Phys.* **60** (1992), no. 5, 397-407.
- [39] James A. Lock and Gérard Gouesbet, *Rigorous justification of the localized approximation to the beam-shape coefficients in generalized Lorenz-Mie theory. I. on-axis beams*, *J. Opt. Soc. Am. A* **11** (1994), no. 9, 2503-2515.
- [40] James A. Lock and Edward A. Hovenac, *Internal caustic structure of illuminated liquid droplets*, *J. Opt. Soc. Am. A* **60** (1991), no. 5, 1541-1552.

- [41] L.V. Lorenz, *Upon the light reflected and refracted by a transparent sphere*, Vidensk. Selsk. Shrifter 6 (1890), 1–62, in Danish.
- [42] Beverly T. Lynds, *About rainbows*, 1995, Unidata Program Center, Colorado, U.S.A. <http://www.unidata.ucar.edu/staff/blynds/rnbw.html>.
- [43] P.L. Marston, *Rainbow phenomena and the detection of nonsphericity in drops*, Appl. Opt. **19** (1980), no. 5, 680–685.
- [44] P.L. Marston and E.H. Trinh, *Hyperbolic umbilic diffraction catastrophe and rainbow scattering from spheroidal drops*, NATURE **312** (1984), 529–531.
- [45] P. Massoli, F. Beretta, A. D'Alessio, and M. Lazzaro, *Temperature and size of single transparent droplets by light scattering in the forward and rainbow regions*, Appl. Opt. **32** (1993), no. 18, 3295–3301.
- [46] R. Meynart, *Flow velocity measurement by a speckle method*, SPIE **210** (1980), 25.
- [47] G. Mie, *Beitrage zur Optik trüber Medien speziell kolloidaler Metallösungen*, Ann. Phys. **25** (1908), 377–445.
- [48] M.G.J. Minnaert, *The nature of light and colour in the outdoors.*, Springer Verlag, 1993, Chap. 10, Title of original Dutch edition, published in 1937: De natuurkunde van 't vrije veld. I. Licht en kleur in het landschap.
- [49] W. Moebius, *Zur Theorie des Regenbogens und ihrer experimentellen Prüfung*, Ann. Phys. (Leipzig) **33** (1910), 1493–1558.
- [50] A.M. Murray and L.A. Melton, *Fluorescence methods for determination of temperature in fuel sprays*, Appl. Opt. **24** (1985), no. 7, 2783–2787.
- [51] A. Naqwi, F. Durst, and X.-Z. Liu, *An extended phase-doppler system for characterization of multiphase flows*, 5th International Symposium on Applications of Laser Techniques to Fluid Mechanics (Lisbon, Portugal), July 1990, pp. 24.4.1–24.4.6.
- [52] Numerical Algorithms Group, *The nag fortran library manual, mark 16*, 1st ed., 1993, Subroutines E02AEF and E02AFF.
- [53] H.M. Nussenzveig, *Complex angular momentum theory of the rainbow and the glory*, J. Opt. Soc. Am. **69** (1979), no. 8, 1068–1079.
- [54] ———, *Diffraction effect in semiclassical scattering, montroll memorial lecture series in mathematical physics*, Cambridge University Press, 1992, Chap. 3, p. 28.
- [55] J.F. Nye, *Rainbow scattering from spheroidal drops – an explanation of the hyperbolic umbilic foci*, NATURE **312** (1984), 531–532.

- [56] F. Onofri, G. Gréhan, G. Gouesbet, T.-H. Xu, G. Brenn, and C. Tropea, *Phase-doppler anemometry with the dual burst technique for particle refractive index measurements*, 7th International Symposium on Applications of Laser Techniques to Fluid Mechanics (Lisbon, Portugal), July 1994, pp. 21.41–48.
- [57] F. Onofri, G. Gréhan, B. Maheu, and G. Gouesbet, *diagaus3.f*, 1995, Fortran program for the computation of scattering diagrams for a sphere arbitrarily located in a Gaussian beam using GLMT.
- [58] J.R. Probert-Jones, *Surface waves in backscattering and the localization principle*, J. Opt. Soc. Am. **73** (1983), no. 4, 503.
- [59] N. Roth, K. Anders, and A. Frohn, *Simultaneous measurement of temperature and size of droplets in the micrometer range*, 7th International Congress on Optical Methods in Flow and Particle Diagnostics ICALEO 88, L.I.A. (Sunnyvale, U.S.A.), vol. 67, 1988, pp. 294–304.
- [60] ———, *Refractive-index measurements for the correction of particle sizing methods*, Appl. Opt. **30** (1991), no. 33, 4960–4965.
- [61] ———, *Simultaneous determination of refractive index and droplet size using Mie theory*, 6th International Symposium on Applications of Laser Techniques to Fluid Mechanics (Lisbon, Portugal), July 1992, pp. 15.5.1–15.5.5.
- [62] S.V. Sankar, D.H. Buermann, and W.D. Bachalo, *An advanced rainbow signal processor for improved accuracy in droplet temperature measurements*, 8th International Symposium on Applications of Laser Techniques to Fluid Mechanics, vol. 1, Lisbon, Portugal, July 1996, pp. 9.3.1–9.3.9.
- [63] ———, *Application of rainbow thermometry to the study of fuel droplet heat-up and evaporation characteristics*, International Gas Turbine and Aeroengine Congress & Exhibition (Birmingham, UK), June 1996, pp. 96–GT-21.
- [64] S.V. Sankar, K.H. Ibrahim, D.H. Buermann, M.J. Fidrich, and W.D. Bachalo, *An integrated phase doppler/rainbow refractometer system for simultaneous measurement of droplet size, velocity, and refractive index*, The Third International Congress on Optical Particle Sizing (Yokohama, Japan), August 1993, pp. 275–284.
- [65] J.K. Schaller, S. Wassenberg, D.K. Fiedler, and C.G. Stojanoff, *A new method for temperature measurements of droplets*, ICLASS-94, Rouen, France, July 1994, pp. IV–9.
- [66] Julius A. Stratton, *Electromagnetic theory*, McGraw-Hill Book Company, Inc., New York, 1941, Chap. 2, pp. 131–137.

- [67] I. Thormählen, J. Straub, and U. Grigull, *Refractive index of water and its dependence on wavelength, temperature and density*, J. Phys. Chem. Ref. Data **14** (1985), no. 4, 933-945.
- [68] J.P.A.J. van Beeck, *mie96.f*, 1996, Fortran program for the computation of scattering diagrams for a sphere arbitrarily located in a Gaussian beam using Lorenz-Mie theory in combination with the localization principle.
- [69] ———, *kirchhoff97.f*, 1997, Fortran program based on the surface integral method used for computation of scattering diagrams of an ellipsoid arbitrarily oriented with respect to an incident, planar wave front.
- [70] J.P.A.J. van Beeck and M.L. Riethmuller, *Détermination non-intrusive de la dimension et de la température des gouttes dans une pulvérisation*, Recueil des actes du 4^e Congrès Francophone de Vélocimétrie Laser (Poitiers, France), Laboratoire de Chimie Physique de la Combustion, Université de Poitiers-CNRS, September 1994, pp. 2.2.1-2.2.8.
- [71] ———, *Simultaneous determination of temperature and size of droplets from the rainbow using Airy theory*, Proc. of the 7th International Symposium on Applications of Laser Techniques to Fluid Mechanics, vol. 2, Lisbon, Portugal, July 1994, also in "Developments in Laser Techniques and Applications to Fluid Mechanics", R.J. Adrian et al.(eds.), Springer, pp. 330-339, pp. 21.5.1-21.5.6.
- [72] ———, *Nonintrusive measurements of temperature and size of single falling raindrops*, Appl. Opt. **34** (1995), no. 10, 1633-1639.
- [73] ———, *Détermination simultanée de la vitesse, de la température et du diamètre des gouttes par la méthode de l'arc-en-ciel dans une pulvérisation*, Recueil des actes du 5^e Congrès Francophone de Vélocimétrie Laser (Rouen, France), Université & INSA de Rouen, URA CNRS 230/CORIA, September 1996, pp. E2.1-E2.8.
- [74] ———, *Rainbow phenomena applied to the measurement of droplet size and velocity and to the detection of nonsphericity*, Appl. Opt. **35** (1996), no. 13, 2259-2266.
- [75] ———, *A single-beam velocimeter based on rainbow-interferometry*, 8th International Symposium on Applications of Laser Techniques to Fluid Mechanics (Lisbon, Portugal), vol. 1, July 1996, pp. 9.1.1-9.1.6.
- [76] ———, *Rainbow interferometry with wire diffraction for simultaneous measurement of droplet temperature, size and velocity*, Accepted for publication in Part. Part. Syst. Charact.

- [77] H.C. van de Hulst, *Light scattering by small particles*, Dover Publications, Inc., N.Y, 1981, Chap. 13, p. 249, originally published in 1957 by John Wiley & Sons, Inc., N.Y.
- [78] ———, *Light scattering by small particles*, Dover Publications, Inc., N.Y., 1981, Chap. 17, pp. 367-374, originally published in 1957 by John Wiley & Sons, Inc., N.Y.
- [79] ———, *Light scattering by small particles*, Dover Publications, Inc., N.Y., 1981, Chap. 9, pp. 119-126, originally published in 1957 by John Wiley & Sons, Inc., N.Y.
- [80] ———, *Light scattering by small particles*, Dover Publications, Inc., N.Y., 1981, Chap. 12, pp. 208-209, originally published in 1957 by John Wiley & Sons, Inc., N.Y.
- [81] ———, *Light scattering by small particles*, Dover Publications, Inc., N.Y., 1981, Chap. 12, pp. 206-207, originally published in 1957 by John Wiley & Sons, Inc., N.Y.
- [82] ———, *Light scattering by small particles*, Dover Publications, Inc., N.Y., 1981, Chap. 13, pp. 240-249, originally published in 1957 by John Wiley & Sons, Inc., N.Y.
- [83] ———, *Light scattering by small particles*, Dover Publications, Inc., N.Y., 1981, Chap. 3, pp. 17-21, originally published in 1957 by John Wiley & Sons, Inc., N.Y.
- [84] H.C. van de Hulst and R.T. Wang, *Glare points*, *Appl. Opt.* **30** (1991), no. 33, 4755-4763.
- [85] B. van der Pol and H. Bremmer, *The diffraction of electromagnetic waves from an electrical point source round a finitely conducting sphere, with applications to radio-telegraphy and the theory of the rainbow*, *Phil. Mag.* **24** (1937), pp. 141-176 and 825-864.
- [86] Jearl D. Walker, *Multiple rainbows from single drops of water and other liquids*, *Am. J. Phys.* **44** (1976), no. 5, 421-433.
- [87] Ru T. Wang and H.C. van de Hulst, *Rainbows: Mie computations and the Airy approximation*, *Appl. Opt.* **30** (1991), no. 1, 106-116.
- [88] David C. Wilcox, *Perturbation methods in the computer age*, DCW Industries, Inc. La Cañada, California, 1995, Chap. 2, pp. 34-48.
- [89] W. J. Wiscombe, *Improved Mie scattering algorithms*, *Appl. Opt.* **19** (1980), 1505-1509.

-
- [90] Y. Yeh and H.Z. Cummins, *Localized flow measurements with an He-Ne laser spectrometer*, Appl. Phys. Letters 4 (1964), 176-178.

Summary

Liquid sprays appear in a variety of aerospace, automotive and industrial applications. In order to be able to employ the optimal spray configuration it is essential that one first develops a complete understanding of the fundamental phenomena that influence and control the overall spray performance for such applications. Toward this end, the development of advanced diagnostic tools is necessary for studying spray processes in both ideal laboratory conditions and realistic environments.

The objective of the thesis was to study the first-order rainbow and to apply it to the non-intrusive determination of droplet parameters in spray environments. The first-order rainbow is created in the laboratory by droplets scattering laser light and this is therefore monochromatic. The effect of size and temperature (and thereby refractive index) of spherical droplets on the rainbow characteristics have been predicted by the Lorenz-Mie and Airy theories.

Experiments on satellite droplets around an unstable water jet, performed with a linear CCD-camera, have revealed the effect of droplet non-sphericity on the accuracy of the temperature and size measurements. To understand this effect better, a surface integral method has been developed which describes the behaviour of the rainbow for an ellipsoidal scatterer. The theoretical approach is based on the vectorial Kirchhoff integral relation taken over the electric field on the droplet surface, with the electric field obtained using ray-optics. The integral has been solved by looking for the ridge of stationary points in the integrand of the Kirchhoff integral. A comparison with the Lorenz-Mie theory has validated the approach in the special case of spherical scatterers. The surface integral method endorses the experimental non-sphericity detection method that selects, using the rainbow pattern, spherical droplets. This method has considerably improved the accuracy of the droplet parameters measured using the rainbow technique.

A rainbow detection device has been developed for measuring simultaneously the size, temperature and velocity of individual spherical droplets in liquid sprays. The rainbow is recorded by a photomultiplier placed behind a pin hole and a spatial filter containing a wire perpendicular to the scattering plane. The wire diffraction and rainbow interference patterns move in front of the pin hole as the droplet traverses the laser beam. Preliminary experiments in a full-cone water spray at isothermal conditions revealed the feasibility of the device in spray environments and stressed the importance of the non-sphericity detection method.

Samenvatting

Vloeistofverstuivers worden toegepast in de vliegtuigbouw, auto-industrie en andere industriële processen. Opdat de juiste verstuiverconfiguratie wordt gebruikt, dient men zich een volledig beeld te vormen van alle fundamentele verschijnselen die het gedrag van verstuivers kunnen beïnvloeden. Daarom is het noodzakelijk om hoogwaardige diagnostische apparaten te ontwikkelen die dat gedrag in zowel realistische als geïdealiseerde omstandigheden kunnen onderzoeken.

Het promotieonderzoek had tot doel te bestuderen of de regenboog te gebruiken is voor het meten van fysische grootheden van druppeltjes in een verstuiver. Daartoe is een eenkleurige regenboog gegenereerd door verstrooiing van een laserbundel aan druppeltjes. De Lorenz-Mie en Airy theorieën zijn aangewend om uit diverse regenboogverschijnselen de grootte en brekingsindex, dus de temperatuur, van de druppels af te leiden.

De eerste experimenten werden uitgevoerd met een lineaire CCD-camera om de fijnstructuren in de regenboog waar te nemen die gevormd werden door satellietdruppeltjes rond een instabiele waterstraal. Het bleek dat niet-bolvormigheid de nauwkeurigheid van de temperatuur- en groottemeting onaanvaardbaar verlaagde. Om deze invloed beter te begrijpen, is een theoretisch model ontwikkeld dat de verandering van de relevante eigenschappen van de regenboog voorspelt voor een druppel met een ellipsoïdale vorm. Het model is gebaseerd op een vektorieële uitdrukking van de Kirchhoffintegraal over het elektrische veld op het druppeloppervlak, verkregen via geometrische optica. Door slechts het pad over de stationaire punten in de integrand te beschouwen, kan de oppervlakte-integraal vereenvoudigd worden tot een lijnintegraal. De theoretische resultaten van het model bekrachtigen de experimentele selectie van bolvormige druppeltjes via frequentieanalyse van het regenboogsignaal. Deze selectiemethode heeft de nauwkeurigheid van de metingen aanzienlijk verhoogd.

Een regenboogapparaat is ontwikkeld dat tegelijkertijd de grootte, temperatuur en snelheid meet van individuele druppeltjes in een waterverstuiver. Het apparaat bevat een photomultiplier die de regenboog waarneemt achter een diafragma en een ruimtefilter met daarin een draad loodrecht op het strooivlak. Het draaddiffractiepatroon en de eenkleurige regenboog verplaatsen zich voor het diafragma wanneer de druppel de laserbundel doorkruist. De experimentele resultaten demonstreren de toepasbaarheid van het apparaat voor onderzoek naar warmte- en massatransport in vloeistofverstuivers.

Acknowledgements

In October 1992, I started to investigate the rainbow technique at the von Karman Institute (VKI). It was the subject of my research project carried out during the post-graduate Diploma Course in fluid dynamics. Because of successful results, I was given the opportunity to enter the doctoral programme of VKI and dive deeper in rainbow phenomena. For this, I thank the VKI staff and I extend my thanks for its financial support during the entire programme. I am most grateful to my supervisor, Prof. M.L. Riethmuller, who has always believed in the potential of the rainbow technique, even when results were disappointing. His numerous suggestions and continuous support made me find solutions.

I thank my promoter Prof. van Dongen at the University of Eindhoven (TUE) for following my progress at VKI with great interest. His critical questions have improved the results and readability of the thesis considerably. I also thank my second promoter Prof. van Heijst and Prof. Sluijter for their valuable remarks.

It was a honour for me that one of the generalizers of the Lorenz-Mie theory, Dr. Gréhan, was so kind to correct chapter 2 with great precision.

Thank you Patricia Waller, for finding so much time to check the body of the thesis concerning English grammar and spelling. Nick Waterson has looked carefully to the summary and Maaïke van Houdt kindly assisted me to check the "samenvatting" for the new Dutch spelling which was not a "peuleschil" (or "peuleschil?").

I thank Jean-Philippe Pages, Philippe Hollander and Fabrice Giuliani for their important contributions to the rainbow experiments. However, without the professional help of the technicians of the Environmental and Applied Fluid Dynamics department, not one rainbow would have been observed. I also owe a thank you to Laurent Beaurain for his ultra-precise uncertainty calculations.

The educational atmosphere at VKI is stimulating and leads to high-level research. Moreover, the interactions between skillful and enthusiastic students, engineers and staff members result in critic personalities. For me, it were above all the members of the doctoral programme that made my stay at VKI to a very pleasant, instructive and unforgettable experience.

I owe a tremendous debt to my family and friends in the Netherlands who supported me throughout my entire studies. Floortje van Houdt, thanks for our romantic discussions on rainbow phenomena and for your patience and understanding during the final rush.

Curriculum Vitae

- 15 april 1969 geboren te Deurne (NL)
- juni 1987 diploma Gymnasium
Sint-Willibrord Gymnasium, Deurne (NL)
- juni 1993 diploma Technische Natuurkunde
Technische Universiteit Eindhoven (NL)
- december 1990 -
maart 1991 stage fysische meteorologie
Koninklijk Nederlands Meteorologisch Instituut, De Bilt (NL)
- juni 1991 -
augustus 1991 stage turbomachinerie
von Karman Instituut, Sint-Genesius-Rode (B)
- juni 1993 diploma post-doctorale opleiding in stromingsdynamica
von Karman Instituut, Sint-Genesius-Rode (B)
- oktober 1993 -
juni 1997 promotieonderzoek
von Karman Instituut, Sint-Genesius-Rode (B)
Technische Universiteit Eindhoven (NL)

Stellingen behorende bij het proefschrift
"RAINBOW PHENOMENA:
development of a laser-based, non-intrusive technique
for measuring droplet size, temperature and velocity".
door J.P.A.J. van Beek

1. Lichtverstrooiing door een bolvormig deeltje kan als een singulariteit beschouwd worden, gezien de grote gevoeligheid van het lichtverstrooiingspatroon voor een geringe afwijking van de bolvorm.

Dit proefschrift

2. De bewering van P.L. Marston in 1980 dat de fluctuaties in de kleuren van de regenboog, waargenomen tijdens een donderslag, worden veroorzaakt door druppel-oscillaties als gevolg van akoestische koppeling, verdient hernieuwde aandacht.

Marston, P.L. (1980), Appl. Opt., Vol. 19, No. 5, pp. 680-685.

3. De mistboog is overwegend wit door diffractie en externe reflectie van zonlicht aan het druppeloppervlak, en niet alleen door kleurenmenging van het Airy-regenboogpatroon, zoals beschreven door M.G.J. Minnaert.

Minnaert, M.G.J. (1993), Light and Color in the Outdoors, pp. 201-202
(vertaling van de originele Nederlandstalige editie, verschenen in 1937:
- De Natuurkunde van 't Vrije Veld. I. Licht en kleur in het landschap -).

4. De historische splitsing van het Airy-regenboogpatroon in de termen "main rainbow maximum" en "supernumerary bows" is misleidend.
5. De "complex angular momentum (CAM)"-theorie voor de regenboog, gepresenteerd in 1979 door H.M. Nussenzweig, vindt zijn oorsprong in het werk van B. van der Pol en H. Bremmer in 1937, waarin het Airy-regenboogpatroon afgeleid wordt van de Lorenz-Mie-theorie.

Nussenzweig, H.M. (1979), J. Opt. Soc. Am., Vol. 69, No. 8, pp. 1068-1079.
Van der Pol, B. en Bremmer, H. (1937), Phil. Mag., Vol. 24, pp. 141-176, 825-864.

6. Het verdwijnen van de fijnstructuur in de regenboog door de eindige sluitertijd van de CCD-camera kan vermeden worden door het gebruik van een flietslaser.

Dit proefschrift

7. De regenboogtechniek is de meest nauwkeurige meettechniek om de druppeltemperatuur in een verstuiver te bepalen mits de lichtverstrooiende druppels bolvormig zijn.

Dit proefschrift

8. In het huidige computertijdperk vergeet de onderzoeker maar al te vaak dat een asymptotische benadering van de wiskundige beschrijving van zijn fysisch model veel onnodige CPU-tijd kan besparen.

*Naar Wilcox, D.C. (1995), Perturbation Methods in the Computer Age, p. 189.:
"Do asymptotics now, save CPU time later!"*

9. De combinatie van een nucleatie-puls techniek en Lorenz-Mie-verstrooiing biedt de mogelijkheid om de binaire diffusiecoëfficiënt in condenserende dampmengsels nauwkeurig te bestuderen als functie van druk en temperatuur.

Luijten, C.C.M., Bosschaart, K.J. and Van Dongen, M.E.H. (1997), to be published in Int. J. Heat Mass Transfer.

10. "Particle image velocimetry" (PIV) is een geschikte experimentele methode om de kwaliteit van het sub-rooster-model van een "large eddy"-simulatie (LES) te bestuderen.

11. Niemand kan zo vermakelijk arrogant zijn als een jonge wetenschapper die pas een oud idee heeft ontdekt en denkt dat het origineel is.

Naar Harris, S.J. (1917), Amerikaans journalist en columnist.

12. De gang van zaken rond het op de markt brengen van genetisch gemanipuleerd voedsel heeft de reputatie van de wetenschap schade toegebracht.

13. Het verbluffende observatievermogen van een kat op een onderzoeksinstituut kan een gunstige uitwerking hebben op de kwaliteit van de onderzoeksresultaten.

Eindhoven, 26 juni 1997